THREE-DIMENSIONAL NANOSCOPY WITH A

DOUBLE-HELIX MICROSCOPE

by

SRI RAMA PRASANNA PAVANI

B.E., Government College of Technology, 2003

M.S., University of Colorado, 2006

A thesis submitted to the

Faculty of the Graduate School of the

University of Colorado in partial fulfillment

of the requirement for the degree of

Doctor of Philosophy

Department of Electrical, Computer, and Energy Engineering

2009

This thesis entitled:
Three-dimensional nanoscopy with a double-helix microscope
written by Sri Rama Prasanna Pavani
has been approved for the Department of Electrical, Computer, and Energy
Engineering

_____

(Rafael Piestun)

_____

(Carol J. Cogswell)

Date_____

The final copy of this thesis has been examined by the signatories, and we find that
both the content and the form meet acceptable presentation standards of scholarly
work in the above mentioned discipline.

Pavani, Sri Rama Prasanna (Ph.D., Electrical, Computer, and Energy Engineering)

Three-dimensional nanoscopy with a double-helix microscope

Thesis directed by Associate Professor Rafael Piestun

Optical microscopy has evolved into a powerful tool for modern scientific investigations. It has enabled biologists to study cells; physicists to analyze forces on microparticles; chemists to examine molecular dynamics; and engineers to fabricate microstructures. The so-called optical diffraction limit, however, prohibits conventional optical microscopes from resolving nanometer scale structures such as intricate intracellular features in three dimensions. This thesis introduces a three-dimensional (3D) nanoscopy paradigm that breaks the diffraction limit by resolving nanometer scale structures in all three dimensions with a far-field optical microscope exhibiting a double-helix point spread function (DH-PSF).

DH-PSF is an engineered 3D PSF specifically designed for 3D position estimation and imaging. It exhibits two lobes that rotate continuously around the optical axis with propagation, thereby forming a 3D double-helical shape. A DH-PSF is generated efficiently using a phase mask designed with a multi-domain optimization procedure. A variety of two-dimensional microscope modalities such as bright-field, dark-field, and fluorescence are directly transformed into their 3D counterparts by placing appropriate DH-PSF phase masks in their imaging paths. An information theoretical analysis shows that the DH-PSF carries higher and more uniform Fisher Information about a particle's 3D position than the PSF of traditional imaging systems. Experiments with DH-PSFs demonstrate nanometer scale 3D

position localization, 3D tracking, and 3D velocimetry of multiple scattering and fluorescent particles.

Single fluorescent molecules are localized in 3D with nanometer scale precisions using a DH-PSF fluorescent microscope. By photoactivating (turning on) different sparse subsets of fluorophores at different times, molecules separated by a few nanometers are resolved, thereby breaking the optical diffraction limit by over an order of magnitude in all three dimensions.

A polarization specific DH-PSF nanoscope is also introduced. Light emitted by individual fluorescent protein molecules is decomposed into orthogonal polarization channels, phase modulated, and separately detected to resolve polarization-specific structures of a biological cell with nanometer scale 3D resolution.

Dedicated to

Amma, Nanna, and Kaushik

Acknowledgements

This thesis would not have been possible had it not been for the encouragement of a number of well wishers, whose academic, financial, and emotional support during the course of my PhD can perhaps be summarized in one word – *priceless*.

My advisor Prof. Rafael Piestun inspired me to confront fundamental high-impact scientific problems, and has been instrumental in making me recognize, hone, and apply my niche to find elegant solutions. I could not have asked for a better mentor. My co-advisor Prof. Carol Cogswell introduced me to microscopy, and gave me the freedom to pursue my own ideas. She essentially formed the foundation for my interest in imaging. Prof. W. Thomas Cathey offered me a position in his Imaging Systems Laboratory, which was my principal motivation to choose the University of Colorado (CU) for my graduate education. He has been an enormous source of inspiration throughout my PhD.

CU's wonderful optics and imaging courses and laboratory classes provided me with a solid background to rest on while pursuing my doctoral research. I thank Prof. Kelvin Wagner, Prof. Alan Mickelson, Prof. Robert Mcleod, Prof. Gregory Beylkin, Prof. Ivan Smalyukh, Prof. Francois Meyer, and Prof. C. T. Mullis for equipping me with a rich set of scientific tools, and for their perennial willingness to help.

Dr. Adam Greengard's PhD thesis on rotating point spread functions has been an enormous motivation for my research. Fruitful interdisciplinary

Contents

List of Figures

Fig. 2.7. DH-PSF illustrated as a function of the defocus parameter (ψ). DH-PSF is generated by a mask that is obtained from an optimization procedure that simultaneously optimizes the PSF is the GL domain, Fourier domain, and spatial domain. [See movie from Opt. Exp. **16**, 3484 (2008)]

Fig. 2.8. A DH-PSF mask designed for a wavelength of 550nm, when used with the wavelengths 500nm and 600nm, exhibits the same rotation rates as function of defocus parameter (ψ) and slightly different rotation rates as a function of depth (NA=0.71).

Fig. 2.9. Phase-only DH-PSF masks and their PSFs at different defocus values: a) exact DH-PSF mask with continuous phase levels, b) 4-level phase quantized DH-PSF mask

Fig. 2.10: Experimental observation of the DH-PSF by focusing a collimated HeNe laser beam with a 0.09NA lens, after the beam reflected off of a phase-only spatial light modulator encoding the DH-PSF phase mask. [See movie from Opt. Exp. **16**, 3484 (2008)]

Fig. 3.1. Comparison of standard and double-helix (DH) PSFs: (a) The shape of the standard PSF barely changes along the focal region, beyond which the PSF rapidly expands in size. (b) The DH-PSF exhibits two main lobes that continuously rotate along the axial (Z) dimension.

Fig. 3.3. Imaging system engineered for 3D position localization: The PSF of an imaging system is engineered to exhibit two main lobes that continuously rotate along the optical axis. The PSF is implemented with a phase mask placed in the Fourier transform plane. For a particle in focus, the two lobes are oriented horizontally. When a particle is located in front of the focal plane, its PSF lobes are rotated in the counter-clockwise direction. On the other hand, when a particle is located behind the focal plane, its PSF lobes are rotated in the clockwise direction. In contrast, a standard imaging system (without the phase mask) would only blur particles outside the focal region.

Fig. 3.4. Information-theoretical comparison of DH and standard PSF for Gaussian and Poisson noise: The plots represent a comparison of DH and standard PSF CRBs, together with the implemented estimator variances in all three spatial dimensions for Gaussian (a-c) and Poisson (d-f) noise distributions. The system has 0.45 numerical aperture, 40X magnification, 6.3µm pixel width, and 633nm wavelength. (a,d), (b,e), and (c,f) show the CRBs and variances for Z, X, and Y dimensions, respectively, as a function of Z for an SNR of 30. The CRB of the DH-PSF is lower and more uniform than the CRB of the standard PSF in all three spatial dimensions.

Fig. 3.5. Experimental setup for 3D localization with a DH-PSF system. A glass slide containing a 3D distribution of point scatterers is illuminated with a horizontally

polarized Argon laser source (514.5nm wavelength), which is made spatially incoherent by a rotating diffuser. The imaging path consists of a microscope section and a signal processing section containing a spatial light modulator to encode the DH-PSF phase mask (upper-left inset) in the Fourier plane. The detected image consists of a diffracted (1st) order containing the DH-PSF image, and an undiffracted (0th) order containing the standard PSF image (bottom-right inset). This system can estimate the 3D locations of multiple sparse particles using a single image.

Fig. 3.6: 3D localization results. (a) Standard PSF and (b) DH-PSF images of five scatterers located at different transverse and axial positions inside the volume of a glass slide. The scale bar in the bottom right of the images represents 1μm. While the standard PSF image blurs the particles outside the focal plane, the DH-PSF image encodes the axial location of the particles in the rotation angle of the PSF lobes. (c) 3D position estimation result from the DH-PSF image in (b). [See related movie from Appl. Phys. Lett. **95**, 021103 (2009)]

Fig. 3.7. (a) Dark-field DH-PSF mask that produces a dark-field DH-PSF image of (d) in +1st order by directing the lower spatial frequency components to the -1st order (b). (c) Dark-field standard PSF image obtained in the +1st order using a blazed grating with an opposite blaze in a central circular region

Fig. 3.8: DH and standard PSF images of a particle at depths (a, e) 0μm, (b,f) 0.8μm, (c,g) 1.6μm, and (d,h) 2.4μm. These images were obtained by moving the piezo stage containing the glass slide in the axial dimension. The scale bar in the bottom right of the images represents 1μm. (i) Calibration plot of rotation angle at 200nm axial steps through a range of 3 μm. The standard deviation of 20 rotation angle estimations is plotted as an error bar at each axial step.

Fig. 3.9: The midpoint of the centroids of two lobes exhibits aberration-induced position variations along the X dimension (a) and the Y dimension (b) as a function of the axial distance. The transverse position of a particle is estimated by correcting this transverse position variations from the midpoint of its DH-PSF lobes.

Fig. 3.10: Effect of SNR: This figure compares the CRBs of DH and standard PSFs, together with the practical estimator variances at different SNRs under Gaussian (a-c) and Poisson (d-f) noise distributions. The system parameters are the same as in Fig. 3.4. The CRBs and variances are calculated for specific Z locations: $Z = 4\mu m$ (Z-dimension), $Z = 0\mu m$ (X and Y dimensions). CRBs and estimator variances decrease with increase in SNR. The CRB of the DH-PSF is lower than that of the standard PSF for a wide range of SNRs in all three dimensions. For Gaussian noise, the practical DH-PSF estimator variance is lower than the standard PSF CRB for all SNRs in the Z (a) and X (b) dimensions, and approximately overlaps with the standard PSF CRB in the Y dimension (c). For the Poisson noise case, the practical DH-PSF estimator variance is lower than the standard PSF CRB in the Z dimension (d), and is higher than the standard PSF CRB in the X (e) and Y (f) dimensions. The estimator variance of an equivalent (centroid based) standard PSF estimator is found to be higher than

the practical DH-PSF estimator variance in the X and Y dimensions for both Gaussian (b,c) and Poisson noise (e,f).

Fig. 3.11: Comparison of the standard and DH PSF images of five scatterers that are located at different 3D locations. As the system is defocused (using the piezo stage), the standard PSF image blurs the scatterers, while the DH-PSF image encodes the axial locations of the scatterers in the rotatation angle of the DH-PSF lobes. [See movie from Appl. Phys. Lett. **95**, 021103 (2009)]

Fig. 4.1. Comparison of the (a) DH-PSF and the (b) standard PSF at different axial planes for a system with 0.45 numerical aperture (NA) and 633nm wavelength.

Fig. 4.2. Information theoretical comparison of DH and standard PSFs for a photon-limited system with Poisson noise. The system has 0.45NA, 40x magnification, 6.3µm pixel width, and 633nm wavelength. See text for explanation of SNR. (a-c) compare the CRBs of the DH and standard PSFs as a function of axial distance for the (a) Z, (b) X, and (c) Y dimensions. (d) compares CRB_{3D} of the DH and standard PSFs. DH-PSF has lower CRB_{3D} than the standard PSF in regions A (focal region) and C, while the standard PSF has lower CRB_{3D} in region B. CRB_{AVG} is lower for the DH-PSF than the standard PSF. DH-PSF, therefore, on an average, carries more information about the position of a particle than the standard PSF.

Fig. 4.3. Experimental setup for three dimensional tracking of moving fluorescent particles: A horizontally polarized beam with 488nm wavelength excites 1µm wide yellow-green (Excitation peak: 505nm, Emission peak: 515nm) fluorescent microspheres. The microspheres are imaged by a 1.3NA oil-immersion infinity corrected objective and a tube lens. In the infinity space of the objective, a 515nm interference filter with 10nm bandwidth blocks out the excitation wavelength, and a polarizer passes only horizontally polarized emitted light. Finally, a phase-only spatial light modulator encoding the DH-PSF mask (top-right inset) engineers the system's PSF to have two rotating lobes. Unlike the standard PSF image which blurs the particles outside the focal region, the DH-PSF image encodes the particle's axial location in the angular orientation of its PSF lobes (bottom insets). The scale bar in the images represents 1µm.

Fig. 4.4. Movies of fluorescent microsphere tracking in three dimensions. The first movie [See movie from Opt. Exp. **16**, 22048 (2008)] (a-c) shows (a) the DH-PSF image, (b) the standard PSF image, and (c) the 3D locations of four microspheres. The second movie [See movie from Opt. Exp. **16**, 22048 (2008)] (d-f) displays X-Y, X-Z, and Y-Z projections of the microspheres' 3D locations.

Fig. 4.5. Time-varying velocities in all three dimensions for (a) particle 1, (b) particle 2, and (c) particle 3.

Fig. 4.6. (a) Calibration plot that maps rotation angle to axial distance. Correction factors for (b) X and (c) Y dimensions that are used in transverse position estimation.

Fig. 5.1: a) Collection path of the single molecule DH-PSF setup. IL is the imaging lens of the microscope, L1 and L2 are focal length matched achromatic lenses, and SLM is a liquid crystal spatial light modulator. b) Typical calibration curve of angle between two lobes with respect to the horizontal versus axial position measured with a piezo-controlled objective. Inset: 3D plot of the DH-PSF intensity profile (Scale bar: 400nm). c) images of a fluorescent bead used for the calibration curve in b) at different axial positions, with 0 being in focus.

Fig. 5.2. 3D localization of a single molecule. (*A*) Histogram of 44 localizations of one single photoactivated DCDHF-V-PF$_4$ molecule in *x*, *y*, and *z* in a layer of PMMA. The standard deviations of the measurements in *x*, *y*, and *z* are 12.8, 12.1, and 19.5 nm, respectively. The smooth curve is a Gaussian fit in each case. An average of 9,300 photons were detected per estimation on top of background noise fluctuations of 48 photons per pixel. (*B*) Representative single-molecule image with DH-PSF acquired in one 500-ms frame. (*C*) Localizations plotted in 3 dimensions.

Fig. 5.3. 3D super-localizations of a low concentration of DCDHF-P molecules in a thick PMMA sample. (*A*) Comparison of the standard PSF (i.e., *Upper*, SLM off) to the DH-PSF image of 2 molecules (*Lower*, SLM on). (Scale bar: 1 μm.) (*B*) Representative image of many single molecules at different *x*, *y*, and *z* positions. (Scale bar: 2 μm.) (*C*) 4D (*x*, *y*, and *z*, time) representation of single-molecule position determinations during a sequence of 97 frames, with a color map showing the time of acquisition.

Fig. 5.4. 3D super-resolution imaging. (A) High concentrations of single molecules of DCDHF-V-PF4-azide in a thick PMMA sample image using the PALM/STORM/F-PALM method with the DH-PSF as described in the text. Color indicates total number of photons used for estimation after background correction. (B) Zoom-in of position estimations for molecules 1 and 2 (blue and red, respectively) separated by 14 nm (x), 26 nm (y), and 21 nm (z); Euclidean distance (green): 36 nm. (Scale bar: 20 nm.) (C) Image from activation cycle 1 showing molecule 1. (D) Image from later in cycle 1 confirming that molecule 1 bleached. (E) Image from activation cycle 2 showing molecule 2. (Scale bar: C–E, 1 μm.)

Fig. 5.5 : (a) Estimations of the z position of the DCDHF-V-PF$_4$ molecule featured in Fig. 5.2 of the main text. (b) Estimations of the z position of the fluorescent bead fiduciary in the sample, illustrating the z drift of the microscope and/or the z-piezo. (c) Fiduciary-corrected positions of the single molecule.

Fig. 5.6: The localization precision from single DCDHF-P (structure shown) molecules as a function of the number of photons used in the centroid estimation algorithm for the x (a), y (b), and z (c) directions. All measurements were made with acquisition times of 500 ms and the rms background noise in the samples was approximately 20 photons/pixel.

Fig. 5.7: Absorption (solid lines) and fluorescence (dashed and dotted lines) spectra of the DCDHF-V-PF4-azide dark fluorogen before and after photoactivation to the amino fluorophore. The short-wavelength absorption peak, which corresponds to the azido fluorogen, disappears after illumination with 385-nm light (0.3 mW/cm^2); the longer wavelength peak of the fluorescent amino compound grows in. Before photoactivation, pumping at 490 nm yields little fluorescence (dashed line); after activation with 385-nm illumination, pumping at 490 nm produces much brighter fluorescence (dotted line).

Figure 6.1. Experimental setup for polarization sensitive 3D super-resolution imaging with the double-helix point spread function (DH-PSF). PtK1 cells expressing PA-GFP are excited with the 488nm argon laser line and are photoactivated with a 405nm laser diode. The imaging path consists of two polarization channels that are modulated with a spatial light modulator (SLM) encoding the DH-PSF phase mask (bottom right inset). The inset in the middle shows PtK1 microtubules imaged in the horizontal and vertical channels with the standard PSF (SLM off) and with the DH-PSF (SLM on). M refers to mirrors; QWP is quarter wave plate; L_W is a 75mm wide-field lens; L_O is a 1.3NA objective; L_T is a 150mm achromatic lens; L_{S1}, L_{S2}, and L_{S3} are 250mm achromatic lenses; PBS is a broadband polarization beam splitter; HWP is a broadband half wave plate; EMCCD is an electron multiplying charge coupled device detector.

Figure 6.2. Plots DH-PSF rotation angle in the (a) horizontal and the (b) vertical channels obtained by moving a 40nm wide fluorescent microsphere in the axial dimension with 100nm steps. The DH-PSF rotates in opposite direction in the two channels. Scale bar: 1μm

Figure 6.3. (a) Gain in position localization precision obtained by combining position information from the two polarization channels. (b) 3D position histograms of a fluorescent bead showing improved precisions when horizontal (X_H, Y_H, Z_H) and the vertical (X_V, Y_V, Z_V) channel estimates are combined (X_C, Y_C, Z_C). $\sigma_H(X,Y,Z)=(2.6nm, 2.5nm, 6.1nm)$; $\sigma_V(X,Y,Z)=(2.5nm, 2nm, 5.6nm)$; $\sigma_C(X,Y,Z)=(2nm, 1.8nm, 4.5nm)$.

Figure 6.4. Position localization histograms of a (a) single PA-GFP molecule in the (b) X, (c) Y, and (d) Z dimensions. The average number of detected photons per image is only 246 photons. $\sigma_{PA-GFP}(X,Y,Z)=(13.2nm, 20.3nm, 42.8nm)$. Scale bar: 1μm

Figure 6.5. Polarization specific 3D super-resolution images of a PtK1 cell obtained from (a) horizontal and (b) vertical polarization channels. The super-resolution images from the two channels reveal polarization specific features of the cell. For example, the edge of the cell (pointed at by cyan dotted arrows) is more prominently

visible in the horizontal polarization channel, but not in the vertical polarization channel. Scale bars: 1μm

Figure 6.6. X and Y corrections of horizontal and the vertical channels due to aberration induced small systematic shift in the midpoint of the two PSF lobes.

Fig. 6.7. (a) Differential Interference Contrast (DIC) image of PtK1 cells, (b) Cross-polarized image of the same cells as in (a) showing negligible birefringence. Scale bars: 10μm

Fig. 7.1. Effect of pixel size. As the pixel size decreases for a given magnification (equivalently, as magnification increases for a given pixel size) in a photon-limited system, the DH-PSF is better sampled, but with a decrease in the number of photons per pixel. The optimal number of pixels sampling the DH-PSF depends on the SNR per pixel of the system.

Fig. 7.2. Effect of image background. As the image background increases for a given signal level, the gradient of the detected PSF (scaled to reach the detector's dynamic range for best CRB) decreases.

Fig. 7.3. Detector-limited PSFs with high (a) 1D, (b) 2D, and (c) 3D Fisher Information

Fig. 7.4. Quantitative phase microscopy using a structured-illumination DH-PSF system

Chapter 1

Introduction to Nanoscopy

"There's Plenty of Room at the Bottom" - Richard Feynman

1.1 Motivation

Nanoscopy is a rapidly evolving field that focuses on imaging and sensing properties at the nanometer scale. Studies at this scale are becoming increasingly important in both fundamental and applied sciences (Fig. 1.1). For example, in biology, many nanoscale intracellular structures (such as DNA, proteins, microtubules, etc.) dictate the organization and the function of an organism at micro and macro scales. In chemistry, nanoscopy is necessary to understand single molecule heterogeneities, which are usually lost at microscales due to ensemble averaging.
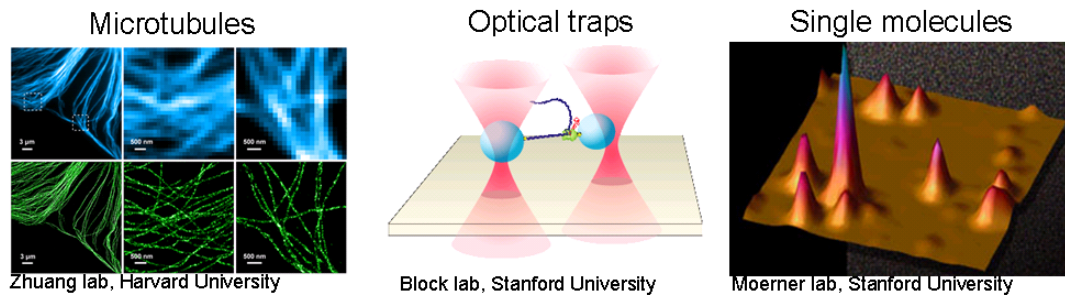
Fig. 1.1. Scientists are now keen on understanding nature at the nanoscale, for events at these scales determine properties at the micro and macro scales.

In physics, nanometer scale precisions are required to investigate forces acting on micro and nano particles. In engineering, nanometer scale studies are critical for nanomanufacturing.

1.2   State of the art in nanoscopy

The state of the art in nanoscopy can broadly be classified into non-optical methods and optical methods. Non-optical methods (Fig. 1.2) include transmission and scanning electron microscopy (TEM 1931; SEM 1935; *Nobel prize in physics - 1986*), scanning tunneling microscopy (STM; 1981; *Nobel prize in physics - 1986*), atomic force microscopy (AFM; 1986), and far-field diffraction based techniques such as X-ray crystallography (1912; *Nobel prize in physics - 1914*). Although termed as "micro"scopes, these techniques can routinely resolve subnanometer scale objects. Electron microscopes achieve atomic scale resolutions because the DeBroglie wavelength of electrons is orders of magnitude smaller than a nanometer.

Fig. 1.2. Non-optical nanoscopy techniques achieve nanometer scale resolutions either by using electrons, X-rays, or by scanning with nanometer scale tips. SEM is scanning electron microscope; TEM is transmission electron microscope; STM is scanning tunneling microscope; AFM is atomic force microscope.

AFMs and STMs use nanometer scale tips in close proximity to the sample being imaged to measure sample properties (forces, tunneling current) at the location of the tip. The resolution of STM and AFM primarily depend on the size of the tips and the scanning resolution of the sample. Far-field diffraction based nanoscopy techniques measure the diffraction pattern of nanoscopic structures (such as crystals) and use this diffraction information to estimate nanoscale structural properties. Non-optical techniques such as SEM and TEM are powerful tools for materials inspection, but their sample preparation constraints and high electron energies make them unsuitable for *in vivo* biological imaging. Surface scanning techiques such as STM and AFM are good in providing high-resolution profiles of surface properties, but are not suitable for three-dimensional (3D) imaging or to study optical properties at small scales.

Optical techniques (Fig. 1.3) operate with visible light, which is known to be less harmful to biological cells than electrons or X-rays. Further, by making target-specific fluorescence imaging possible, optical techniques have given biologists the ability to differentiate a single protein of interest from a number of other intracellular
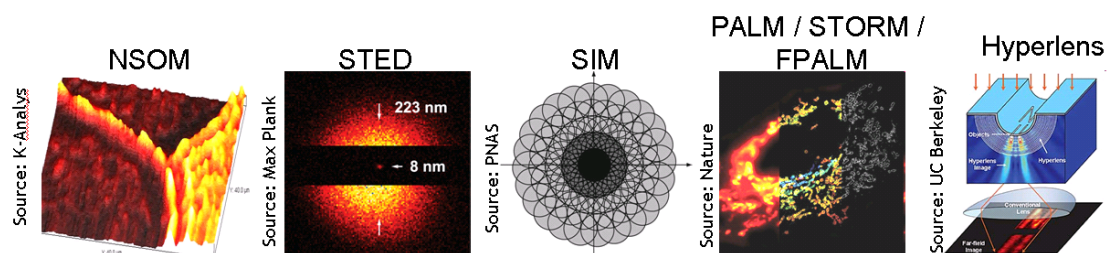
Fig. 1.3. Optical nanoscopy methods achieve nanometer scale resolutions by overcoming the far-field diffraction barrier, either by capturing evanescent waves (NSOM, Hyperlens), or by using active illumination (SIM), and/or by controlling the molecular properties of samples (STED, PALM/STORM/FPALM). See text for further explanation of these techniques.

structures (*Nobel prize in chemistry - 2008*).

Optical nanoscopy methods include near-field scanning optical microscope (NSOM; 1984), stimulated emission depletion microscope [1] (STED; 2000), structured illumination microscope [2] (SIM; 2000), single molecule photoactivation based techniques such as photoactivated localization microscopy [3] (PALM; 2006), stochastic optical reconstruction microscopy [4] (STORM; 2006), fluorescence photoactivated localization microscopy [5] (FPALM; 2006), and hyperlens [6] (2007). All of these techniques overcome the so called optical diffraction barrier that restricts the resolution of conventional optical microscopes to ~200nm in the transverse (x,y) dimensions.

NSOM achieves nanometer scale transverse resolutions by interacting with the evanescent waves that exist very close to the sample. It is a surface scanning technique and is consequently not suitable for probing the interior of 3D objects. Poor reproducibility in tip fabrication and low power throughput further affect this technique. Also, being a two-dimensional scanning technique, NSOM is fundamentally slow in operation.

Hyperlens is an anisotropic lens consisting of a periodic stack of silver and aluminum oxide. When placed close to the sample, the hyperlens converts evanescent waves into propagating waves, which can then be imaged in the far-field. Because evanescent waves decay exponentially in the axial dimension, lossless hyperlenses still need to be developed for accomplishing 3D imaging. In practice, hyperlenses have low space-bandwidth product and very small working distances.

STED is a scanning technique that illuminates a sample point simultaneously with two beams designed to effectively reduce the size of the point spread function. While one of these two beams excites fluorophores within a diffraction-limited spot, the other (donut shaped) beam depletes the excited fluophores in the outer regions of the diffraction-limited spot of the first beam, effectively resulting in fluorescence emission from a region smaller than the diffraction limit. Because STED does not use all excited molecules (those in the outer regions of the diffraction-limited spot) for imaging, it inherently results in high phototoxicity and bleaching rates.

SIM projects sinusoidal patterns on the sample to make spatial frequencies outside the pass-band of a microscope participate in the image formation. It can at best improve the resolution by a factor of two, but saturated illumination patterns can be used to achieve better resolution. However, the saturated SIM approach suffers heavily from decreased signal levels in higher diffraction orders of the pattern, resulting in low signal-to-noise reconstructions.

PALM, STORM, and FPALM photoactivate (turn on) and localize different sparse molecule subsets at different times, and combine the position information of all photoactivated molecules to obtain images with nanoscale resolution. In comparison to NSOM, PALM/STORM/FPALM has a large working distance, does not employ spatial scanning, and can be extended to the third dimension. Unlike STED, PALM/STORM/FPALM detects every excited molecule, and therefore has reduced phototoxicity and bleaching rates. The reported resolution of PALM/STORM/FPALM is better than SIM.

The last couple of years (2008-2009) have witnessed significant progress to extend STED, SIM, and PALM/STORM/FPALM to simultaneously achieve super-resolution imaging in all three spatial dimensions. isoSTED (2008) extended STED to 3D by creating a 40-45nm diameter spherical focal spot [7]. 3D-SIM (2008) pushed the structured-illumination technique to explore the third dimension [8]. PALM/STORM/FPALM was pushed to explore the third dimension by using astigmatism [9] (2008), two focal planes [10] (biplane; 2008), two-photon processes [11] (2008), and interferometry [12] (2009).

isoSTED and 3D-SIM, although extended to sense the third dimension, fundamentally suffer from the same drawbacks as STED and SIM, respectively, as described above. The astigmatism and biplane methods of extending PALM/STORM/FPALM suffer from a limited axial range of operation. The two-photon based technique does not fundamentally improve the axial resolution, but demonstrated transverse super-resolution imaging of micron-scale axially separated slices of an object. The interferometry based extension of PALM/STORM/FPALM also suffers from a limited range, but achieves better axial resolutions than astigmatism and biplane methods. However, it is requires a complex modification to existing two-dimensional PALM/STORM/FPALM systems, involving dual objectives, a custom-designed three-way beam splitter, and three detectors.

1.3   Thesis overview

This thesis introduces a 3D nanoscopy paradigm based on a 3D point spread function (PSF) that was specifically designed for 3D position estimation and imaging.

With an insight on the importance of the phase of Gauss-Laguerre modes over their amplitudes, chapter 2 develops a multi-domain optimization procedure that generates a PSF (termed double-helix PSF or DH-PSF) that exhibits two rotating lobes within a limited region in space with over 30 times higher light efficiency than traditional rotating PSFs. DH-PSF is then experimentally demonstrated with a spatial light modulator (SLM).

Chapter 3 shows with an information theoretical analysis that the DH-PSF is fundamentally better than a standard PSF for 3D position localization in detector-limited (bright field, dark field) systems. With a single image of a bright-field DH-PSF microscope, the positions of multiple scattering microparticles are localized with better than 10nm precision in three dimensions. This chapter also introduces dark-field DH-PSF microscopy.

Chapter 4 introduces DH-PSF fluorescence microscopy, and demonstrates three dimensional tracking and velocimetry of fluorescent microspheres with nanometer scale precisions. Further, this chapter shows with information theoretical analysis that DH-PSF systems, on an average, carry more (Fisher) information than standard systems in the photon-limited regime.

Chapter 5 demonstrates single-molecule 3D super-resolution imaging by breaking the optical diffraction limit by over an order of magnitude in all three dimensions. Single fluorescent molecules were localized in 3D with nanometer scale precisions

using a DH-PSF fluorescence microscope, and super-resolution imaging was achieved by photoactivating and localizing different sparse subsets of photoactivatable fluorescent molecules at different times.

Chapter 6 introduces polarization sensitive 3D nanoscopy using a DH-PSF nanoscope, and resolves polarization-specific intracellular structures inside a PtK1 cell. Light from photoactivatable green fluorescent protein (PA-GFP) molecules are decomposed into orthogonal polarization imaging channels, which are then separately modulated and detected with a single SLM and a single electron multiplying charge coupled device detector. Further, this chapter demonstrates that localization precisions can be improved by optimally combining information from the two channels.

Chapter 7 suggests some future work on approaching the fundamental limits of DH-PSF nanoscopy, quantifying the experimental factors affecting the Cramer-Rao Bound, achieving unlimited precisions with detector-limited systems, and on applying the DH-PSF to quantitative phase imaging.

Chapter 8 discusses and concludes this thesis.

Chapter 2

Double-helix Point Spread Function

Rotating point spread functions (PSFs) present invariant features that continuously rotate with defocus and are important in diverse applications such as computational imaging and atom/particle trapping. However, their transfer function efficiency is typically very low. We generate highly efficient rotating PSFs (termed Double-helix PSF) by tailoring the range of invariant rotation to the specific application. The PSF design involves an optimization procedure that applies constraints in the Gauss-Laguerre modal plane, the spatial domain, and the Fourier domain. We observed over thirty times improvement in transfer function efficiency. Experiments with a phase-only spatial light modulator demonstrate the potential of high-efficiency rotating PSFs.

2.1   Introduction

A delicate balance between vortex (phase singularity) charge and the Gouy phase of a superposition of beams produces the so-called rotating beams. These beams present an intensity distribution that continuously rotates about the optical axis upon propagation [13,14,15,16,17,18]. Combinations of Gauss-Laguerre (GL) or Bessel beams have been used for optical manipulation of atoms and microparticles [19,20,21]. Because each point in the transverse cross sections of *rotating* beams

describes a spiral trajectory, they are attractive for such particle manipulation applications. The same optical elements that generate rotating beams can be used to engineer the point spread functions (PSFs) of imaging systems to rotate with defocus. These rotating PSFs significantly increase the sensitivity of depth estimation and are the foundation of a new passive ranging principle named "depth from diffracted rotation" [22].

The main disadvantage of existing methods to implement rotating PSF systems is low light efficiency, which makes them inappropriate for photon limited applications. In this chapter, we introduce a new type of PSF named "double-helix PSF" (DH-PSF) that solves this low efficiency problem. Unlike exact rotating PSFs, DH-PSFs present rotating cross sections only in a predetermined region of space, which allows for additional degrees of freedom to be used towards a phase-only implementation of the transfer function and its optical element.

The rest of this chapter is organized as follows: In section 2, we review the properties of rotating PSFs and establish their limitations. Section 3 introduces the new three-dimensional DH-PSFs. Section 4 describes the design methodology, and section 5 analyzes the spatial and spectral properties of DH-PSFs through modeling and experiment.

2.2   Rotating point spread functions

Rotating PSFs are 3D optical responses with circularly asymmetric transverse profiles that continuously rotate with defocus (Fig. 2.1). They are conveniently represented in

the GL modal plane as a linear superposition of GL modes that lie along a straight line [15]. A rotating PSF system can be implemented by introducing a mask that encodes the rotating PSF transfer function in the Fourier plane of a standard imaging system. For example, the superposition of modes with indices (1,1), (3,5), (5,9), (7,13), (9,17) forms a useful rotating PSF transfer function as shown in Fig. 2.2 [22], where all the modes have equal energy. When such a GL superposition is implemented as the transfer function of an imaging system, the PSF of the system rotates with defocus (Fig. 2.1). The rate of rotation, which is proportional to the slope of the straight line chosen in the GL modal plane, is maximum in the focal region. The transfer function of a rotating PSF, being an eigen-Fourier transform, is a scaled version of the PSF itself.
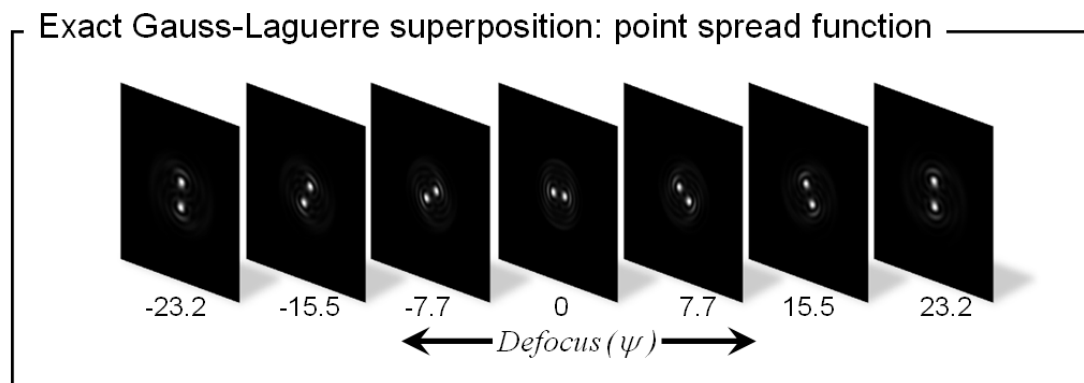
Figure 2.1. Exact rotating PSF formed by superposing Gauss-Laguerre modes (1,1), (3,5), (5,9), (7,13), (9,17). [See movie from Opt. Exp. **16**, 3484 (2008)]

The main disadvantage of existing rotating PSFs is their very low transfer function efficiency, which is defined as the ratio of the energy in the rotating PSF main lobes to the energy incident on the mask. This is fundamentally due to two

reasons: 1) the amplitude of the rotating PSF transfer function creates highly absorptive masks, and 2) part of the energy in the rotating PSF is delivered to the side lobes, which are usually not used. In the example of Fig. 2.2, the transfer function efficiency is only about 1.8%; meaning that only 1.8% of the energy incident on the rotating PSF system from a point source actually contributes to the main lobes of the PSF.
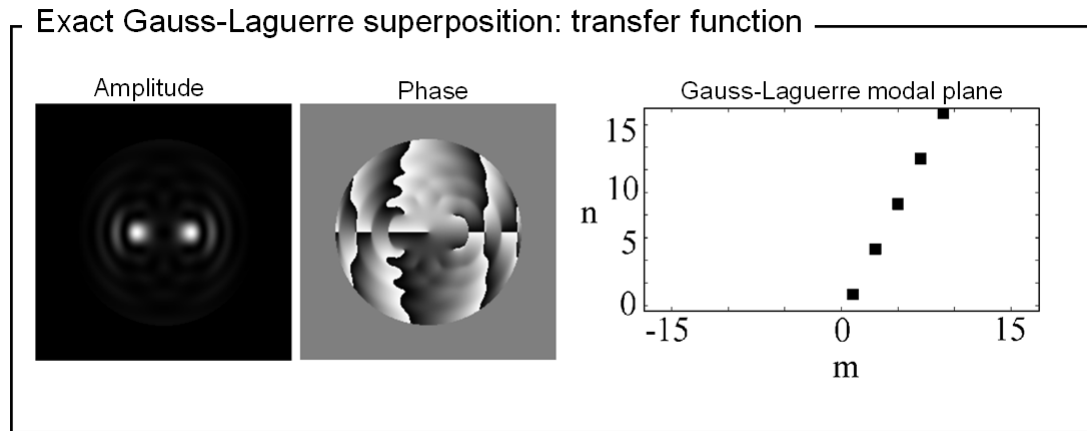
Figure 2.2. Transfer function mask formed by superposing Gauss-Laguerre modes (1,1), (3,5), (5,9), (7,13), (9,17), which fall along a straight line in the Gauss-Laguerre modal plane.

Adding to — and independent of — this low efficiency problem is the encoding method of the amplitude and phase components of the transfer function that often results in unused diffraction orders, causing further loss of light. Because of the above mentioned inherent factors, current rotating PSF systems are not suitable for photon-limited applications.

2.3 Double-helix PSF: high efficiency rotating PSF

We solve the rotating PSFs' low efficiency problem by designing DH-PSFs with the following key features: 1) The rotating response appears only within a limited volume instead of the whole 3D space, 2) The main features of the PSF rotate but the entire cross section is only approximately invariant within the volume of interest.

A DH-PSF specifically designed for depth estimation presents two main lobes that rotate continuously with defocus. The key advantage of this DH-PSF is that its transfer function efficiency is over 30 times higher than in the case of the exact rotating PSF. Unlike previous rotating PSFs, DH-PSFs have phase-only coherent transfer functions and hence can be implemented with non-absorbing masks. DH-PSFs are engineered using an iterative optimization procedure to have the following attributes: 1) a continuous rotation of the main lobes with defocus within a specified range, 2) maximum energy directed towards the main lobes, and 3) the transfer function modulates only the phase (no absorption).

2.4 Double-helix PSF design by iterative optimization

It is straightforward to design a phase mask for achieving any arbitrary complex field on any one particular transverse plane [23]. In such a design, the fields in all other axial planes would be dictated by diffraction. However, in the DH-PSF design, we seek a phase mask that generates a particular intensity distribution on one transverse plane and continuously rotated versions of the intensity distribution on the successive planes. In other words, we are looking for a 2D phase mask to generate a specific 3D

intensity distribution. Although a 2D mask cannot generate any arbitrary 3D *complex*

field (i.e. having both an arbitrary intensity *and* an arbitrary phase), it is known that

the available degrees of freedom can be optimized to obtain any arbitrary 3D intensity

distribution (without arbitrary phase) subject to physical limitations [24]. Because of

the strong constraints on the intensity of the transfer function (phase-only) and the

intensity of the 3D PSF (rotating main lobes with maximum energy), the only degrees

of freedom in the DH-PSF design are 1) phase of the transfer function and 2) phase of

the 3D PSF. One method for achieving this could be to use the block-iterative

weighted projections algorithm [24,25]. To apply this method in three dimensions,

each 2D transverse slice of a desired 3D intensity distribution is applied as a

constraint to the mask. A continuous 3D distribution requires a suitable axial

sampling rate. In the proposed design, we substantially reduce the number of required

constraints by starting with an efficient initial estimate and by iteratively enforcing

constraints in three different domains; namely the GL modal plane, the spatial

domain, and the Fourier domain. While the idea of optimizing a 3D optical response

over a finite domain is not new, the combination of spatial, spectral, and GL plane

constraints has not been attempted before.

2.4.1 Initial estimate

We now describe the initial estimate that is fed into the iterative optimization

algorithm. Typically, the phase of a GL mode or a GL mode superposition determines

the behavior of the beam to a larger extent than its amplitude. For example, when the

amplitude of a GL mode is replaced by a constant amplitude, the beam still closely

resembles the original mode in the far field. Consider again the rotating PSF (Fig. 2.1) and its transfer function (Fig. 2.2). When the amplitude of the GL superposition is removed from the transfer function (Fig. 2.3), the PSF still exhibits two main lobes that rotate continuously with defocus (Fig. 2.4). This seemingly surprising result can be understood by representing the transfer function in the GL modal plane. When the phase of the exact GL superposition is decomposed into its fundamental GL basis functions in the GL modal plane, it forms a cloud centered along the same straight line as the exact superposition (Fig. 2.3). Since the slope of the major axis of the cloud is same as the straight line of the exact GL superposition, the rate of rotation of the new PSF remains the same.
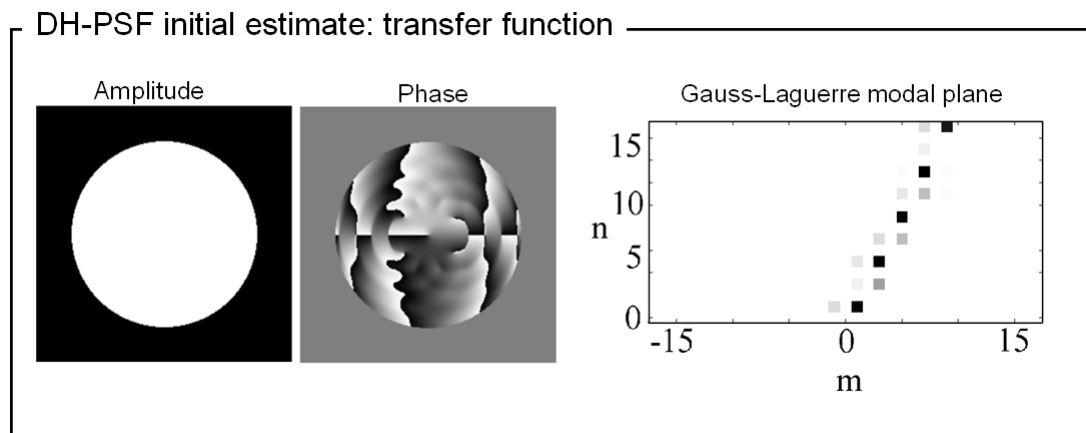
Figure 2.3. Transfer function of DH-PSF initial estimate, and its GL modal plane decomposition, which forms a cloud around the GL modal plane line in Figure 2.2.

The observation that a PSF with two rotating main lobes can be formed by a cloud centered around a line in the GL modal plane relieves us from the restriction of picking modes along just one line in the GL modal plane. Thus, by merely ignoring

the amplitude of the exact GL superposition, we satisfy two of the three DH-PSF

attributes — phase-only transfer function and the continuous rotation of the PSF main

lobes with defocus. Although this PSF offers 41.9% transfer function efficiency, it is

not optimal in terms of efficiency and suffers from high side lobes in the focal region.

Hence, we use this phase-only transfer function as the initial estimate in our

optimization procedure.
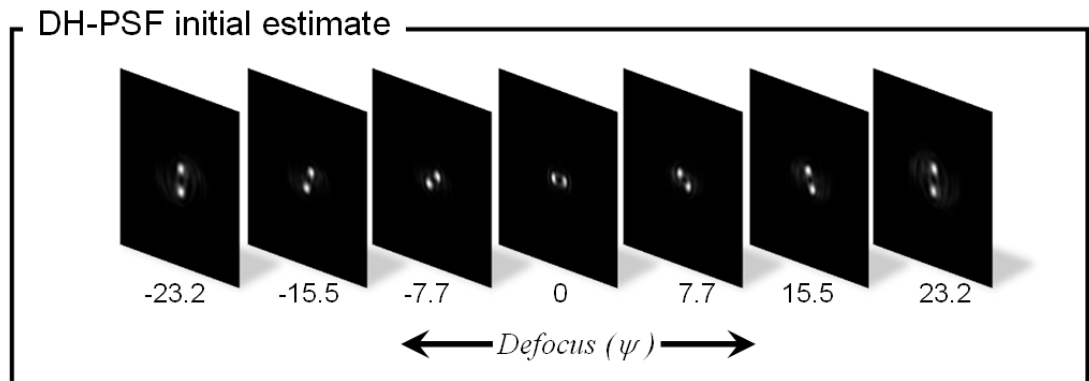
Figure 2.4. DH-PSF initial estimate as a function of the defocus
parameter (ψ) [see section 3.8 for more information on ψ]. This PSF
is generated by a mask that is obtained by retaining just the phase of
the exact GL superposition, and replacing the superposition's
amplitude with a disc. [See movie from Opt. Exp. **16**, 3484 (2008)]

2.4.2. Optimization constraints

The iterative optimization procedure starts with the above transfer function estimate

and repeatedly enforces constraints specifically designed for achieving PSF rotation,

maximum energy in the PSF main lobes, and a phase-only transfer function.

For enforcing PSF rotation, we decompose the transfer function into GL modes

and multiply the GL modal plane decomposition by a weight function to boost the

modes that lie on a cloud around the line defining the exact rotating PSF. The expression for this cloud weight function is obtained from a function $d(m,n)$ defined as,

$$d(m,n) = \prod_{k=1}^{N} [(m-m_k)^2 + (n-n_k)^2]^p, \qquad (1)$$

where m and n are the indices of the GL modal plane, m_k and n_k are the m and n indices of the kth GL mode along the rotating PSF line, N is the number of modes selected along the rotating PSF line, and p is a parameter that determines the width of the cloud. The weight function $w_{gl}(m,n)$ is directly obtained from $d(m,n)$ as

$$w_{gl}(m,n) = max[d(m,n)] - d(m,n).$$

To maximize the energy in the main lobes of the entire 3D PSF, we apply constraints to boost the PSF main lobes at nine defocus values spanning the $[-\pi/2, \pi/2)$ rotation range of the 3D PSF. Specifically, we compute the coherent PSF for a particular defocus value and multiply it by a weight function designed to boost the main lobes at that particular defocus. The weight function consists of two spatially separated Gaussians whose locations and widths are the same as those of the main lobes of the rotating PSF. Due to the continuous rotation of the rotating PSF along with varying scale, the spatial width and the locations of its main lobes change continuously with defocus. Consequently, the weight functions also need to change for different defocus values. We construct nine different weight functions for the nine different slices of the 3D PSF. The number of axial constraints needed here (nine) is

not large because of the fact that the constraint in the GL modal plane already ensures continuous rotation.

The final constraint is to enforce that the transfer function is a phase-only function in the Fourier domain. Even though the initial estimate was a phase-only transfer function, the modal plane and the spatial domain constraints affect the transfer function to include amplitude modulation. However, because the preceding two constraints only boost already existing features of the PSF, the modified transfer function is close to being phase-only. Therefore, the third constraint enforces the transfer function to be phase-only by replacing its amplitude with a constant amplitude function.

2.5 Optimization Results

The above three constraints are repeatedly enforced in an optimization loop. After a few iterations, a DH-PSF mask that approximately satisfies all three of its desired attributes is obtained. The desired attributes are monitored at the end of each of the iterations — if the modes form a cloud in the GL modal plane, if the peak intensities of the main lobes are increasing, and if the mask is phase-only. The phase-only attribute is quantified by computing the mask's transparency (T), defined as,

$$T = \sum_x \sum_y \left| H_i(x,y) \right| \Big/ \sum_x \sum_y C(x,y),\tag{2}$$

where $H_i(x,y)$ is the complex mask immediately before enforcing the phase-only

constraint and $C(x,y)$ represents a clear aperture of the same size.

The evolution of the mask phase, the GL modal plane, the main lobe peak intensity,

and T with each of the iterations is shown in Fig. 2.5.
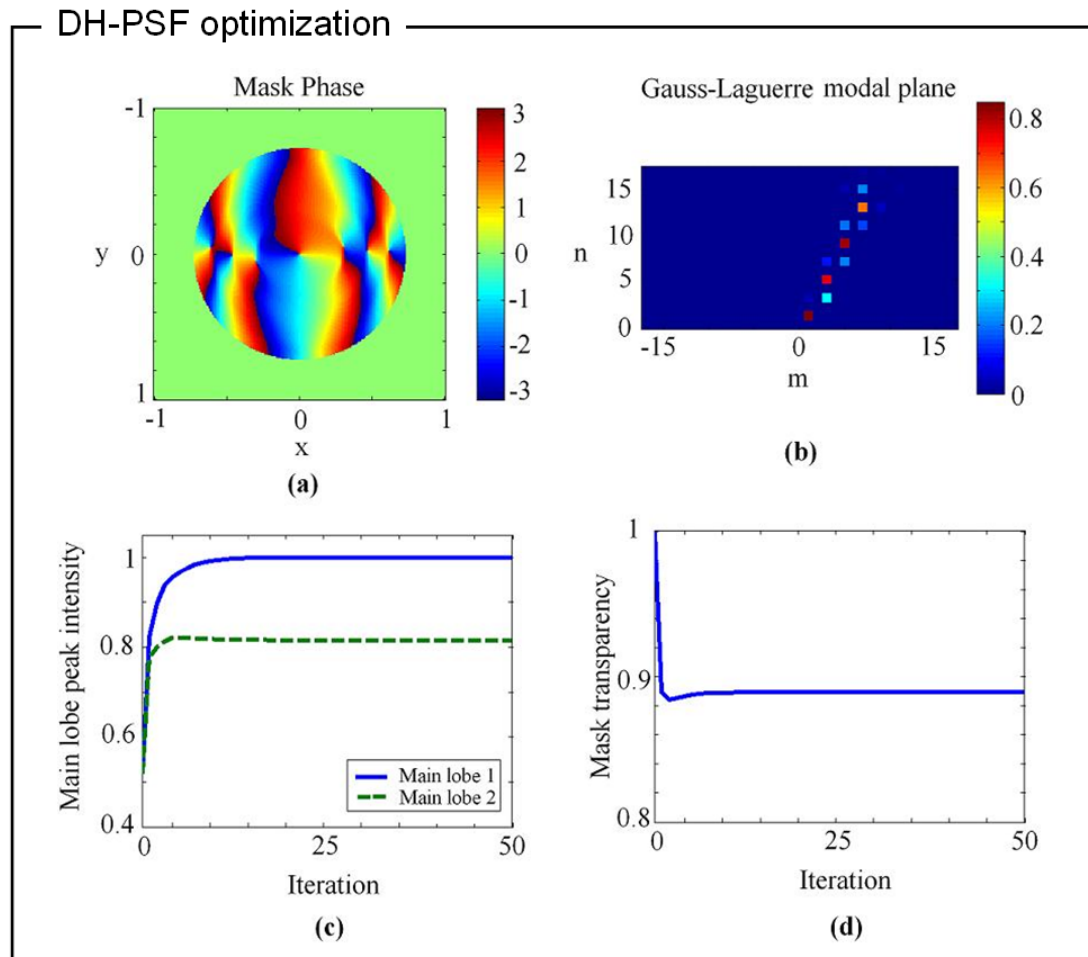
Figure 2.5. Evolutions of (a) mask phase, (b) GL modal plane, (c) main lobe peak intensity, and (d) mask transparency during the iterative optimization procedure. [See movie from Opt. Exp. **16**, 3484 (2008)]

While the continuous phase modulations of the mask disappear during the optimization process, the phase singularities remain, suggesting that phase singularities at appropriate locations are principally responsible for the rotation of the PSF. The GL modal plane evolves by picking up different weights for the modes on a cloud around the straight line of the exact rotating PSF. Although the two main lobes were equally boosted by the spatial domain constraint, one of the main lobes (main lobe 1) grows faster than the other main lobe (main lobe 2). Since the constraints in the GL modal plane and in the spatial domain did not preserve the phase-only attribute of the initial estimate, T drops immediately after the first iteration. T eventually increases because of the phase-only constraint in the Fourier domain. After 20 iterations, the main lobe peak intensities and T saturate. We then obtain the phase-only DH-PSF mask (Fig. 2.6) by stopping the iterative optimization process immediately after applying the phase-only Fourier domain constraint.
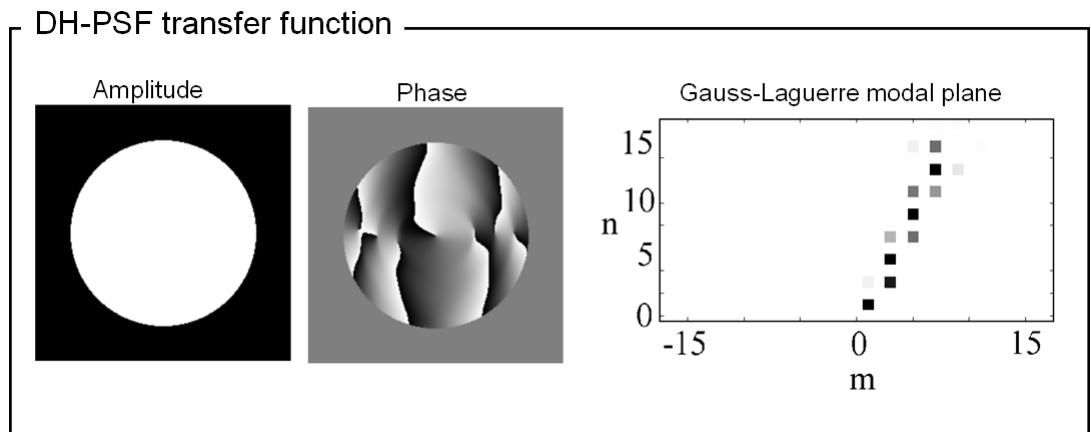
Figure 2.6. DH-PSF transfer function obtained from the iterative obtimization procedure, and its GL modal plane decomposition, which forms a cloud around the GL modal plane line in Figure 2.2. The DH-PSF transfer function does not have any amplitude component, and consequently is not absorptive.

The DH-PSF has two main lobes that rotate continuously with defocus (Fig. 2.7) as suggested by its mask's modal decomposition (Fig. 2.6). The transfer function efficiency of the exact rotating PSF and the DH-PSF are 1.8% and 56.8%, respectively. Hence, the main lobes of the DH-PSF have over 30 times more energy than the exact rotating PSF. Further, compared to a rotating PSF mask, the DH-PSF mask is easier to fabricate because of its phase-only attribute and also because the phase modulation becomes smoother in the optimization process.
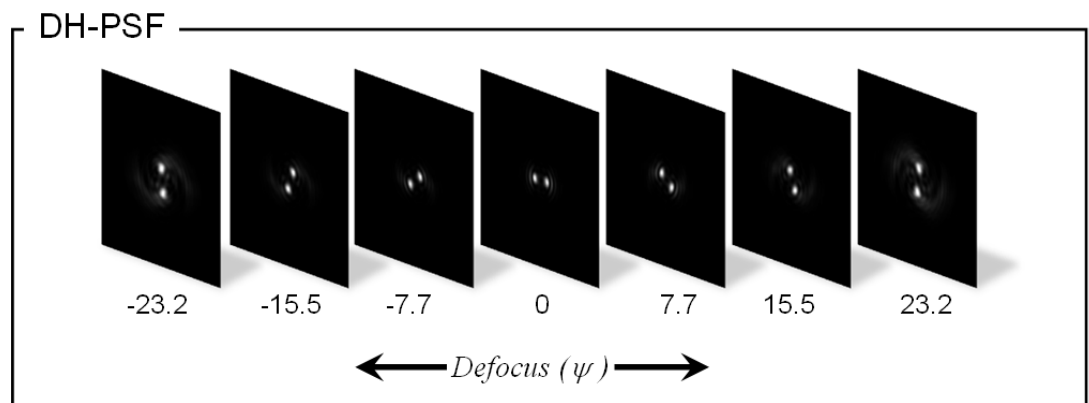
Figure 2.7. DH-PSF illustrated as a function of the defocus parameter (ψ). DH-PSF is generated by a mask that is obtained from an optimization procedure that simultaneously optimizes the PSF in the Gauss-Laguerre, Fourier, and spatial domains. [See movie from Opt. Exp. **16**, 3484 (2008)]

2.6 Effect of wavelength change

Although the DH-PSF design used a coherent transfer function model, it applies equally well for an incoherent imaging system because the incoherent PSF is the

modulo-squared of its coherent counterpart. However, because the mask is designed for one particular wavelength, it is interesting to analyze its wavelength (λ) dependence. Wavelength dependence arises from four factors: 1) phase retardation of a mask is $2\pi n t(x,y)/\lambda$, where n and $t(x,y)$ are the mask's refractive index and thickness function, respectively; 2) material dispersion; 3) defocus is inversely proportional to λ; and 4) PSF size is proportional to λ. (3) and (4) are the result of diffraction upon wave propagation.

As an example, the effect of using a BK7 glass DH-PSF mask designed for a wavelength of 550nm with the wavelengths 500nm, 550nm, and 600nm is shown in Fig. 2.8. The rotation angles were determined by calculating the 3D PSF for each wavelength from the transmittance function produced by the mask at the corresponding wavelength. For all three wavelengths, the PSF exhibits two main
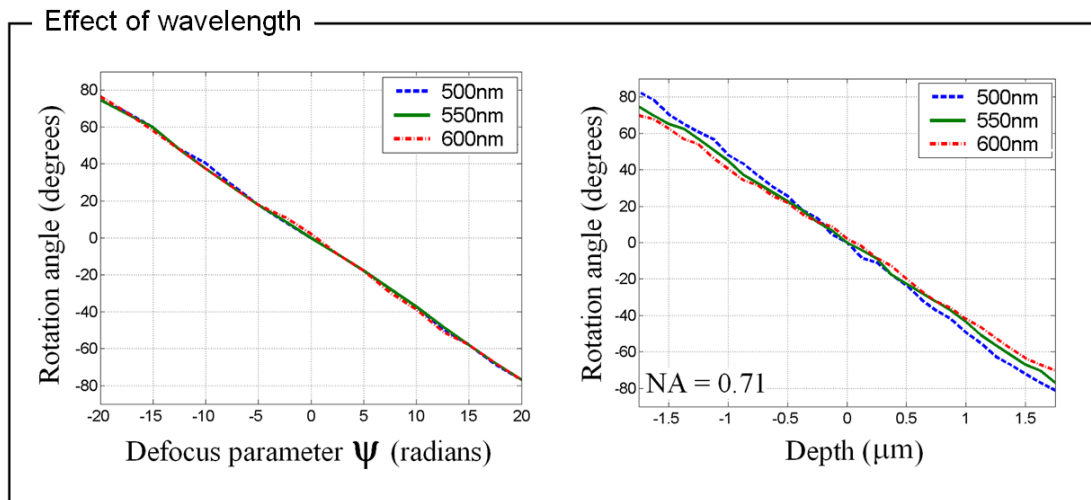
Figure 2.8. A DH-PSF mask designed for a wavelength of 550nm, when used with the wavelengths 500nm and 600nm, exhibits the same rotation rates as function of defocus parameter (ψ) and slightly different rotation rates as a function of depth (NA=0.71).

 lobes that rotate continuously. The rates of rotation are essentially the same for all three wavelengths (Fig. 2.8), when plotted as a function of the defocus parameter (ψ). However, as a function of depth, the rotation rate increases when the mask is used with wavelengths smaller than its design wavelength, and decreases when used with wavelengths greater than the design wavelength. This is exemplified in Fig. 2.8 for a unity magnification system with 0.71 numerical aperture (NA).

2.7   Double-helix PSF phase mask implementation

   DH-PSF mask can be fabricated either as continuous phase mask, or as a mask with quantized phase levels. Quantization effects are minimal, as can be seen from the comparison of the PSFs of a 4-level phase quantized mask and a continuous phase mask in Fig. 2.9. Such a phase quantized mask with small number of phase levels can be fabricated easily using lithography, and can be mass produced using precision molding.

   When a spatial light modulator (SLM) is used to encode the DH-PSF mask, care needs to be taken to avoid any unmodulated light from affecting the quality of the DH-PSF. Specifically, an SLM with less than 100% fill factor creates an undesirable on-axis lobe that lies between the two DH-PSF lobes. A significant on-axis lobe can seriously affect position estimation accuracies. A solution to this problem is to implement a blazed DH-PSF phase mask (a linear phase is added to the phase mask and the result is phase wrapped) on the SLM. This mask physically pushes the desirable DH-PSF response away from the unmodulated on-axis lobe. It is important

to note that such a blazed encoding makes the DH-PSF mask chromatic, restricting it to narrowband applications. Further, phase SLMs are designed to operate on one linear polarization, a constraint that requires the introduction of a crossed-polarizer to prevent any unmodulated light (with polarization orthogonal to the SLM polarization) from reaching the detector. When the light emitted by the sample is not polarized in the right direction, the crossed polarizer results in absorption, which adds to the overall losses of the system.
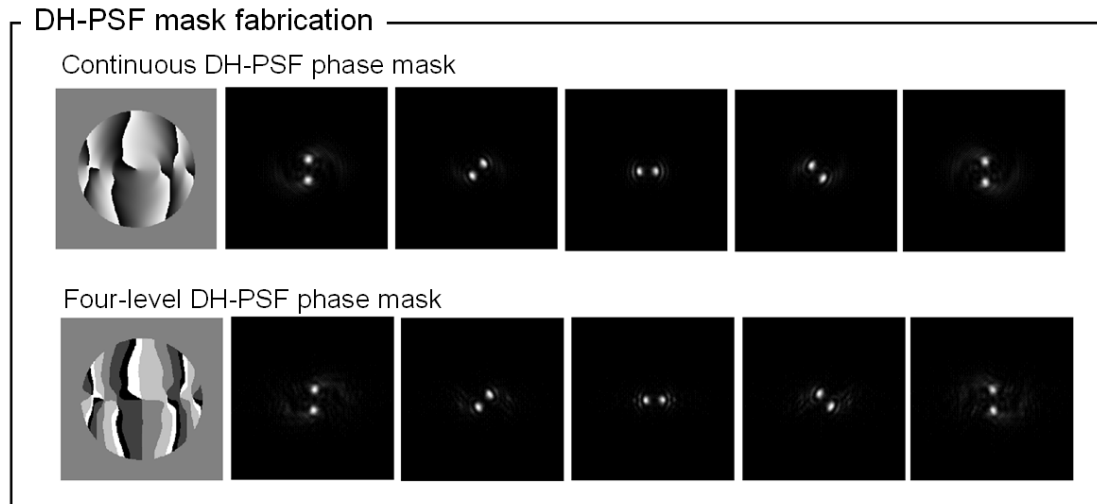
Figure 2.9: Phase-only DH-PSF masks and their PSFs at different defocus values: a) exact DH-PSF mask with continuous phase levels, b) 4-level phase quantized DH-PSF mask also shows two rotating lobes.

2.8 Experimental demonstration of double-helix PSF

For experimental demonstration (Fig. 2.10), we implement DH-PSF with a reflective phase-only spatial light modulator (SLM). Because of the sampling of the phase function by the SLM's pixels, the SLM produces multiple orders, of which the 0th
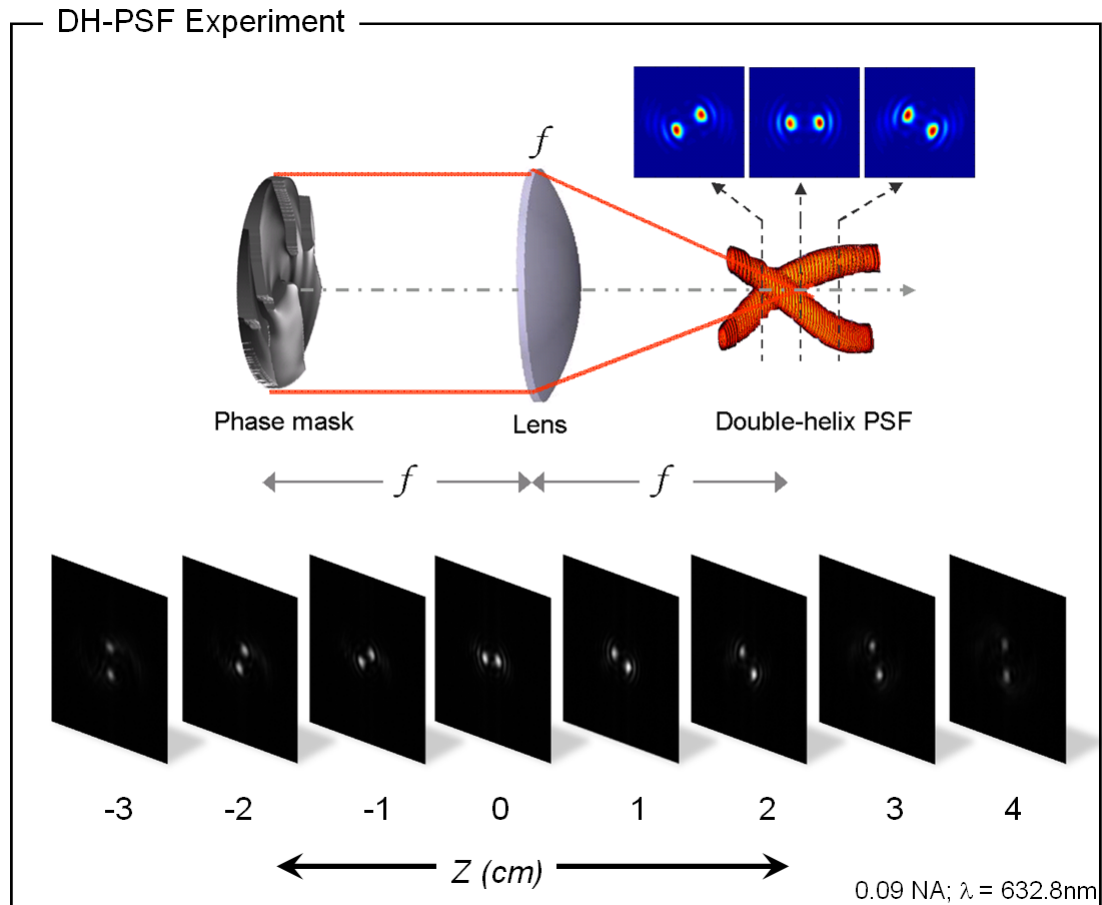
Figure 2.10. Experimental observation of the DH-PSF by focusing a collimated HeNe laser beam with a 0.09NA lens, after the beam reflected off of a phase-only spatial light modulator encoding the DH-PSF phase mask. [See movie from Opt. Exp. **16**, 3484 (2008)]

order has the highest energy. In order to avoid on-axis effects due to the SLM's non-ideal modulation, a blazed DH-PSF mask is used for the experiments of this chapter, and those of chapters 3 and 4. However, the experiments in the chapters 5 and 6 of this thesis used an on-axis mask (no blaze) with an SLM having close to 100% fill factor.

A collimated light with wavelength 632.8nm is incident on the SLM and a 0.09 NA lens Fourier transforms the 0th order of the SLM. The PSF at different axial distances shows two continuously rotating main lobes (Fig. 2.10) with 37.5% transfer function efficiency. The experimental efficiency is not as high as the theoretical value (56.8%) because of the non-ideal response of the SLM.

2.9   Summary

In this chapter, we introduced DH-PSFs, described their design methodology, analyzed their spatial and frequency response, and demonstrated them experimentally with an SLM. We showed that DH-PSFs can offer over thirty times higher efficiency than the exact rotating PSFs.

The use of an SLM for implementing the DH-PSF phase mask has the convenience of rapidly implementing masks with different sizes and for different wavelengths, but can be inefficient due to the polarization-sensitive nature of liquid crystal SLMs. We address this efficiency problem in chapter 6.

Chapter 3

3D Localization in Detector-limited Double-helix Microscopes

Accurate estimation of the three-dimensional (3D) position of particles is critical in applications such as biological-imaging, atom/particle-trapping, and nano-manufacturing. With the knowledge of an imaging system's point spread function (PSF), a particle can be localized with much higher accuracy than the Rayleigh spatial resolution limit. Using an information-theoretical analysis and an experimental demonstration, this chapter shows that a detector-limited double-helix PSF system is fundamentally better than a standard imaging system for three-dimensional position localization, and has the potential to reach into subnanometer accuracies. The gain in accuracy in detector-limited DH-PSF systems occurs in all three dimensions throughout the axial range of interest.

3.1 Introduction

Three-dimensional (3D) position localization is required to investigate the structure and dynamics of freely moving particles in a 3D volume. The particles under investigation could be biological cells, colloidal spheres, or even fluorescent single molecules. For example, by determining the position of a particle at different times, its trajectory in a 3D volume can be tracked [26,27,28] or optical traps can be guided

to restrict the motion of the particle [29]. The positions of photoactivated fluorescent molecules can also be combined to accomplish imaging at the molecular level [30, 3,4,5].

While traditional imaging systems are primarily designed for imaging a two-dimensional (2D) slice of a 3D object, they nevertheless also encode the third (axial) dimension in the form of defocus blur. The transverse (X, Y) position of an object point can be determined from the location of its point spread function (PSF) and the axial (Z) position can be determined from the amount of defocus in the PSF [27,31]. Because of noise in imaging, fine discrimination between the 3D positions of two objects is possible only if the corresponding 2D responses are significantly different. In fact, as will be shown below, the accuracy of position estimation in a particular dimension is related to the magnitude of the PSF's gradient along that dimension. A PSF exhibiting sharp variations in all three dimensions is therefore required for accurate 3D position estimation. Unfortunately, PSFs of conventional imaging systems barely change along the depth of field, resulting in poor localization accuracy in the axial dimension [Fig. 3.1(a)].

Axial accuracy can be improved by defocusing the system to operate away from the depth of field [27], but this comes at the cost of degrading the transverse position accuracy of the system and seriously limiting the axial range of operation (see Sec. 2.1). Because an aberration corrected standard PSF is essentially symmetric to either side of the focal plane, unambiguous axial position estimation, albeit with lower accuracy, is possible only within a limited range. To solve this problem, astigmatic

PSFs have been proposed to create opposite PSF orientations to either side of the focal plane [26,9], but they do not fundamentally improve the axial accuracy.
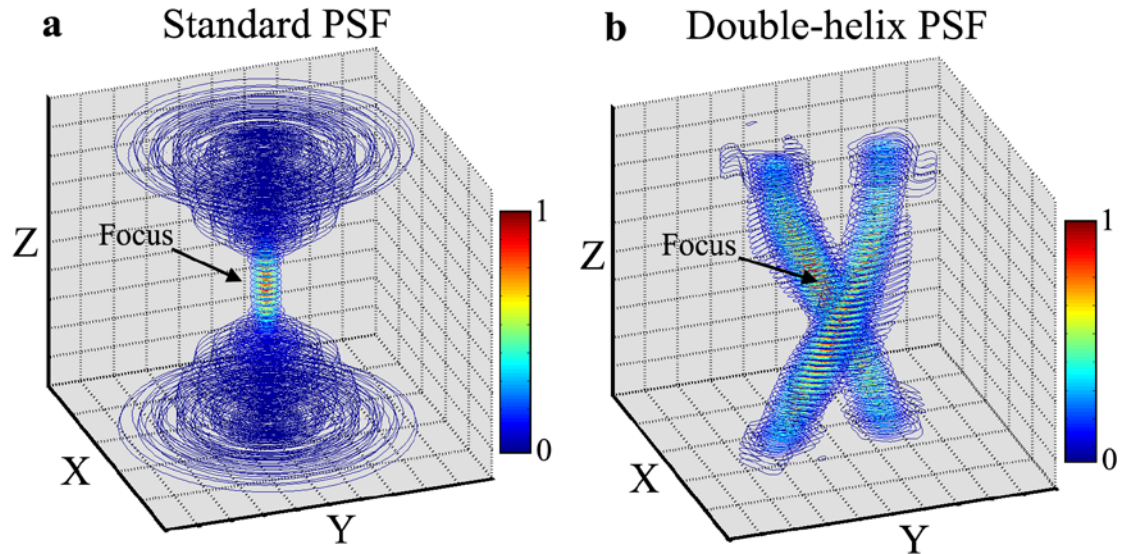
Figure 3.1. Comparison of standard and double-helix (DH) PSFs: (a) The shape of the standard PSF barely changes along the focal region, beyond which the PSF rapidly expands in size. (b) The DH-PSF exhibits two main lobes that continuously rotate along the axial (Z) dimension.

Another technique for 3D localization of recent renewed interest is digital holography [28,32,33,34]. Extensions of this technique improve the estimation accuracies with *a priori* knowledge about the particle scattering characteristics or digital post processing using the complex amplitude of the point spread function [28,32,33]. However, in general, digital holography suffers from coherent noise effects and multi-particle crosstalk, while requiring high space-bandwidth product detectors and significant digital post-processing.

Prior work has shown the use of diffracted rotation to encode depth information at the macro scale [22]. One of the drawbacks of that technique is the extremely low energy efficiency of the PSF generation [35], which precludes its use with small objects that scatter or emit weakly. Recent advances in PSF engineering have increased the transfer function efficiency by more than one order of magnitude [35], enabling for the first time the use of diffraction encoding to sense the nanoscale.

In this chapter, we present a 3D localization paradigm based on a double-helix (DH) PSF system operating in the *detector-limited* regime. This is in contrast to the *photon-limited* regime which will be discussed in chapters 4, 5, and 6. Fig. 3.2 compares the intensities of the standard and the double-helix PSFs in a detector-limited regime, and in a photon-limited regime.
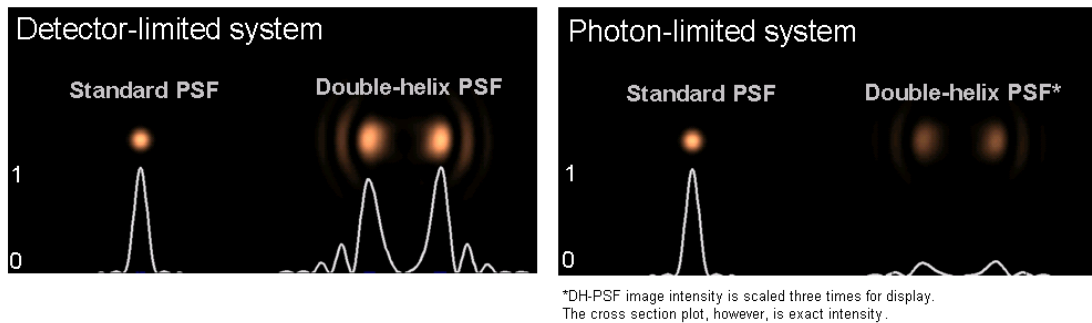
Fig. 3.2. Comparison of standard and double-helix PSFs in detector-limited and photon-limited systems. While both PSFs span the dynamic range of detector in detector-limited systems, the double-helix PSF peak intensity is lower than the standard PSF in photon-limited systems.

Detector-limited systems are pervasive and encompass a class of imaging systems where the object under observation either transmits, scatters, or reflects an external illumination. Imaging modalities such as bright-field, Zernike phase contrast, differential interference contrast, and dark-field fall into this regime. In these systems, the number of detected photons can be directly increased by increasing the intensity of the external illumination, and is only limited by the dynamic range of the detector for a particular detector setting (e.g. gain, exposure time). We show with an information-theoretical analysis that DH-PSF systems exhibit fundamentally better 3D position localization accuracies than conventional systems throughout a 3D volume of interest in the detector-limited regime. We then use a detector-limited bright-field DH-PSF microscope to demonstrate single-image 3D position localization of multiple scattering particles with nanometer scale accuracies.

3.2   3D position localization in a double-helix PSF system

The DH-PSF has two main lobes that rotate continuously with defocus creating a double-helical shape in a limited 3D region. As shown in Fig. 3.3, the two lobes are oriented horizontally when an object point is in-focus, and rotate in opposite directions when the point is moved along opposite defocus directions. Fig. 3.1 shows
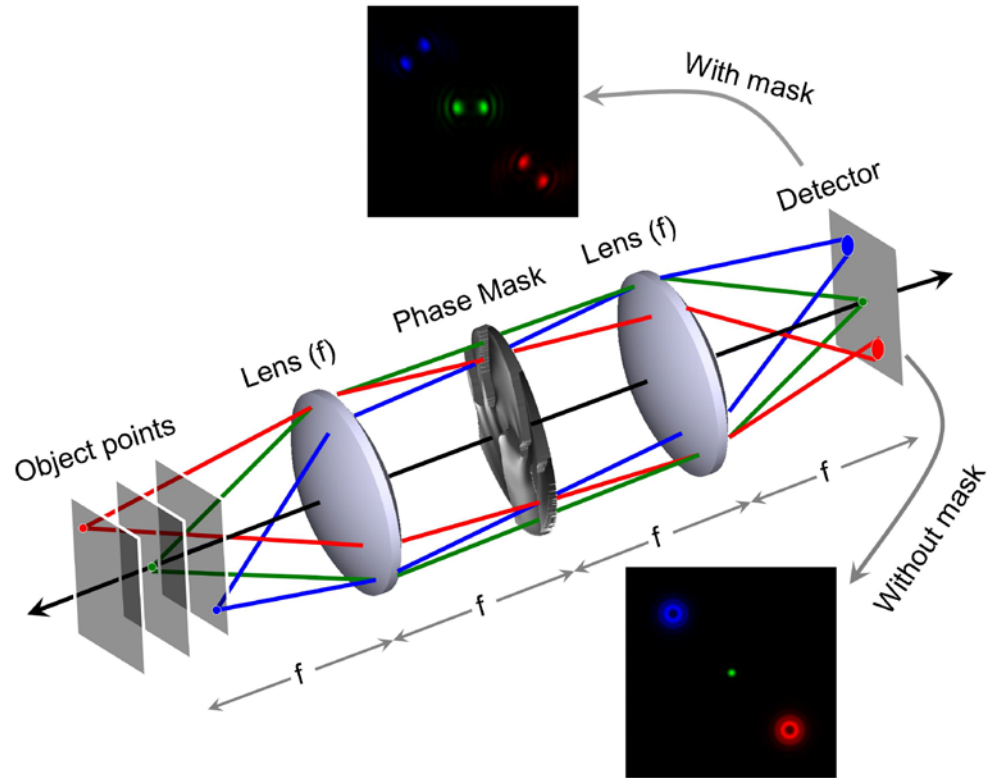
Figure 3.3. Imaging system engineered for 3D position localization. The PSF of an imaging system is engineered to exhibit two main lobes that continuously rotate along the optical axis. The PSF is implemented with a phase mask placed in the Fourier transform plane. For a particle in focus, the two lobes are oriented horizontally. When a particle is located in front of the focal plane, its PSF lobes are rotated in the counter-clockwise direction. On the other hand, when a particle is located behind the focal plane, its PSF lobes are rotated in the clockwise direction. In contrast, a standard imaging system (without the phase mask) would only blur particles outside the focal region.

how the DH-PSF lobes rotate 180 degrees within the axial region of interest. Beyond this region, the lobes essentially vanish due to diffraction, which is a desirable property for particle localization to avoid the background influence of out-of-range particles.

A practical low-complexity 3D position estimator determines the axial position of a particle from the angular orientation of its DH-PSF lobes and the transverse position

of the particle as the midpoint of the same two lobes. This estimator is analyzed in Sec. 3.3 and used in the experiments of Sec. 3.4.

3.3   Information-theoretical analysis: detector-limited systems

A useful measure for quantifying a PSF's ability to estimate position — under the inevitable presence of noise — is the Cramer-Rao Bound (CRB) [22,36,37,38]. The CRB is the lower bound on the variance over all unbiased estimators.   The CRB does not specify any particular method for estimating position, but is rather a fundamental limit associated with a PSF.

The CRB of a sampled 3D PSF along a particular spatial dimension is determined directly from the inverse of the Fisher Information matrix ($\mathbf{I}$) as,

$$CRB_{\theta[m]} = \boldsymbol{I}_{\theta}^{-1}[m,m] \ , \tag{3.1}$$

where $\boldsymbol{\theta} = [x, y, z]$, and m is either 1, 2, or 3. Because the number of parameters to be estimated is 3, $\boldsymbol{I}$ is a 3 x 3 matrix.

Each element of $\boldsymbol{I}$ is computed as,

$$\boldsymbol{I}_{\theta}[m,n] = \sum_{i,j} E\left[\frac{\partial \ln p_{i,j}(k/\theta)}{\partial \theta[m]} \frac{\partial \ln p_{i,j}(k/\theta)}{\partial \theta[n]}\right], \tag{3.2}$$

where $p_{i,j}(k/\boldsymbol{\theta})$ is the probability density function (PDF) for the pixel in i^{th} row and j^{th} column, E refers to expectation, and indices m, n are 1, 2, or 3. The sum in Eq. (3.2) corresponds to the addition of Fisher information over the pixels of the detector. Different noise sources can be considered by appropriately choosing the probability density function. For example, Gaussian PDFs can be used for thermal noise limited systems while Poisson PDFs can be used for systems that are shot noise limited.

Imaging systems generally exhibit shift invariance in the transverse dimension, but not in the axial dimension. Because of this property, the CRB of an imaging system remains constant in the transverse dimension but varies in the axial dimension. Consequently, for a given noise distribution, the CRB of a PSF for all object points in a 3D volume can be completely described by three 1D plots — $CRB_X(z)$, $CRB_Y(z)$, and $CRB_Z(z)$.

3.2.1 Comparison of Cramer-Rao Bounds

In general, the CRB decreases with an increase in the number of photons, until the peak intensity of the PSF saturates the detector. Increasing the number of photons beyond saturation will clip the detected PSF, thereby reducing the magnitude of the PSF's gradient. Therefore, the best (lowest) CRB of a PSF is obtained when the intensity of the PSF spans the dynamic range of the detector. Because the DH-PSF is broader (hence lower peak intensity) than the standard (clear aperture) PSF, it does not span the detector's dynamic range when the detector is set to span the standard PSF's dynamic range. In detector-limited systems, however, the illumination intensity can be increased to make the DH-PSF span the detector's dynamic range. This

flexibility in the detector-limited regime enables the quantification of the best position localization accuracies achievable with any PSF.

Fig. 3.4 shows numerical calculations of the CRB for the DH-PSF and the standard PSF in all three dimensions under Gaussian [Fig. 3.4(a-c)] and Poisson [Fig. 3.4(d-f)] noise. The calculations correspond to an SNR of 30. SNR is defined as the ratio of the peak value of the in-focus PSF to the standard deviation of noise.

Along the axial dimension [Fig. 3.4(a,d)], the standard PSF CRB_Z is sharply varying, becoming infinity exactly at the focal plane, thereby making differential position estimation virtually impossible in the focal region. In contrast, the DH-PSF CRB is essentially constant over a wide range and is significantly lower than the CRB of the standard PSF. Having a constant and low CRB means that position localization with high accuracy is possible over a long range.

In the transverse dimension, the standard PSF CRB_X and CRB_Y attain their minima at in-focus [Fig. 3.4(b,c,e,f)], and increase sharply as the PSF is defocused. However, the in-focus CRB_Z of the standard PSF is infinity. This means that the standard PSF is better in-focus for transverse position estimation, but better out-of-focus for axial position estimation. In contrast, the DH-PSF behavior is remarkably different, with CRB_X and CRB_Y significantly lower and more uniform than in the standard PSF case for any axial location. Hence, the DH-PSF can achieve high accuracy estimation *simultaneously* in all three dimensions.
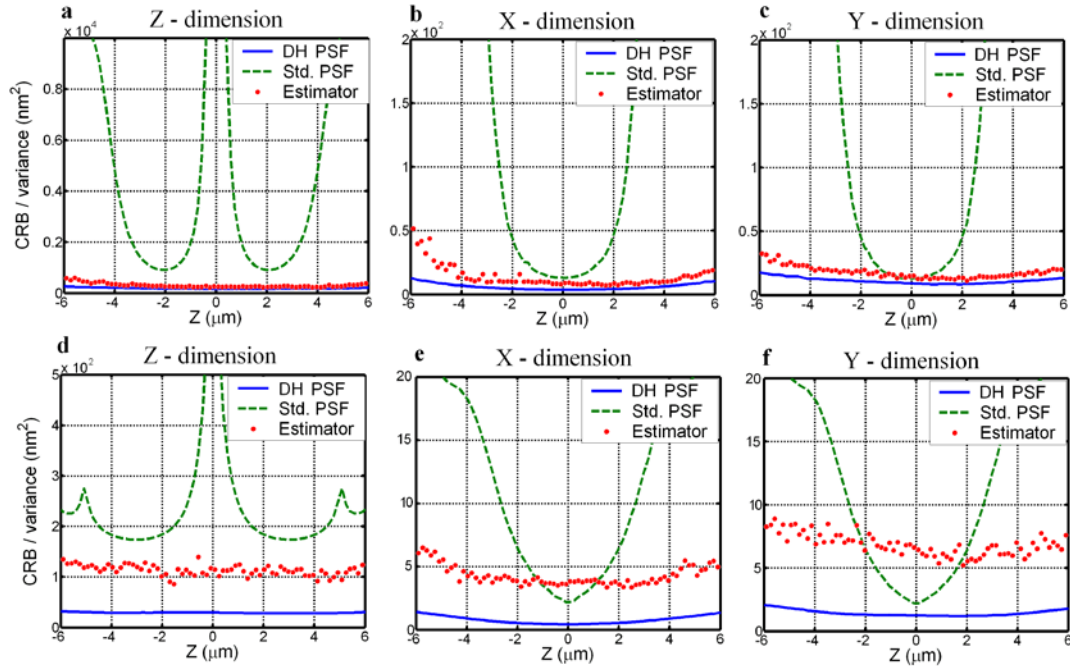
Figure 3.4. Information-theoretical comparison of DH and standard PSF for Gaussian and Poisson noise. The plots represent a comparison of DH and standard PSF CRBs, together with the implemented estimator variances in all three spatial dimensions for Gaussian (a-c) and Poisson (d-f) noise distributions. The system has 0.45 numerical aperture, 40X magnification, 6.3µm pixel width, and 633nm wavelength. (a,d), (b,e), and (c,f) show the CRBs and variances for Z, X, and Y dimensions, respectively, as a function of Z for an SNR of 30. The CRB of the DH-PSF is lower and more uniform than the CRB of the standard PSF in all three spatial dimensions.

The uniformly low CRBs of the DH-PSF are explained by the fact that the energy of the DH-PSF is concentrated in the two lobes that rotate uniformly throughout the Z region of interest. This behavior, in turn, creates effectively constant derivatives in the CRB calculations of Eq. 3.2. It is also worth noting that CRB_X and CRB_Y of the DH-PSF are not identical because of the transverse asymmetry of the PSF.

The CRB analysis was performed for 0.45NA to show an important property of DH-PSF, namely that nanometer scale position localization accuracies are achievable even with relatively low NA objectives. In effect, for the parameters of Fig. 3.4, the

in-focus standard deviations are 1.9nm (X), 3nm (Y), and 12.8nm (Z) for Gaussian noise, and 0.7nm (X), 1.1nm (Y), and 5.4nm (Z) for Poisson noise. All other parameters being the same, increasing the NA lowers the estimator variance in all three dimensions while always keeping the DH-PSF CRB below the standard PSF CRB.

3.2.2 Performance of the practical centroid estimator

The maximum-likelihood estimator can reach the CRB [37], but its computational complexity might preclude its use in applications requiring real-time position localization. The practical estimator implemented here uses the centroids of the two DH-PSF lobes. While the transverse position is the midpoint of the two lobe centroids, the axial position is estimated from the rotation angle of the two centroids using a look up table that maps angles to axial positions. The main advantage of this estimator is that it is non-iterative, and hence fast to compute. However, because it uses only a partial set of geometrical characteristics instead of the entire PSF shape, in general it does not reach the CRB limit.

Fig. 3.4 also shows the variance of the implemented estimator. This variance was determined using a Monte Carlo simulation from a dataset of 500 estimations under additive Gaussian or Poisson noise with an SNR of 30. For Gaussian noise, the practical estimator variance almost reaches the DH-PSF CRB, and is lower than the standard PSF's CRB_Z and CRB_X for all object points in the 3D volume [Fig. 3.4(a,b)]. In the Y dimension, the variance of the practical DH-PSF estimator is almost equal to the standard PSF CRB_Y near the in-focus region, and is lower for all other axial

positions [Fig. 3.4(c)]. For the Poisson noise case, the variance of the practical DH-PSF estimator is lower than the standard PSF CRB_Z for all object points in the 3D volume [Fig. 3.4(d)]. In the X and Y dimensions, the variance is higher than the standard PSF CRB_X and CRB_Y near the in-focus region, but significantly lower for all other axial positions over a long range [Fig. 3.4(e,f)].

CRBs and estimator variances decrease with increase in SNR. The inferences made from Fig. 3.4 regarding the relative performances of the DH and the standard PSFs are valid for a wide range of SNRs (See section 3.9 – Fig. 3.10).

3.4   Bright-field double-helix microscope for 3D particle localization

3D localization of multiple particles can be achieved with a single image using a DH-PSF system. When a DH phase mask is placed in the Fourier plane of an imaging system (Fig. 3.3) [35], every object point is convolved with the two DH-PSF lobes at different angular orientations depending on the point's axial position. For an imaging system with magnification M, the DH-PSF corresponding to an object point at *(x, y, z)* is located at *(Mx, My),* and oriented at an angle, which is uniquely related to z.

In a detector-limited bright-field microscope (Fig. 3.5), designed for 3D localization of multiple particles with a single DH-PSF image, an object is mounted on a piezo stage and illuminated with the 514.5nm Argon laser line. The object consists of five index scatterers (about 1μm wide and 2.5μm long) inside the volume of a glass slide. These were fabricated by focusing a femtosecond laser pulse at different 3D spatial locations to produce tiny refractive index discontinuities in the

glass. A $\lambda/2$ wave plate and a polarizer are used to create horizontally polarized illumination appropriate for the spatial light modulator (SLM) used in the imaging path. Spatial incoherent illumination is achieved by using a rotating diffuser plate in the illuminating laser path. The light scattered by the diffuser is focused on the sample by a combination of two lenses designed to maximize the collection efficiency and to avoid a significant increase in the spatial coherence of the illumination.

The subsequent imaging path of the system consists of a microscope section and a signal processing section. In the microscope section, a 1.3NA infinity corrected oil-immersion objective and a 125mm focal length tube lens magnify the point scatterers 76 times. This magnified image of the point scatterers acts as the virtual object for the subsequent signal processing section of the imaging path. The signal processing section consists of a reflective phase-only SLM, a 50/50 beam splitter, and two 100mm focal length lenses. These two lenses are arranged in a reflective 4f configuration. Finally, an electron multiplying charge coupled device (EMCCD) detector array cooled to -90°C and placed 100mm away from the second lens detects the output of the signal processing section. The Argon laser power was set such that the DH-PSF images of the point scatterers span the dynamic range of the CCD, which
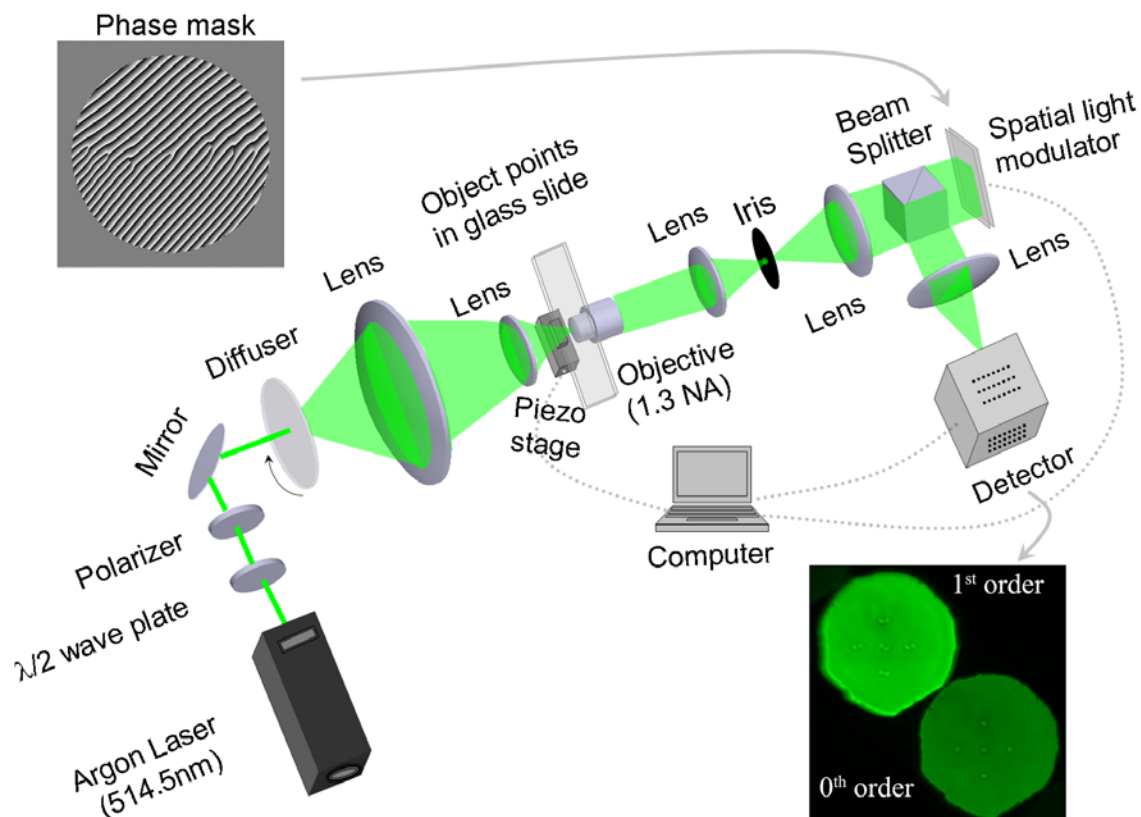
Figure 3.5. Experimental setup for 3D localization with a DH-PSF system. A glass slide containing a 3D distribution of point scatterers is illuminated with a horizontally polarized Argon laser source (514.5nm wavelength), which is made spatially incoherent by a rotating diffuser. The imaging path consists of a microscope section and a signal processing section containing a spatial light modulator to encode the DH-PSF phase mask (upper-left inset) in the Fourier plane. The detected image consists of a diffracted (1st) order containing the DH-PSF image, and an undiffracted (0th) order containing the standard PSF image (bottom-right inset). This system can estimate the 3D locations of multiple sparse particles using a single image.

was set to operate with no gain in order to avoid amplifying noise. The SNR of the system is 162. These source and detector settings take advantage of the detector-limited nature of the bright-field DH-PSF microscope.

When the SLM displays the DH-PSF phase mask, assuming the scatterers are smaller than the coherence area (area over which the illumination beam is spatially coherent), the Fourier transform of the complex amplitude of the scatterers is multiplied by the transfer function of the DH-PSF. In the space domain, the complex amplitude of each scatterer is mathematically convolved with a differently oriented 2D PSF, according to the scatterer's axial position.

A linear phase is added to the DH-PSF phase mask function and phase wrapped to avoid the distortion of undiffracted light from the SLM. This mask produces a diffracted (1st) order containing the DH-PSF image, and an undiffracted (0th) order containing the standard PSF image (See bottom-right inset in Fig. 3.5).

The 0th order is 69% as bright as the 1st order, but it could be eliminated for example by using a custom diffractive optical element. In this system, however, the 0th order is useful for comparison.

The result of imaging the scatterers with the DH-PSF system is shown in Fig. 3.6 and in Fig. 3.11. The standard PSF image [Fig. 3.6(a)] blurs the particles outside the focal region. However, the DH-PSF image [Fig. 3.6(b)] shows characteristic two-lobe images with different angular orientations. The DH-PSF image encodes the axial location of the particles in the rotation angle of the PSF lobes. The axial position of each particle is estimated by mapping the rotation angles to axial distances using calibration data (see Section 3.8). The transverse location is estimated as the midpoint between the centroids of the two lobes. The 3D localization result is shown in Fig. 3.6(c). One hundred successive images of the glass slide, each recorded with a 236ms exposure time, were analyzed in order to characterize the standard deviation of the

estimation. The mean and standard deviation of the positions are listed in Table 3.1.

Less than 10nm single-image standard deviations are achieved in all three dimensions

for all of the five particles.
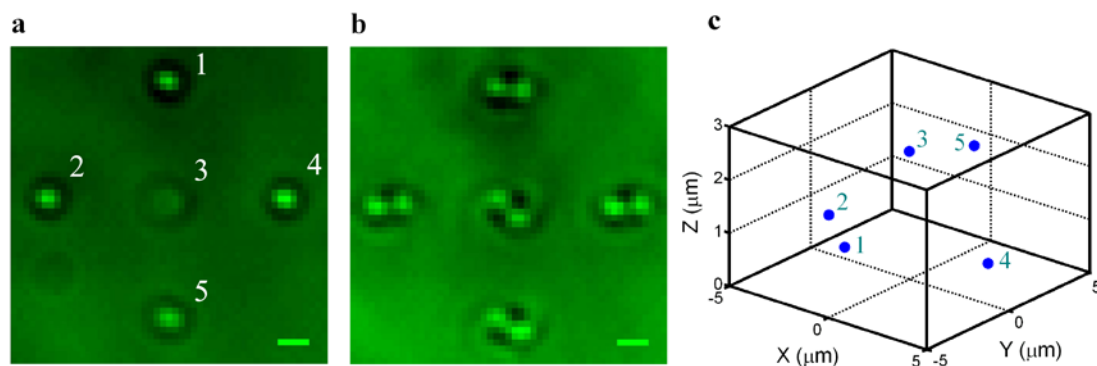
Figure 3.6: 3D localization results. (a) Standard PSF and (b) DH-PSF images of five scatterers located at different transverse and axial positions inside the volume of a glass slide. The scale bar in the bottom right of the images represents 1μm. While the standard PSF image blurs the particles outside the focal plane, the DH-PSF image encodes the axial location of the particles in the rotation angle of the PSF lobes. (c) 3D position estimation result from the DH-PSF image in (b). [See related movie from Appl. Phys. Lett. **95**, 021103 (2009)]

Table 3.1: Mean 3D positions and 3D standard deviations for the 5 particles in Fig. 3.5

Particle	$\bar{X}$ (μm)	$\bar{Y}$ (μm)	$\bar{Z}$ (μm)	X accuracy (nm)				Y accuracy (nm)				Z accuracy (nm)			
				σ_{Xm}	$\sigma_{\overline{Xcr}}$	σ_X	$\sigma_{\bar{X}}$	σ_{Ym}	$\sigma_{\overline{Ycr}}$	σ_Y	$\sigma_{\bar{Y}}$	σ_{Za}	$\sigma_{\overline{Zcl}}$	σ_Z	$\sigma_{\bar{Z}}$
1	-0.0333	-4.0497	1.1801	6.1	1.2	**6.2**	**1.4**	3.7	0.7	**3.8**	**0.8**	8.8	1.8	**9.0**	**2.0**
2	-4.093	-0.1136	0.7507	6.5	1.3	**6.6**	**1.4**	3.2	0.9	**3.3**	**0.9**	5.9	2.0	**6.2**	**2.1**
3	0	0	2.4007	5.8	1.4	**6.0**	**1.5**	3.6	0.6	**3.6**	**0.7**	8.7	2.6	**9.1**	**2.7**
4	3.9309	-0.0704	0.7884	5.5	1.3	**5.7**	**1.4**	3.7	0.9	**3.9**	**1.0**	8.2	2.0	**8.5**	**2.2**
5	0.0265	3.9242	1.9553	5.9	1.3	**6.0**	**1.4**	3.6	0.6	**3.7**	**0.7**	7.7	2.3	**8.0**	**2.4**

$\bar{X}$, $\bar{Y}$, $\bar{Z}$: Cartesian coordinates of the 3D position of a particle

σ_X, σ_Y, σ_Z : Single-image standard deviations along the X, Y, and Z dimensions

$\sigma_{\bar{X}}$, $\sigma_{\bar{Y}}$, $\sigma_{\bar{Z}}$: 3D Standard deviations of the mean, when all 100 detected images are averaged

σ_{Xm}, σ_{Ym}, σ_{Za} : Single-image standard deviations for lobe midpoint (Xm, Ym) and angle (Za) estimations.

$\sigma_{\overline{Xcr}}$, $\sigma_{\overline{Ycr}}$, $\sigma_{\overline{Zcl}}$: Standard deviations of X correction, Y correction, and Z calibration associated with the mean of 20 estimates.

$\sigma_X = (\sigma_{Xm}^2 + \sigma_{\overline{Xcr}}^2)^{1/2}$, $\sigma_Y = (\sigma_{Ym}^2 + \sigma_{\overline{Ycr}}^2)^{1/2}$, and $\sigma_Z = (\sigma_{Za}^2 + \sigma_{\overline{Zcl}}^2)^{1/2}$

$\sigma_{\bar{X}} = (\sigma_{\overline{Xm}}^2 + \sigma_{\overline{Xcr}}^2)^{1/2}$, $\sigma_{\bar{Y}} = (\sigma_{\overline{Ym}}^2 + \sigma_{\overline{Ycr}}^2)^{1/2}$, and $\sigma_{\bar{Z}} = (\sigma_{\overline{Za}}^2 + \sigma_{\overline{Zcl}}^2)^{1/2}$.

3.5 Dark-field double-helix PSF microscopy

Because bright-field imaging produces a background in the detected images, weakly scattering samples appear with poor contrast. For such samples, dark-field mode is a suitable choice to achieve high-contrast imaging (Fig. 3.7). Here, the low spatial frequency components of the sample that are responsible for the image background are blocked from participating in the image formation.
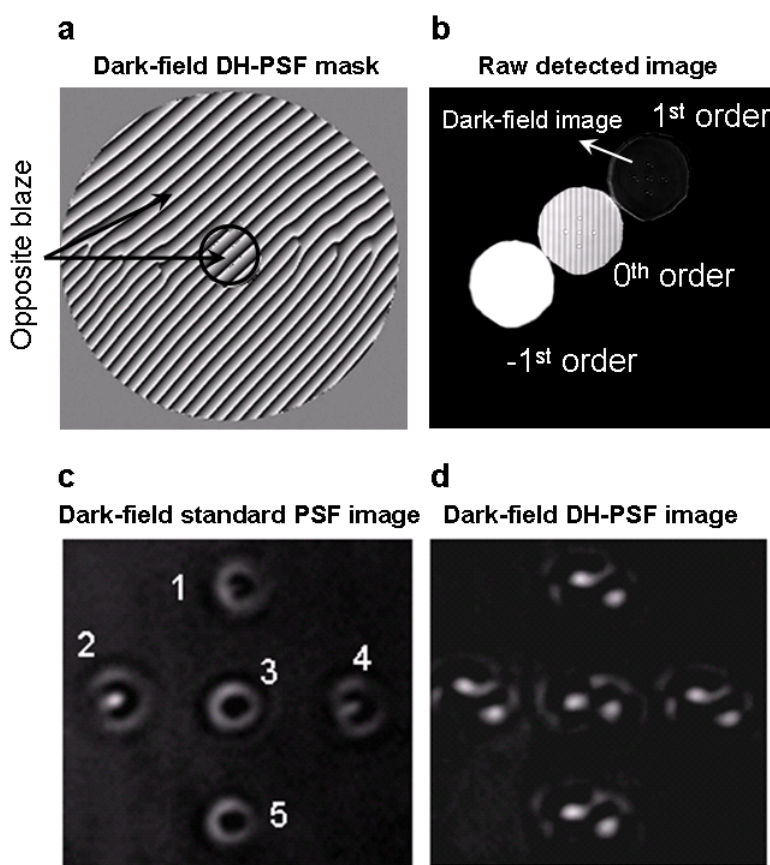
Figure 3.7. Dark-field DH-PSF microscopy. (a) Dark-field DH-PSF mask generating the dark-field DH-PSF image shown in (d) in the $+1^{st}$ diffraction order by directing the lower spatial frequency components to the -1st order as shown in (b). (c) Dark-field standard PSF image shown here for comparison with the dark-field DH-PSF image.

Traditionally, a microscope is operated in the dark-field mode by inserting an opaque annular stop to produce a hollow cone illumination, and by making sure that only the higher order frequencies reach the image plane. However, the dark-field DH-PSF image in Fig. 3.7(d) was obtained by using a modified blazed DH-PSF phase mask that blocks the lower frequency components from reaching the image plane [39]. Specifically, a circular central region of the blazed DH-PSF mask is replaced with a grating having an opposite blaze orientation as shown in Fig. 3.7(a). By re-directing the energy in the low frequency components to the -1st order, this mask forms the dark-field DH-PSF image in its +1st order Fig. 3.7(b). The -1st order was chosen (as opposed to the 0th order) to prevent the 0th order from saturating the detector and possibly leaking into the +1st order containing the dark-field image. For comparison, Fig. 3.7(c) shows a dark-field standard PSF image obtained using a blazed grating (instead of the blazed DH-PSF mask) with an opposite blaze in a central circular region. In contrast to the dark-field standard PSF image of Fig. 3.7 (c), the two DH-PSF lobes in the dark-field DH-PSF image of Fig. 3.7(d) encode the 3D position of the five particles.

3.6 Sensitivity of double-helix PSF microscopes

Returning to Fig. 3.6, the better sensitivity of the DH-PSF to small variations in depth is apparent. In the standard PSF image of Fig. 3.6a, particles 1, 2, and 4 appear similar because they are within the depth of field of the system. However, in the DH-PSF image of Fig. 3.6b, the different rotation angles of the PSF clearly indicate that

the particles are at different axial locations. This fact directly translates into axial position estimation with better accuracy.

The accuracies in Table 3.1 are in-line with what is expected from the practical centroid estimator, considering that the particles are not ideal point sources (see section 3.9.2), and the fact that the system suffers from vibrations. In the experiment, position uncertainties could be reduced by mechanically isolating the rotating diffuser and the laser cooling system from the optical setup.

If the object is fixed and if acquisition time is not an issue, the average of the estimates over several (N) images could be calculated providing an improvement in accuracy by a factor of $\frac{1}{\sqrt{N}}$. In this experiment, for example, if the 100 estimates were averaged, the accuracies shown in the table would improve by a factor of 10, providing sub-nanometer scale localizations. In general, when reaching the sub-nanometer scale, care is required to consider sources of systematic error such as detector array non-uniformity, which can be corrected by proper calibration.

Notwithstanding, it is remarkable that the standard deviations listed in Table 3.1 do not represent the fundamental limit of a single-image DH-PSF system. CRB computations for a similar DH system — 1.3NA, 100x magnification, 514.5nm wavelength, 4.4μm pixel width, and an SNR of 30 under Poisson noise distribution for an in-focus particle — determined the fundamental accuracy limits as 0.2nm, 0.3nm, and 0.2nm in X, Y, and Z dimensions, respectively. From information theory, we know that these accuracies could potentially be achieved by using more complex estimators, which present an exciting challenge for the future.

3.7   Summary

In summary, an information-theoretical analysis shows that the DH-PSF is fundamentally better suited for detector-limited 3D position estimation than the standard PSF because it has a lower CRB (better localization accuracy) along the three spatial dimensions, over a long axial range. The variance of a fast position estimator is found to be lower than the CRB of the standard PSF in all three dimensions. A detector-limited experiment with a bright-field DH-PSF microscope demonstrates nanometer scale 3D localization of multiple particles using a single image. These results show the exciting potential to reach deep into the subnanometer regime using detector-limited DH-PSF systems.

3.8   Appendix I: Methods for PSF calculation and system calibration

3.8.1 PSF calculation

The PSFs are calculated numerically from their transfer functions using a paraxial scalar model. The paraxial PSF model is a good approximation even for high NA objectives as shown by prior studies [40]. This model is also valid in the signal processing part of the system in Fig. 3.5 where, after propagation through the objective lens, the waves are essentially paraxial.

The incoherent PSF [$h(x,y,z)$] at different axial planes is computed by multiplying the DH-PSF transfer function by a quadratic phase factor, calculating the inverse Fourier transform, and then its modulo-squared value as follows:

$$h(x,y,z) = \left| \Im^{-1} \left\{ H(u,v) exp\left[-i \frac{\Psi(z)}{2}(u^2 + v^2) \right] \right\} \right|^2, \qquad (3.3)$$

where *(x,y,z)* and *(u,v)* are Cartesian coordinates in the spatial and the Fourier domains, *H* is the transfer function, $\Im$ represents the two-dimensional Fourier transform operator, and Ψ is the defocus parameter, defined as

$$\Psi(z) = \frac{2\pi}{\lambda}\left(\frac{1}{z_f} - \frac{1}{z} \right) r^2, \qquad (3.4)$$

where z_f is the distance of the in-focus plane to the entrance pupil, *r* is the aperture radius, and λ is the wavelength. From equation (3.4), it can be seen that the defocus parameter is primarily dependent on the system's NA ($NA = sin[tan^{-1}(r/z_f)]$) and λ.

The in-focus DH-PSF lobes are about 1.7 times larger and are separated by about 3 times the size of a corresponding in-focus standard PSF lobe. While the DH-PSF expands by roughly 1.2 times through its range of operation, the standard PSF expands by about 9.6 times through this range.

3.6.2 Calibration

The DH-PSF system is calibrated to map rotation angles to axial positions. DH-PSF images of one of the particles at different axial distances are recorded in steps of 200nm through a range of 3μm. Fig. 3.8 shows a few of these images (a-d) and their corresponding standard PSF images (e-h). Rotation angles at each of the axial steps are determined as the angle between the centroids of the two DH-PSF lobes. Twenty successive measurements were made at each axial step to determine the standard

deviation of the calibration. The resulting calibration plot, with error bars denoting standard deviation, is shown in Fig. 3.8(i). The rotation rate of this DH-PSF system is 1 degree for every 34.7nm. Because the rotation angle estimator can resolve small fractions of a degree, very small axial distances can be resolved by this system. In general, given a DH-PSF mask, the rate of rotation of the PSF is directly related to the NA of the system and the wavelength of operation. However, other rotating PSF masks with different PSF shapes and rotation rates can be designed [15].
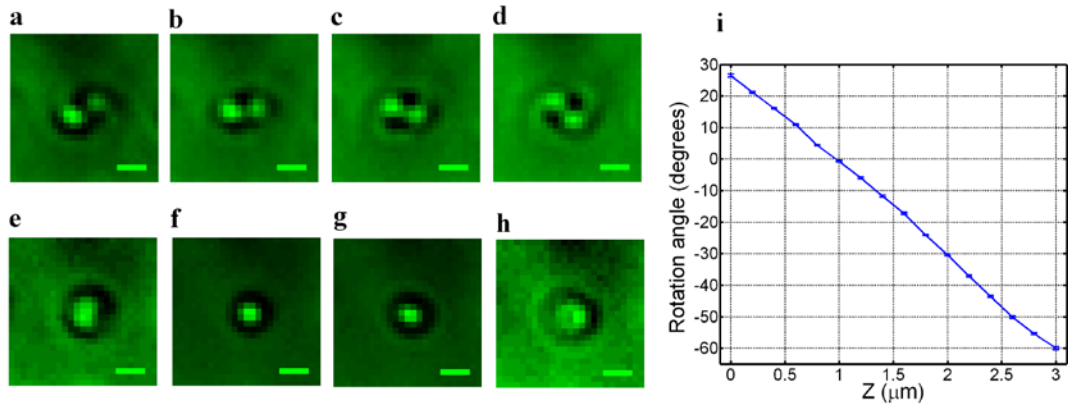
Figure 3.8: DH and standard PSF images of a particle at depths (a, e) 0μm, (b,f) 0.8μm, (c,g) 1.6μm, and (d,h) 2.4μm. These images were obtained by moving the particle in the axial dimension with a piezo-stage. The scale bars in the bottom right of the images represent 1μm. (i) Calibration plot of rotation angle vs axial distance through a 3 μm range. The standard deviation of 20 rotation angle estimations is plotted as an error bar at each axial step.

The calibration DH-PSF images are also used to determine the X and Y correction factors (Fig. 3.9). These factors correct for the small transverse displacement of the DH-PSF as a function axial distance. The exact transverse position of a particle is obtained by subtracting these factors from the midpoint of the particle's DH-PSF lobes. These correction factors are found to be space invariant.
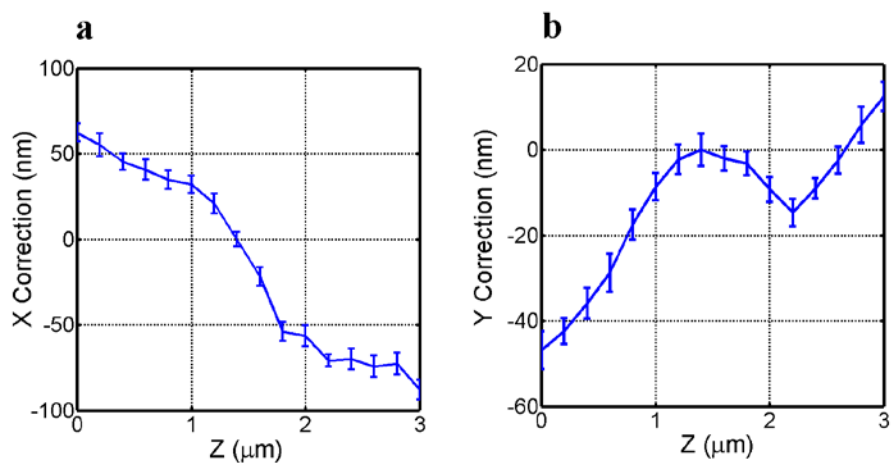
Figure 3.9: The midpoint of the centroids of two lobes exhibits aberration-induced position variations along the (a) X and (b) Y dimensions as a function of the axial distance. The transverse position of a particle is estimated by correcting these transverse position variations from the midpoint of its DH-PSF lobes.

3.9   Appendix II: SNR, information theory calculations, and estimation

The effect of SNR on the CRB and the estimator variances is analyzed in Figure 3.10.

See figure caption for more explanation.
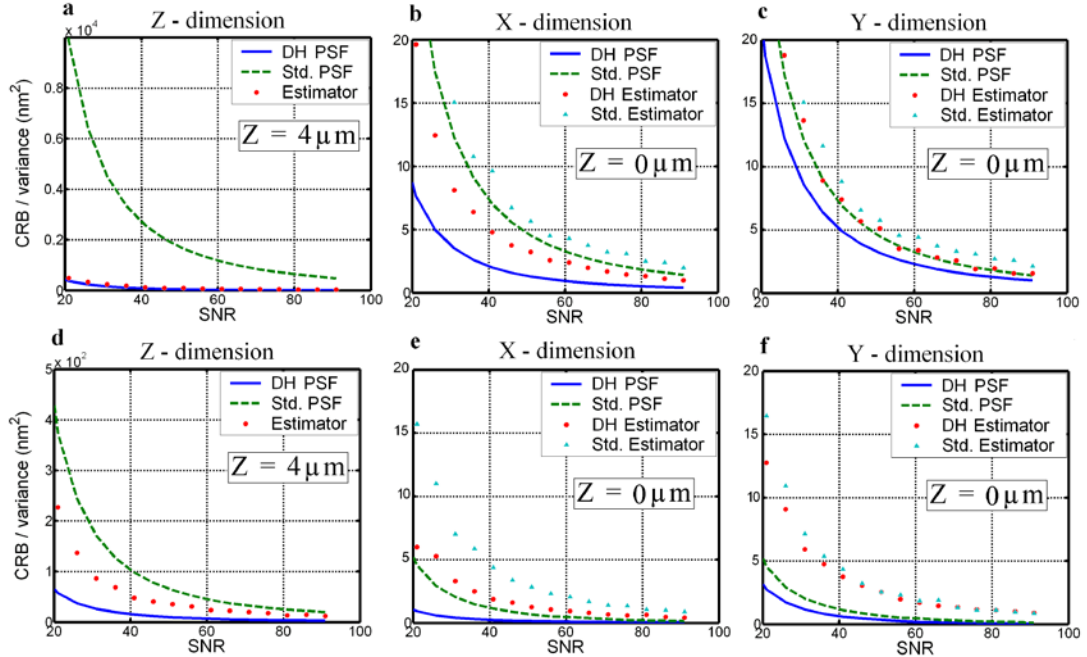
Figure 3.10:   Effect of SNR: This figure compares the CRBs of DH and standard PSFs, together with the practical estimator variances at different SNRs under Gaussian (a-c) and Poisson (d-f) noise distributions. The system parameters are the same as in Fig. 3.4. The CRBs and variances are calculated for specific Z locations: $Z = 4\mu m$ (Z-dimension), $Z = 0\mu m$ (X and Y dimensions). CRBs and estimator variances decrease with increase in SNR. The CRB of the DH-PSF is lower than that of the standard PSF for a wide range of SNRs in all three dimensions. For Gaussian noise, the practical DH-PSF estimator variance is lower than the standard PSF CRB for all SNRs in the (a) Z and (b) X dimensions, and approximately overlaps with the standard PSF CRB in the (c) Y dimension. For the Poisson noise case, the practical DH-PSF estimator variance is lower than the standard PSF CRB in the (d) Z dimension, and is higher than the standard PSF CRB in the (e) X and (f) Y dimensions. The estimator variance of an equivalent (centroid based) standard PSF estimator is found to be higher than the practical DH-PSF estimator variance in the X and Y dimensions for both (b,c) Gaussian and (e,f) Poisson noise.

Figure 3.11 compares the effect of translating a glass slide containing five index scatterers with a standard PSF system and with a DH-PSF system.
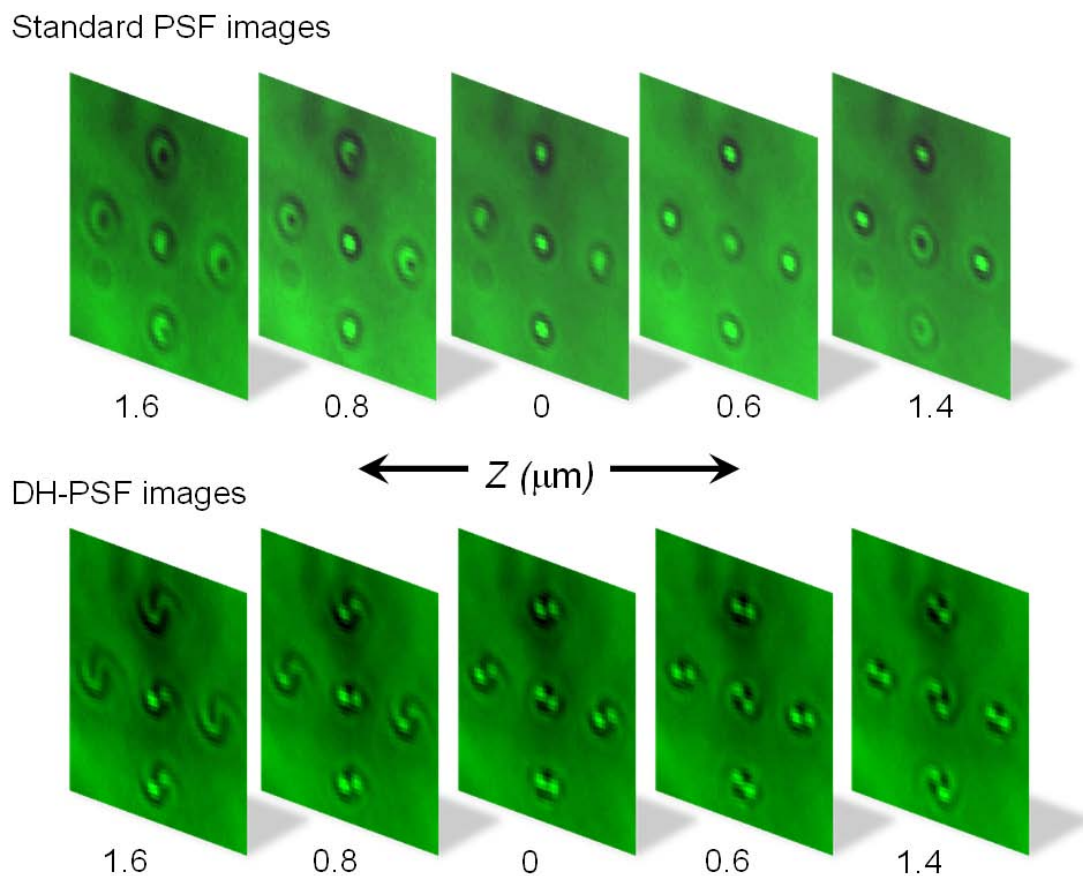
Figure 3.11: Comparison of the standard and DH PSF images of five scatterers that are located at different 3D locations. As the system is defocused (using a piezo-stage), the standard PSF image blurs the scatterers, while the DH-PSF image encodes the axial locations of the scatterers in the rotation angle of the DH-PSF lobes. [See movie from Appl. Phys. Lett. **95**, 021103 (2009)]

3.9.1 Information-theoretical calculations

The Cramer-Rao Bound (CRB) of a PSF (Figs. 3.4 and 3.10) is calculated numerically using equations (3.1) and (3.2). For any given value of Z, the CRB is calculated by first computing the Fisher Information matrix (**I**) using equation (3.2), and then by inverting **I** as shown in equation (3.1). Each element of **I** is computed from sampled PSF values and a specific noise model. The noise model defines the probability density function, $p_{i,j}(k/\,\boldsymbol{\theta})$. For example, in a thermal noise limited system, $p_{i,j}(k/\,\boldsymbol{\theta})$ is a Gaussian distribution. The mean of the distribution is the PSF pixel value at the ith row and jth column, and the standard deviation of the distribution is the ratio of the peak value of the PSF to the SNR. The expectation of the derivatives of the natural logarithm of $p_{i,j}(k/\,\boldsymbol{\theta})$ with respect to $\boldsymbol{\theta}[n]$ and $\boldsymbol{\theta}[m]$ are calculated as shown in equation (3.2). Finally, the expectations from all pixels of the PSF are added to obtain the element (m,n) of **I.**

Monte Carlo simulations are used to determine the variance of the centroid based DH-PSF estimator (Figs. 3.4 and 3.10). The PSF corresponding to each Z location is numerically computed from the DH-PSF transfer function, and either Gaussian or Poisson noise is added to it. The SNR is 30 in Fig. 3.4 and varies from 20 to 90 in Fig. 3.10. The transverse and axial positions are estimated from the centroids of the two (noise-corrupted) PSF lobes. 500 estimates of the 3D positions are obtained by repeating this process. The variance of the DH-PSF estimator is determined as the variance of these 500 estimates.

3.9.2 Effect of a large particle

When a particle being imaged in a DH-PSF system is larger than a point source, the detected image is, to a good approximation, the convolution of the object and the DH-PSF. As long as the particle size in any direction is smaller than *w,* where *w = distance between lobe centroids - lobe size,* the image of the particle will exhibit two non-overlapping lobes. Consequently, the centroid estimator can still be used. The effect of this increased particle size on the estimation accuracy along a particular dimension depends on the shape of the particle and the angular orientation of the DH-PSF lobes.

There are two competing factors that affect the CRB as the particle size increases. First, the magnitude of the gradient of the image decreases with increasing particle size due to the convolution, hence increasing the CRB. Second, the image of the particle spans a larger number of pixels, which in turn decreases the CRB. These factors affect the values of CRB_X, CRB_Y, CRB_Z, and actual measured variances, as exemplified in Table 1 where $\sigma_x > \sigma_y$, contrary to what it could be expected from the CRB values of Fig. 3.4. Because these factors affect both the DH-PSF and the standard PSF, CRB_X, CRB_Y, and CRB_Z are always lower for the DH-PSF than for the standard PSF.

3.9.3 Position estimation

The 3D position of a particle is estimated from the centroids of the particle's DH-PSF lobes. A square region with 17 pixel side that contains the image of a particle is extracted from the raw detected image. This region is interpolated to a 256 x 256

pixel region by using bicubic interpolation. The interpolated region is then normalized such that the pixel values range between 0 and 1. This normalized image is thresholded to eliminate background light below a certain small value. The threshold value is chosen such that the areas of the two lobes are maximized while still being disconnected. The centroids of the two PSF lobes are then determined. The transverse particle position is estimated from the midpoint of the two lobe centroids, while the rotation angle of the PSF is estimated as the angle of the line joining the two centroids. Finally, the axial position of the particle is obtained from the rotation angle using the calibration plot in Fig. 3.8i.

Chapter 4

3D Tracking in Photon-limited Double-helix Microscopes

We demonstrate simultaneous three-dimensional tracking of multiple fluorescent microparticles with the Double-helix PSF. An information theoretical comparison in photon-limited systems shows that the DH-PSF delivers higher Fisher information for 3D localization than the standard PSF. Experiments demonstrate average position estimation accuracies under 14nm and 37nm in the transverse and axial dimensions respectively. The system determines the 3D positions of multiple particles with a single image, and using a time series of images, tracks particle position and provides their velocities.

4.1 Introduction

Discrete fluorescent particles are often encountered in applications such as biological imaging [41,42], single molecule imaging [43,44], and flow cytometry [45]. In most cases, these fluorescent particles move in all three spatial dimensions with time. Accurately detecting these position variations is critical in many applications. Conventional fluorescent microscopes are good for detecting position variations of focused particles along the transverse dimensions [31]. However, because of the finite depth of field associated with the point spread functions (PSFs) of these microscopes, small axial position variations of focused particles escape undetected. Confocal microscopes offer better axial sensitivity, but the motion of the fluorescent particles

precludes the use of mechanical scanning to obtain three-dimensional (3D) position information. 3D tracking requires that the 3D positions of particles at a particular time be instantaneously determined, for example by recording a single image at a given time.

One way to increase axial position estimation sensitivity is to slightly defocus the system to operate just outside focus [27]. This increased axial sensitivity, however, comes at a price. Because of the lowering of signal levels, defocused systems have reduced transverse position sensitivity than focused systems. In photon-limited applications, defocusing buries the signal in noise, and is consequently not the best approach for 3D tracking. A weak cylindrical lens in a microscope's imaging path creates an astigmatic PSF, which is often used for 3D tracking [26,46,9]. Unfortunately, astigmatic PSFs expand in size with defocus, resulting in reduced signal levels. Another interesting way to achieve 3D imaging without scanning is by using digital holography [28,32]. Although originally developed for coherent systems, it has recently been extended to incoherent emitters like fluorescent particles [47]. However, this incoherent extension requires multiple images for determining the 3D particle locations, and is hence not suitable for 3D tracking.

In the last chapter, we demonstrated single-image 3D localization of discrete scattering particles in a *detector-limited* monochromatic wide-field microscope presenting a double-helix (DH) PSF [48]. An information theoretical analysis showed that the DH-PSF is fundamentally better suited than the standard diffraction-limited PSF for 3D position localization in detector-limited systems with either Gaussian or Poisson noise.

In this chapter, we report our studies on *photon-limited* DH-PSF systems. In order to compare the 3D position localization accuracies of systems with different PSFs, we introduce a new quality measure based on the average Fisher information over the 3D volume of interest. Using this measure, we show that in the photon-limited case, DH-PSF systems carry higher average Fisher information than the standard PSF systems. We then demonstrate simultaneous 3D position estimations of multiple fluorescent particles using a single image with accuracies in the nanometer regime. By acquiring multiple images at periodic intervals, we track moving fluorescent particles in three dimensions, and calculate their velocities.

4.2   Double-helix PSF for photon-limited systems

While analytical solutions for helical beams provide valuable insight on wave propagation and can be used in applications with unlimited photon budget [22], they do not provide the high-efficiency transfer functions required for photon-limited systems. Hence, we use a design that confines the helical pattern to a specific axial range of interest to attain high efficiency systems [Chapter 2, Ref. 35]. Unlike standard and astigmatic PSFs, the DH-PSF concentrates its energy in its two main lobes throughout this range of operation, and is consequently well suited for photon-limited applications. Note that DH-PSF displays a significant change of orientation with defocus over an extended depth [Fig. 4.1(a)]. In contrast, the standard PSF presents a slowly changing and expanding symmetrical pattern in the same region [Fig. 4.1(b)].
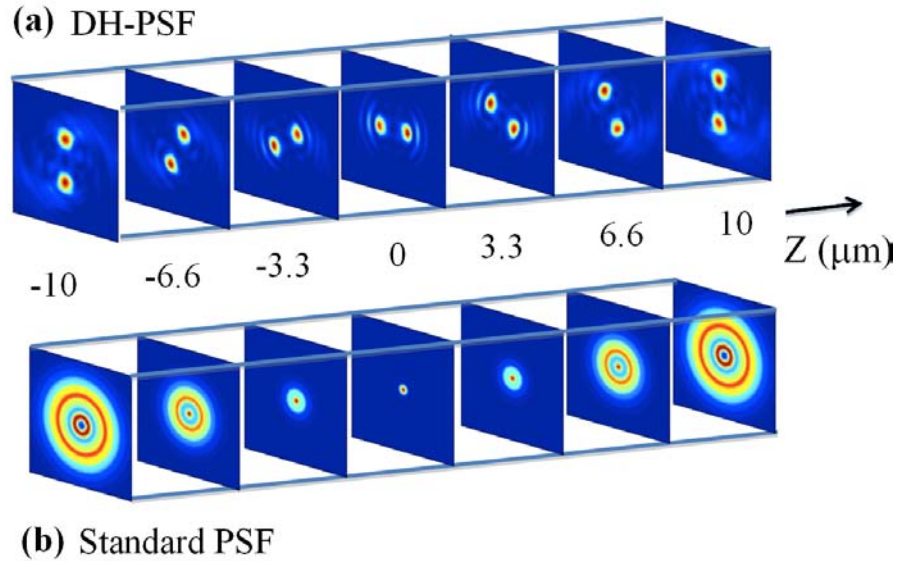
Fig. 4.1. Comparison of the (a) DH-PSF and the (b) standard PSF at different axial planes for a system with 0.45 numerical aperture (NA) and 633nm wavelength.

4.3 Information theoretical analysis: photon-limited systems

The position estimation accuracy of a PSF in the presence of noise can be quantified by computing its Cramer-Rao bound (CRB) [Chapter 3]. The CRB of a PSF represents the lowest possible position estimation variance that can be achieved by an unbiased estimator based on that PSF [48,22,37,36,38]. CRBs are computed for different noise conditions by appropriately choosing the noise distribution and the noise level relative to the signal level. For the 3D position estimation problem, CRBs for the X, Y, and Z dimensions are obtained from the diagonal elements of the inverse of the 3x3 Fisher information matrix [48,49].

For a given noise level, the position localization accuracy of a PSF is best when the intensity of the PSF spans the dynamic range of the detector. Because the energy

of the rotating PSF is distributed in two of its main lobes, for a given photon budget and NA, the peak intensity of the in-focus rotating PSF is lower than that of the standard PSF. In order to compare the best possible accuracies of the rotating and standard PSFs, the peak intensities of both PSFs should span the detector's dynamic range. This is possible in *detector-limited* systems, such as bright-field microscopes, where increasing the illumination intensity increases the intensity of the detected PSF. However, in *photon-limited* systems, the detected PSF intensity cannot be arbitrarily increased.

Tracking of fluorescent particles is indeed a good example of such a photon-limited problem. Because the excited state lifetime of a fluorescent molecule limits its emission intensity, any increase in the excitation intensity beyond a certain point would not help increase the number of emitted photons per unit time. Increasing the detector's exposure time is a common alternative. However, in fluorescent particle tracking situations where the particles are moving, large exposure times produce motion blurs in the detected image. Such systems, therefore, have an inherent limited photon budget for every detected image.

Introducing a DH-PSF mask in a photon-limited system distributes the available photons into two main lobes. If the detector parameters (exposure time, gain) are set so that a standard PSF spans the detector's dynamic range, the DH-PSF will not span the detector's dynamic range because of its lower peak intensity. This fact is critical in the photon-limited CRB calculations, and is fundamentally different from the CRB calculations of the detector-limited case [48].

Many well-designed systems can be considered shift-invariant, i.e. the PSF does not change in shape when an object point is moved in the transverse (X, Y) dimensions. Consequently, for a given noise level, the CRBs for X, Y, and Z dimensions for the entire 3D object volume can be completely described by three 1D plots: CRB_X, CRB_Y, and CRB_Z, as functions of axial distance [Chapter 3].

Accordingly, Fig. 4.2 compares the DH-PSF CRB and the standard PSF CRB for a photon-limited system with Poisson noise. This model can be used, for example, in a photon-limited system with a shot-noise limited detector. In Fig. 4.2, the signal to noise ratio (SNR) of the standard PSF is 30. SNR is defined as the ratio of the in-focus peak intensity to the noise standard deviation. For a given point source power, the peak of the in-focus DH-PSF is 7.18 times lower than the peak of the standard PSF, so its SNR is also lower. However, in the Poisson case, the noise standard deviation decreases with a decrease in the signal. Hence, the Poisson DH-PSF SNR is 11.2 ($30 / \sqrt{7.18}$).

For the Z dimension [Fig. 4.2(a)], the DH-PSF has lower CRB than the standard PSF, except in a region just outside the depth of field, where the standard PSF CRB is slightly lower. CRB values are very high in the depth of field of the standard PSF, indicating that axial position estimations in its focal region will have very poor accuracies. For the X dimension [Fig. 4.2(b)], the DH-PSF CRB is lower than the standard PSF CRB except exactly in the focal region. The standard PSF has identical CRBs for the X and Y dimensions because of its transverse symmetry but the DH-PSF CRB is higher for the Y than for the X dimension. The standard PSF CRB for Y

Fig. 4.2. Information theoretical comparison of DH and standard PSFs for a photon-limited system with Poisson noise. The system has 0.45NA, 40x magnification, 6.3µm pixel width, and 633nm wavelength. See text for explanation of SNR. (a-c) compare the CRBs of the DH and standard PSFs as a function of axial distance for the (a) Z, (b) X, and (c) Y dimensions. (d) compares CRB_{3D} of the DH and standard PSFs. DH-PSF has lower CRB_{3D} than the standard PSF in regions A (focal region) and C, while the standard PSF has lower CRB_{3D} in region B. CRB_{AVG} is lower for the DH-PSF than the standard PSF. DH-PSF, therefore, on an average, carries more information about the position of a particle than the standard PSF.

dimension is lower than that of the DH-PSF in the focal region [Fig. 4.2(c)]. However, outside the depth of field region, the DH-PSF has lower CRB.

Since most practical systems are required to locate and track particles over an extended axial range, it is useful to quantify the information content of the PSFs in all three dimensions and capture the essence of each PSF design in a single parameter. Therefore, we introduce a metric defined as the sum of the CRBs in all three dimensions, $CRB_{3D} = CRB_X + CRB_Y + CRB_Z$, and its average over the axial region of interest,

$$CRB_{AVG} = \frac{1}{\Delta Z} \int_{\Delta Z} CRB_{3D}(Z) \, dZ \qquad (2)$$

to quantify the overall performance of PSFs throughout the 3D volume.

For the parameters used in Fig. 4.2, the CRB_{3D} largely mimics CRB_Z, because for a 0.45NA objective, CRB_Z is much higher than CRB_X and CRB_Y. The DH-PSF performs better in the regions A and C of the plot, while the standard PSF does better in region B. CRB_{AVG} of the standard PSF is infinity, and that of the DH-PSF is 239 nm^2, which corresponds to an average combined standard deviation of 15.5nm in all three dimensions for a 0.45NA objective. DH-PSF is consequently better suited than the standard PSF for photon limited systems with Poisson noise. Moreover, the CRB_{3D} for the DH-PSF is more uniform throughout the whole range implying that a high 3D accuracy can be achieved over a long axial range.

2.1. Practical DH-PSF estimator

While the CRB gives the lowest possible estimator variance, it does not provide the means to achieve this variance. Maximum likelihood estimators can reach the CRB but are computationally intensive because they require iterative operations. The DH-PSF estimator used here is non-iterative as it directly uses the PSF lobes for 3D position estimation. Specifically, the transverse (X, Y) locations are estimated from the midpoint between the centroids of the two PSF lobes, while the axial location is estimated by mapping the angular orientation of the line joining the lobe centroids to axial distance using a look-up table. This estimator is fast when compared to a maximum likelihood estimator but it does not reach the CRB.

4.4   Fluorescence double-helix PSF microscopy

We now describe a DH-PSF system (Fig. 4.3) designed for fluorescent particle tracking in three dimensions. A phase-only spatial light modulator (SLM) was used to encode the DH-PSF mask.

The sample consisted of 1μm wide yellow-green fluorescent microspheres with 505nm excitation and 515nm emission peaks. These microspheres were excited with the 488nm Argon laser line. A half wave plate and a polarizer produced horizontally polarized light, as required for the SLM. A rotating diffuser destroyed the spatial coherence of the beam. While this was not critical for fluorescence imaging, it was required to avoid coherent artifacts when operating the system in bright field mode. Two lenses, one with 85mm focal length and the other with 100mm focal length,

collected the scattered light from the diffuser and focused it on the sample mounted on a piezo-stage.

The imaging path can be separated into a microscope section and a signal processing section. In the microscope section, a 1.3NA infinity corrected oil-immersion objective and a tube lens with 140mm focal length produced an 85x magnified image of the sample. A 515nm interference filter with a 10nm bandwidth, located in the infinity space of the microscope section, blocked the excitation beam. In the signal processing section of the imaging path, two achromatic lenses with focal length 125mm were aligned in a reflective 4f configuration such that the SLM was located at a distance of 125mm from both of the lenses. The plane of the SLM was slightly tilted relative to the optical axis to avoid the need for an imaging path beam splitter, which would waste 75% of the emitted photons. While this tilt causes the SLM plane to be tilted with respect to the Fourier plane of the signal processing section, the effect of this is negligible and can be corrected. Finally, an Andor iXon detector, placed 125mm from the second achromatic lens, recorded the image.

A linear phase was added to the DH-PSF phase mask, and the combination was phase wrapped (see top-right inset in Fig. 4.3), before loading the mask pattern into the SLM. This avoided the non-ideal 0th order response of the SLM by pushing the DH-PSF image to the SLM's 1st order. The undiffracted 0th order was essentially the same as a standard PSF image as it was unaffected by the DH-PSF mask (similar to the experiment in chapter 3).

Fig. 4.3. Experimental setup for three dimensional tracking of moving fluorescent particles: A horizontally polarized beam with 488nm wavelength excites 1μm wide yellow-green (Excitation peak: 505nm, Emission peak: 515nm) fluorescent microspheres. The microspheres are imaged by a 1.3NA oil-immersion infinity corrected objective and a tube lens. In the infinity space of the objective, a 515nm interference filter with 10nm bandwidth blocks out the excitation wavelength, and a polarizer passes only horizontally polarized emitted light. Finally, a phase-only spatial light modulator encoding the DH-PSF mask (top-right inset) engineers the system's PSF to have two rotating lobes. Unlike the standard PSF image which blurs the particles outside the focal region, the DH-PSF image encodes the particle's axial location in the angular orientation of its PSF lobes (bottom insets). The scale bar in the images represents 1μm.

In order to characterize the system's position localization accuracies, we imaged four fixed fluorescent microspheres embedded inside the volume of cured optical cement that has a refractive index 1.507. While the standard PSF image blurred the microspheres outside the focal region, the DH-PSF image encoded the axial position of the microspheres in the PSFs' rotating angles (bottom insets in Fig. 4.3). Each microsphere's transverse and axial positions were estimated using the practical centroid-based DH-PSF estimator. Section 4.7 presents details of the calibration and correction methods.

We estimated the position of the four microspheres by recording 100 successive images. From these data we were able to determine the standard deviation of the position estimation. *The single-image* standard deviations were $(\sigma_X, \sigma_Y, \sigma_Z)$ = (14nm,13nm,37nm), on an average among the studied particles (see Section 4.7 for details). Because these microspheres were fixed, we could average the 100 estimations. The standard deviation of the average estimate was $(\sigma_{\overline{X}}, \sigma_{\overline{Y}}, \sigma_{\overline{Z}})$ = (3nm, 3nm, 6nm) for the four particles.

It is important to note that these accuracies do not represent the fundamental limit of the DH-PSF system in Fig. 4.3. CRB calculations of a similar system with 1.3NA, 100x magnification, 4.4μm pixel width, 514.5nm emission wavelength peak, and an SNR of 11.2 revealed the single-image position localization limits to be $(\sigma_X, \sigma_Y, \sigma_Z)$ = (0.5nm,0.9nm,0.7nm) for an in-focus particle. These accuracies can potentially be

achieved using more complex estimators, carefully calibrated detectors, and a more stable optical setup[1].

4.5   3D tracking of fluorescent microparticles

We extended the procedure to track moving fluorescent particles by recording DH-PSF images at regular time intervals.

Fig. 4.4 shows movies of 3D tracking of four fluorescent microspheres with the DH-PSF system. These microspheres are moving inside a blob of cured optical cement that has water trapped within it. While microspheres 2, 3, and 4 are moving in water, the microsphere 1 is relatively immobile as it is attached to optical cement. Except for particle 4, which moves out of the field of view and later reappears, all other particles are within the field of view for the entire time of the movie (10 seconds). 100 images of the moving microspheres are recorded with an exposure time of 100ms.

In the standard PSF movie [Fig. 4.4(a)], the transverse motion of the microspheres is detectable because of the corresponding transverse displacement of the PSF. However, the axial displacements of the particles cause their PSFs to blur, and consequently bury in noise. In contrast, in the DH-PSF movie [Fig. 4.4(b)], both transverse and axial displacements of the microspheres are detectable from their

---

[1] In addition to the photon noise considered in the CRB calculations, the above experimental standard deviations are also affected by the nanoscale vibrations in the optical setup caused by components such as the water-cooled Argon laser and the rotating diffuser. Tighter vibration control conditions could help approach the DH-PSF CRB limit for a given SNR.

corresponding PSFs. When a micosphere moves in the transverse dimension, as in the standard PSF case, the DH-PSF cross-section also moves in the transverse dimension. Consequently, the instantaneous transverse position of the microsphere can be estimated from the midpoint of its PSF lobes. As the microsphere moves in the axial dimension, its PSF rotates. The microsphere's instantaneous axial position can thus be determined by mapping the rotation angle of its PSF to the axial dimension using the calibration plot [Fig. 4.6(a)]. With the knowledge of each microsphere's 3D locations every 100ms, the motion of the microspheres can be tracked, as shown in
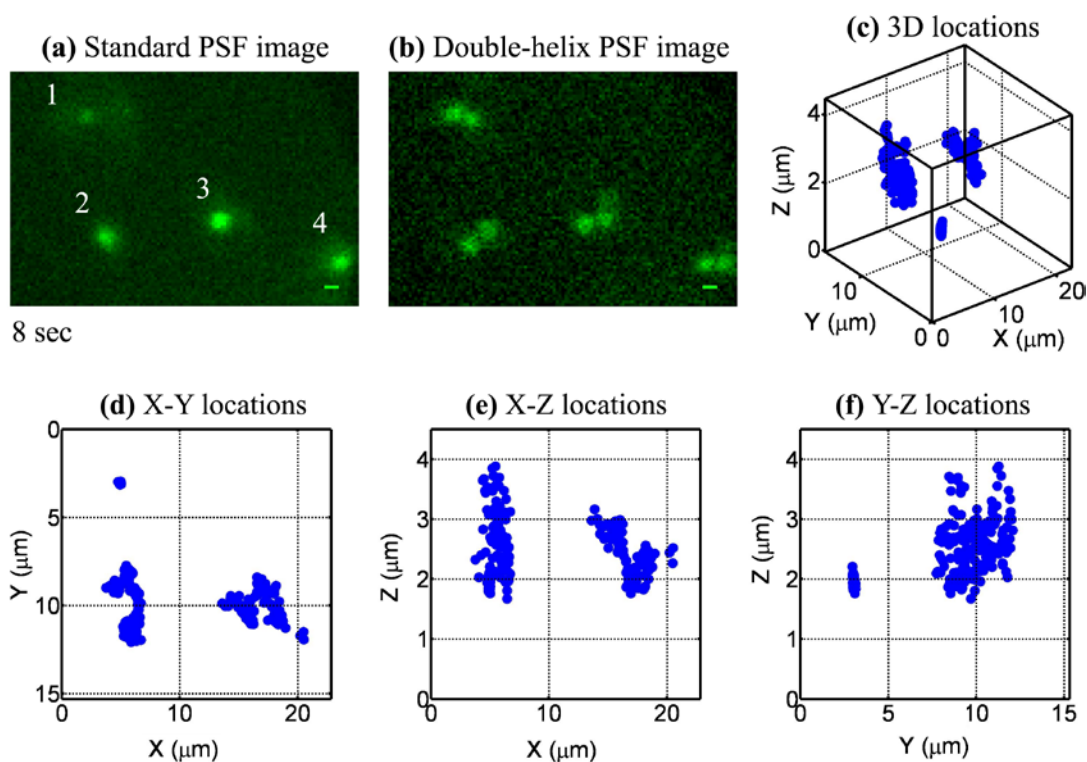
Fig. 4.4. Movies of fluorescent microsphere tracking in three dimensions. The first movie [See movie from Opt. Exp. **16**, 22048 (2008)] (a-c) shows (a) the DH-PSF image, (b) the standard PSF image, and (c) the 3D locations of four microspheres. The second movie [See movie from Opt. Exp. **16**, 22048 (2008)] (d-f) displays X-Y, X-Z, and Y-Z projections of the microspheres' 3D locations.

Fig. 4.4(c). Figs. 4.4(d-f) shows the X-Y, X-Z, and Y-Z projections of the 3D tracking plot of Fig. 4.4(c), and also show that particle 1 is immobile in the transverse dimensions, but does move a bit in the axial dimension. This subtle axial movement is undetectable in the standard PSF movie of Fig. 4.4(a).

3D tracking also facilitates the determination of velocities of the fluorescent microspheres. Fig. 4.5(a-c) shows the velocities averaged over 100ms for the particles 1, 2, and 3 in all three dimensions.
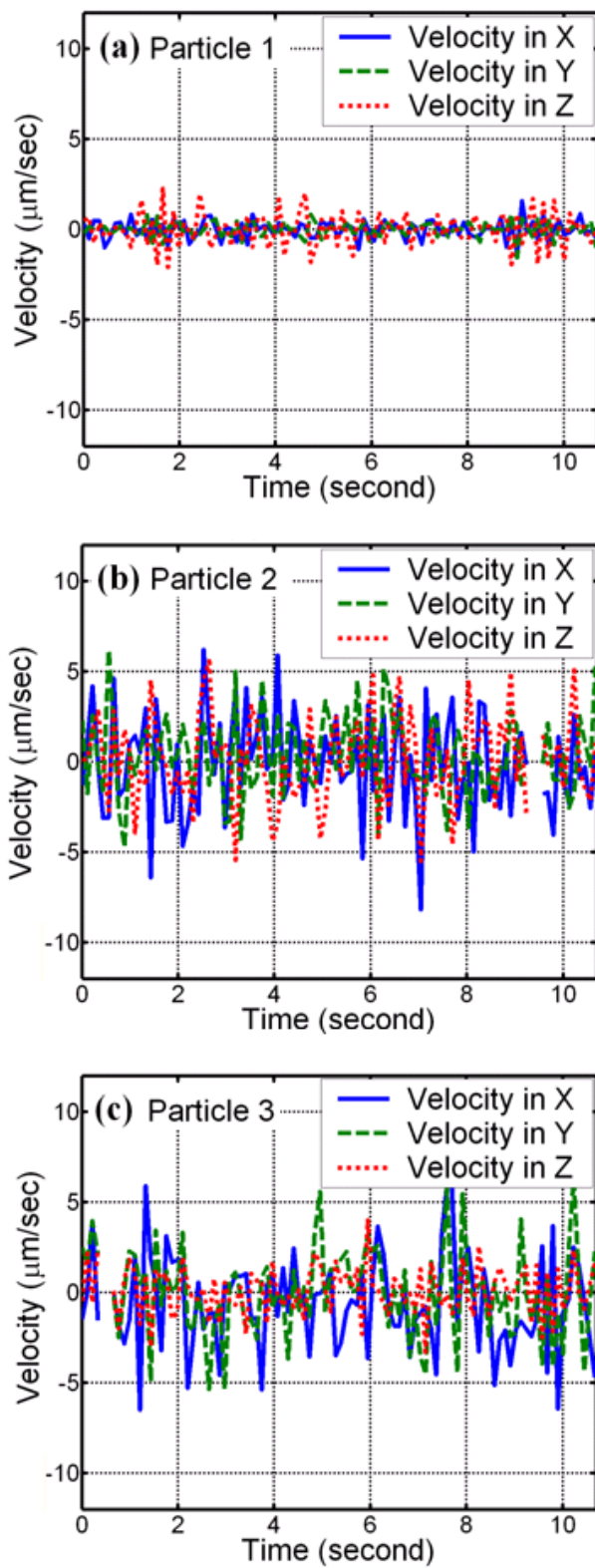
Fig. 4.5. Time-varying velocities in all three dimensions for (a) particle 1, (b) particle 2, and (c) particle 3.

4.6 Summary

We have demonstrated photon-limited tracking of fluorescent particles using a computational optical system with a DH-PSF. Because it is possible to estimate the 3D position of multiple particles over a long axial range with a single DH-PSF image and using a fast estimator, this technique is attractive to track multiple particles in real time in three dimensions. An information theoretical analysis shows that the DH-PSF carries higher average 3D information over a longer range than a standard PSF. It also shows that subnanometer accuracies are achievable with the DH-PSF using improved estimators.

4.7 Appendix: Calibration, correction, estimation precisions

4.7.1 Calibration and detailed estimations

A calibration plot (Fig. 4.6). that maps rotation angles to axial locations was obtained by translating the piezo-stage holding the sample in steps of $0.8\mu m$ over a $5.6\mu m$
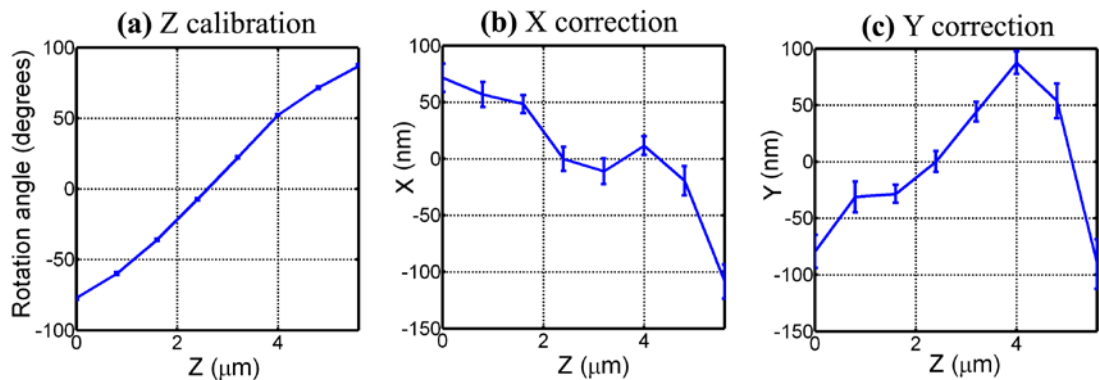
Fig. 4.6. (a) Calibration plot that maps rotation angle to axial distance. Correction factors for (b) X and (c) Y dimensions that are used in transverse position estimation.

range, and by estimating the DH-PSF angle of particle 4 (in bottom inset of Fig. 4.3) from 20 successively recorded images at each location.

Because of system aberrations, including sample induced aberrations, the transverse location of an object point is not exactly the midpoint of the centroids of the two PSF lobes for all axial locations. Corrections were applied to the midpoint to determine the exact transverse location. The X and Y coordinates of the midpoint of the lobe centroids of particle 4 were plotted as a function of the axial distance to obtain correction factors, Xcr [Fig. 4.6(b)] and Ycr [Fig. 4.6(c)]. These correction factors were subtracted from the lobe midpoint location to obtain the transverse position of a particle. Similar curves for other particles within the field of view confirmed that these corrections are effectively shift-invariant. These plots also account for an additional minor correction that compensates for the slight asymmetry of the DH-PSF (see Fig. 4.1), which also shifts the midpoint of the lobes' centroids as the system is defocused. For the system in Fig. 4.3, the standard deviation of this movement was theoretically calculated to be 2nm and 5nm for the X and Y dimensions.

Table 1: Positions and standard deviations of the four fluorescent microspheres shown in Fig. 4.3.

Micro-sphere	$\overline{X}$ (μm)	$\overline{Y}$ (μm)	$\overline{Z}$ (μm)	X accuracy (nm)				Y accuracy (nm)				Z accuracy (nm)			
				σ_{Xm}	$\sigma_{\overline{Xcr}}$	σ_X	$\sigma_{\overline{X}}$	σ_{Ym}	$\sigma_{\overline{Ycr}}$	σ_Y	$\sigma_{\overline{Y}}$	σ_{Za}	$\sigma_{\overline{Zcl}}$	σ_Z	$\sigma_{\overline{Z}}$
1	3.148	0	2.055	14	2	**14**	**3**	11	3	**11**	**3**	41	6	**41**	**8**
2	2.241	7.809	0	11	2	**11**	**2**	11	2	**11**	**2**	31	5	**31**	**6**
3	0	9.712	0.690	17	2	**17**	**3**	17	2	**17**	**3**	43	5	**43**	**6**
4	1.925	13.006	0.962	13	2	**13**	**3**	11	2	**11**	**2**	31	5	**31**	**6**

Table 1 lists the positions ($\overline{X}, \overline{Y}, \overline{Z}$) and standard deviations for all four particles in Fig. 4.3. σ_X, σ_Y, and σ_Z refer to the standard deviations along the X, Y, and Z dimensions, respectively. σ_X and σ_Y of a particle were computed from the standard deviation (σ_{Xm}, σ_{Ym}) of the midpoint (Xm, Ym) of the lobes of the particle, and the standard deviation ($\sigma_{\overline{Xcr}}$, $\sigma_{\overline{Ycr}}$) of the correction factors averaged over the 20 measurements. σ_Z is computed from the standard deviation (σ_{Za}) of the rotation angle (Za) estimation, and the standard deviation ($\sigma_{\overline{Zcl}}$) of the Z calibration (Zcl) averaged over the 20 measurements. Specifically, $\sigma_X = (\sigma_{Xm}^2 + \sigma_{\overline{Xcr}}^2)^{1/2}$, $\sigma_Y = (\sigma_{Ym}^2 + \sigma_{\overline{Ycr}}^2)^{1/2}$, and $\sigma_Z = (\sigma_{Za}^2 + \sigma_{\overline{Zcl}}^2)^{1/2}$. σ_{Xm}, σ_{Ym}, and σ_{Za} are obtained as the standard deviation of the 100 estimates. $\sigma_{\overline{Xcr}}$, $\sigma_{\overline{Ycr}}$, and $\sigma_{\overline{Zcl}}$ are calculated as the standard deviation of the average of 20 estimates.

The standard deviation of the average of N estimates is smaller than the standard deviation of each of N estimates by a factor of $(N)^{1/2}$. Because the correction and calibration plots are obtained from an average of 20 estimates, the standard deviations $(\sigma_{\overline{Xcr}}, \sigma_{\overline{Ycr}}, \sigma_{\overline{Zcl}})$ of the average estimates are determined by dividing the standard deviation of each estimate by $(20)^{1/2}$. However, σ_{Xm}, σ_{Ym}, and σ_{Za} are the standard deviations of a single estimate. σ_X, σ_Y, and σ_Z listed in the table therefore represent single-image position estimation standard deviations. In other words, σ_X, σ_Y, and σ_Z are the accuracies when only one image is used for position estimation.

For fixed particles, the estimation accuracy can be improved by recording multiple images. Indeed, when estimates of Xm, Ym, and Za from 100 images are averaged, the average estimates ($\overline{Xm}$, $\overline{Ym}$, and $\overline{Za}$) will have a factor of $(100)^{1/2}$ reduction in standard deviation ($\sigma_{\overline{Xm}}, \sigma_{\overline{Ym}}, \sigma_{\overline{Za}}$). The standard deviations of the average position estimates ($\overline{X}, \overline{Y}, \overline{Z}$) are $\sigma_{\overline{X}} = (\sigma_{\overline{Xm}}^2 + \sigma_{\overline{Xcr}}^2)^{1/2}$, $\sigma_{\overline{Y}} = (\sigma_{\overline{Ym}}^2 + \sigma_{\overline{Ycr}}^2)^{1/2}$, and $\sigma_{\overline{Z}} = (\sigma_{\overline{Za}}^2 + \sigma_{\overline{Zcl}}^2)^{1/2}$. The average values of $\sigma_{\overline{X}}, \sigma_{\overline{Y}}$, and $\sigma_{\overline{Z}}$ for all four particles were 3nm, 3nm, and 6nm, respectively.

It is worth emphasizing that (typically slower) optimal estimators and tight vibration control conditions could help reach the DH-PSF CRB limit for a given SNR.

Chapter 5

3D Super-resolution Imaging with a Double-helix

Microscope

We demonstrate single-molecule fluorescence imaging beyond the optical diffraction limit in three dimensions with a wide-field microscope that exhibits the double-helix point spread function (DH-PSF). Single fluorescent molecules in a thick polymer sample are localized in single 500 ms acquisitions with 10-20 nanometer precision over a large depth of field (2 μm) by finding the center of the two DH-PSF lobes. Using a new photoactivatable fluorophore, repeated imaging of sparse subsets with a DH-PSF microscope provides super-resolution imaging of high concentrations of molecules in all three dimensions. The combination of optical PSF design and digital post-processing with photoactivatable fluorophores opens up new avenues for improving three-dimensional imaging resolution beyond the Rayleigh diffraction limit.

5.1 Introduction

Fluorescence microscopy is ubiquitous in biological studies because light can noninvasively probe the interior of a cell with high signal-to-background and remarkable label specificity. Unfortunately, optical diffraction limits the transverse (x-y) resolution of a conventional fluorescence microscope to approximately $\lambda/(2NA)$, where λ is the optical wavelength and NA is the numerical aperture of the

objective lens [50]. This limitation requires that point sources need be more than about 200 nm apart in the visible wavelength region in order to be distinguished with modern high-quality fluorescence microscopes. Diffraction causes the image of a single point emitter to appear as a blob (i.e., the point-spread function or PSF) with a width given by the diffraction limit. However, if the shape of the PSF is measured, then the center position of the blob can be determined with a far greater precision (termed super-localization) that scales approximately as the diffraction limit divided by the square root of the number of photons collected, a fact noted as early as Heisenberg in the context of electron localization with photons [51] and later extended to point objects [52,53] and single-molecule emitters [54,55,31,38]. Because single-molecule emitters are only a few nm in size, they represent particularly useful point sources for imaging, and super-localization of single molecules at room temperature has been pushed to the one nanometer regime [56] in transverse (two-dimensional) imaging. In the third (z) dimension, diffraction also limits resolution to $\sim 2n\lambda/NA^2$ with n the index of refraction, corresponding to a depth of field of about 500 nm in the visible with modern microscopes. Improvements in three-dimensional localization beyond this limit are also possible using astigmatism [26, 46], defocusing [27], or simultaneous multiplane viewing [57].

Until recently, super-localization of individual molecules was unable to provide true resolution beyond the diffraction limit (super-resolution) because the concentration of emitters had to be kept at a very low value, less than one molecule every $(200\ nm)^2$, to prevent overlap of the PSFs. In 2006, three groups independently proposed localizing sparse ensembles of photoswitchable or photoactivatable

molecules as a solution to the "high concentration problem" to obtain super-resolution fluorescence images [3,4,5] (denoted PALM, STORM, F-PALM, respectively). A final image is formed by summing the locations of all single molecules derived from imaging the separate randomly generated sparse collections. Variations on this idea have also appeared, for example, by using accumulated binding of diffusible probes [58] or quantum dot blinking [59]. Importantly, several of these techniques have recently been pushed to three dimensions using astigmatism [9], multiplane methods [10], and two-photon activation by temporal focusing [11] to quantify the z-position of the emitters. In the astigmatic case, the depth of field was only about 600 nm, whereas in the extensively analyzed [57] multiplane approach, the maximum depth of field was about 1 μm, which has been recently extended to 2.5 μm with bright quantum dot emitters [60].

In this chapter, we present a method for three-dimensional super-resolution with single fluorescent molecules where the PSF of the microscope has been engineered with a DH-PSF mask [35] (see Fig. 5.1). In the previous chapters, we used the DH-PSF to localize detector-limited point scatterers inside the volume of a glass slide [48], and to track moving fluorescent microspheres [49]. Here, we show that a particularly useful photon-limited source, a single-molecule emission dipole, can be imaged far beyond the diffraction limit using a DH-PSF. In thick samples, we demonstrate super-localization of single fluorescent molecules with precisions as good as 10 nm laterally and 20 nm axially over axial ranges greater than 2 μm. Further, we also show that three-dimensional super-resolution imaging of high concentrations of single molecules in a bulk polymer sample can be achieved using a

new photoactivatable 2-dicyanomethylene-3-cyano-2,5-dihydrofuran (DCDHF) fluorophore, a modification of the recently reported azido-DCDHF [61]. Two molecules as close as 14nm (x), 26nm(y), and 21nm (z) are resolved by this technique. The ideas presented here should be broadly applicable to super-resolution imaging in various fields ranging from single emitters in solid hosts for materials science applications to biological and biomedical imaging studies.

5.2   Single molecule imaging in a double-helix PSF system

The 3D positions of multiple sparse molecules are estimated with a single wide-field fluorescence image using the DH-PSF design as follows. The imaging system is composed of a sample located at the objective focal plane of a conventional inverted microscope and an optical signal processing section as shown in Fig. 5.1a. The signal processing section is a 4f imaging system with a reflective phase-only spatial light modulator (SLM) placed in the Fourier plane. Specifically, an achromatic lens L1 placed at a distance f from the microscope's image plane produces the Fourier transform of the image at a distance f behind the lens. The phase of the Fourier transform is modulated by reflection from the liquid crystal of the SLM. Because the SLM is sensitive only to vertically polarized light, a vertical polarizer P is placed immediately after the SLM to block any horizontally polarized light not modulated by the SLM. The final image is produced by another achromatic lens L2 (f = 15cm) placed at a distance f after the SLM and recorded with an electron-multiplying CCD (EMCCD) camera.
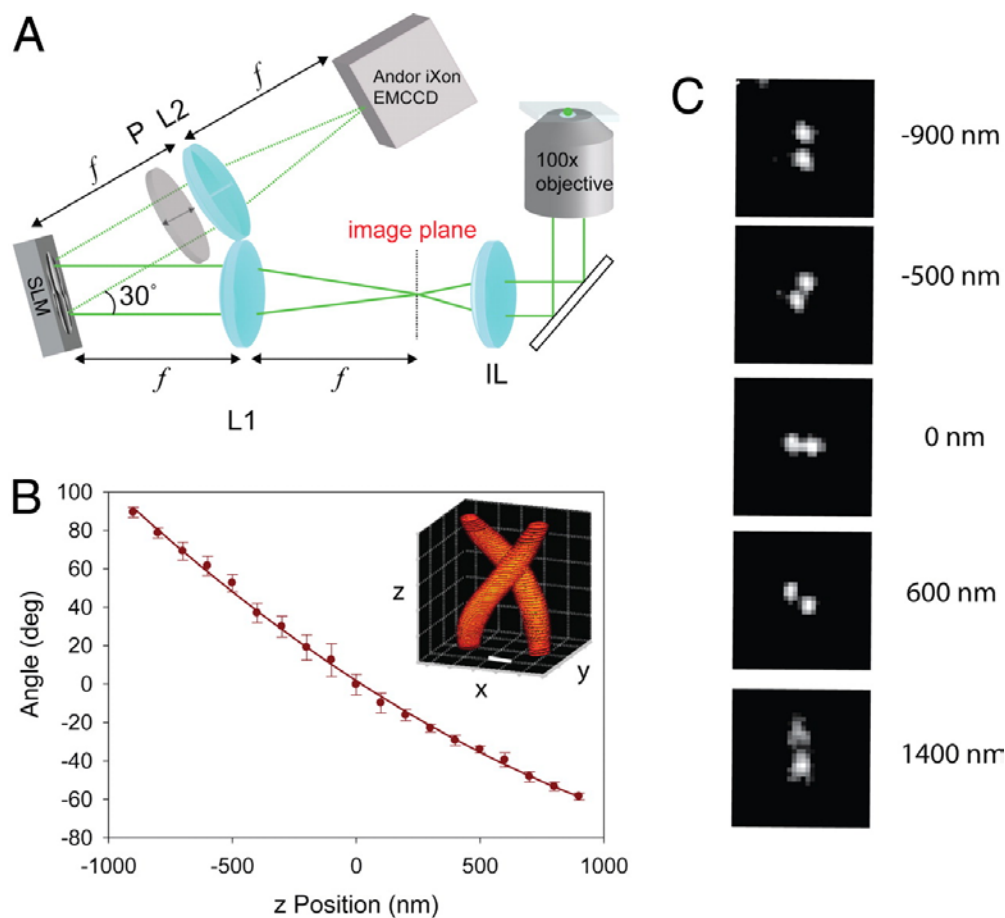
Fig. 5.1: a) Collection path of the single molecule DH-PSF setup. IL is the imaging lens of the microscope, L1 and L2 are focal length matched achromatic lenses, and SLM is a liquid crystal spatial light modulator. b) Typical calibration curve of angle between two lobes with respect to the horizontal versus axial position measured with a piezo-controlled objective. Inset: 3D plot of the DH-PSF intensity profile (Scale bar: 400nm). c) images of a fluorescent bead used for the calibration curve in b) at different axial positions, with 0 being in focus.

When the SLM is loaded with the DH-PSF phase-mask [35], the Fourier transform of the sample image is multiplied by the DH-PSF transfer function. Equivalently, every object point is convolved with two DH-PSF lobes, with the angular orientation of the lobes depending on the axial location of the object above or below focus. The lobes are horizontal when the emitter is in focus. As the emitter is

moved towards the objective, the DH-PSF lobes rotate in the counter-clockwise direction. On the other hand, if the emitter is moved away from the objective the lobes rotate in the clockwise direction. When a sample comprises multiple sparse molecules at different 3D positions, the detected DH-PSF image will exhibit two lobes (with different angular orientations) for each molecule. The transverse (x-y) position of a molecule is estimated from the midpoint of the line connecting the positions of the two lobes, and the axial position is estimated from the angle of the line connecting the two lobes using a calibration plot that maps angles to axial positions. An example calibration plot of angle versus z position is shown in panel b of Fig. 5.1. The inset in Fig. 5.1b is a simulation of the three dimensional shape of the DH-PSF. Figure 5.1c also shows actual DH-PSF images taken from a fluorescent bead at different z positions illustrating the type of data used to extract the calibration plot. The beads (pumped with 514 nm) have an emission spectrum with a peak at about 580 nm.

Unlike DH-PSF experiments of Chapters 2, 3, and 4, the need for blazed encoding of the DH-PSF phase mask was avoided in the single-molecule experiment of Fig. 5.1 by using an SLM with close to 100% fill factor. This significantly increases the light throughput system by imaging all emitted photons in one diffraction order, and makes the mask implementation less chromatic, which in turn permits the use of emission filters with a wider bandwidth, thereby further increasing the light throughput. These improvements in efficiency and the use of an EMCCD are critical in enabling a DH-PSF fluorescence microscope to detect single molecules.

5.3   Localizing single molecule positions

Although we demonstrated the imaging of highly fluorescent beads with the DH-PSF in the Chapter 5 [49], it is critical to demonstrate useful imaging of single molecules because the much lower signal-to-background inherent in a typical single-fluorophore experiment taxes any imaging system and highlights areas for future development. Single-molecule imaging can be impeded by the >75% loss (50% because of the polarizer and the rest because of SLM reflection losses) associated with the SLM device. Nevertheless, we have achieved 3D localization precision that compares well with previous approaches while more than doubling the available depth of field. Figure 5.2 shows the results from the localization of one single molecule in a ~2µm thick poly(methyl methacrylate) (PMMA) film. The molecule is a derivative of the previously described class of photoswitchable fluorogenic azido-DCDHF molecules, specifically   (*E*)-2-(4-(4-Azido-2,3,5,6-tetrafluorostyryl)-3-cyano-5,5-dimethylfuran-2(5*H*)-ylidene)malononitrile, abbreviated as DCDHF-V-PF$_4$-azide (see section 5.8.5 for structure). This molecule was chosen for this study because (1) the azido-DCDHF class of fluorophores emit on the order of 10^6 photons before photobleaching [61] (an order of magnitude more than photoswitchable fluorescent proteins), (2) the molecule has a suitable emission wavelength for our SLM, and (3) a relatively small amount of blue light irradiance is necessary for photoactivation. For the data shown, the fluorogenic azide functionalized molecule was previously irradiated with 407 nm light to generate the amine functionalized emissive form [61]. For imaging, the molecule was pumped with 514 nm and the fluorescence peaking at 580 nm was

recorded for 500 ms/frame to yield images similar to Fig. 5.2b. The synthesis and optical properties of the molecule can be found in section 5.8.5.
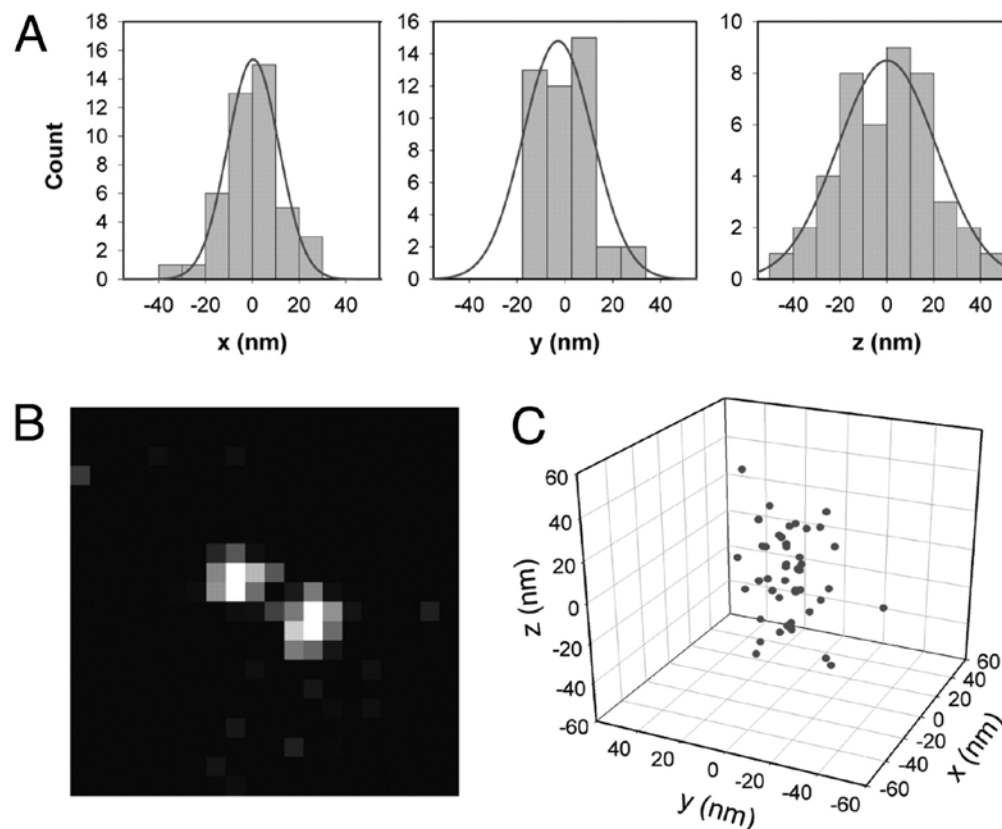
Fig. 5.2. 3D localization of a single molecule. (*A*) Histogram of 44 localizations of one single photoactivated DCDHF-V-PF$_4$ molecule in *x*, *y*, and *z* in a layer of PMMA. The standard deviations of the measurements in *x*, *y*, and *z* are 12.8, 12.1, and 19.5 nm, respectively. The smooth curve is a Gaussian fit in each case. An average of 9,300 photons were detected per estimation on top of background noise fluctuations of 48 photons per pixel. (*B*) Representative single-molecule image with DH-PSF acquired in one 500-ms frame. (*C*) Localizations plotted in 3 dimensions.

In this work, the location of each single molecule was determined using two different schemes (see section 5.8). The first method found the center of each DH-PSF lobe using a least-squares Gaussian fit, then determined the midpoint between

the centroid positions to define the x,y position of the bead, and finally obtained the angle between the centroid positions, which gave the z position of the emitter. The second method, which was considerably more computationally efficient than the first, determined the positions of the lobes of the PSF using a simple centroid calculation. The first procedure gives better precision measurements than the second, although it is less robust in that it requires a fairly symmetric shape to obtain a good fit. The data in Figure 5.2 was analyzed using the first scheme, and data for the large number of molecules in Figures 5.3 and 5.4 was analyzed using the second scheme for computational convenience.

The three-dimensional position of one single molecule was estimated 44 times and the histograms of the three spatial coordinates of the molecule are presented in Fig. 5.2a. The molecule was found to have a mean z position of 644 nm above the standard focal plane. Each estimation used an average of 9300 photons with an average rms background fluctuation of 48 photons per pixel. The histograms in Fig. 5.2a must be regarded as a population of successive position determinations which have a population standard deviation, or localization precision, of 12.8, 12.1, and 19.5 nm in x, y, and z, respectively. The x-direction is defined as the orientation of the line between the two DH-PSF lobes for a molecule at z=0 in Fig. 5.1. These values should be regarded as the expected localization precision for a single measurement. As is well-known, if all the 44 position measurements in Fig. 5.1a are combined, the result will have a far better localization precision as would be expected from the scaling of the standard error of the mean (i.e., the inverse of the square root of the number of measurements or 6.6 times smaller), but in many studies, multiple

localizations of the same single molecule may not be possible. The localization

precision of our method is within the same range as both the astigmatic [9] and

multiplane techniques [10], while simultaneously more than doubling the depth of

field. It is worth noting that the simple estimators reported here are not statistically

efficient since they do not reach the Cramer-Rao bound for the DH-PSF [49]. This

indicates that the simple estimators are not currently using all of the possible

information contained in the images, and that there is room for significant

improvement through the choice of a better estimator. Also, the system can be made

more photon-efficient by using a custom DH-PSF phase mask, which would take

away the need for a polarizer, and would avoid the SLM losses. These and other

improvements in background minimization and drift correction should allow for

improved localization precision in the future.

5.4   Double-helix PSF imaging of single molecules in a thick sample

The DH-PSF imaging system can be used to identify the 3D position of many

molecules in a single image as long as the PSFs from the different emitters do not

appreciably overlap. Fig. 5.3 demonstrates this capability using a sample containing a

low concentration of the fluorophore DCDHF-P [62] (see section 5.8 for structure)

embedded in a ~2 μm thick PMMA film. Fig. 5.3a compares the standard and the

DH-PSF images of two molecules at different 3D positions selected to be fairly close

to the focal plane for purposes of illustration only. Notable in the DH-PSF image is a

slightly increased background compared to the standard PSF, a property which arises

from the distribution of photons between the DH-PSF lobes
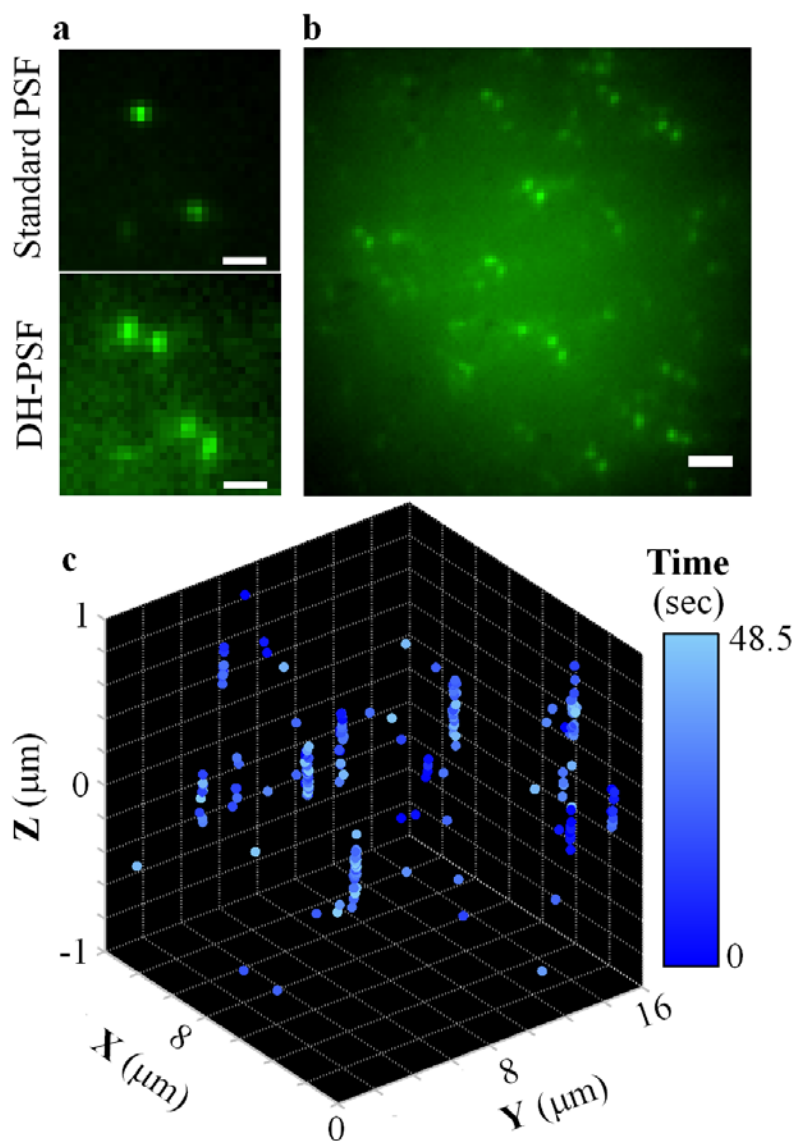
Fig. 5.3. 3D super-localizations of a low concentration of DCDHF-P molecules in a thick PMMA sample. (a) Comparison of the standard PSF (i.e., *Upper*, SLM off) to the DH-PSF image of 2 molecules (*Lower*, SLM on). (Scale bar: 1 µm.) (b) Representative image of many single molecules at different x, y, and z positions. (Scale bar: 2 µm.) (c) 4D (x, y, and z, time) representation of single-molecule position determinations during a sequence of 97 frames, with a color map showing the time of acquisition.

over a long axial range. In general, molecules away from the focal plane appear quite blurry in the standard PSF image. In contrast, the DH-PSF image encodes the axial position of the molecules in the angular orientation of the molecules' DH-PSF lobes, which are distinctly above the background with approximately the same intensity through the entire z range of interest. This increased depth-of-field is illustrated directly in Fig. 5.3b, which shows a representative DH-PSF image of multiple molecules in a volume.

Each molecule is seen to exhibit two lobes oriented at an angle that is uniquely related to its axial position. This image is obtained by averaging 97 successive frames recorded with a 500ms exposure time. Fig. 5.3c shows the 3D positions of molecules extracted from each of these 97 frames as a function of time in the imaging sequence (encoded in the colormap). Molecules were localized below the diffraction limit over an axial range of 2 μm. Molecules that were localized more than once are shown as a spread of points, each representing a single localization event. This apparent spread is not due to drift, but is rather an ensemble of multiple position determinations as in Fig. 5.2a.

5.5   Imaging of molecules spaced closer than the diffraction limit

When a large concentration of fluorophores is present, repeated photo-activation, image acquisition, localization, and photobleaching of non-overlapping subsets of fluorescent molecules provides resolutions beyond the classical diffraction limit (super-resolution). Fig. 5.4 shows that three-dimensional super-resolution can be

achieved with a DH-PSF system. We used the fluorogenic DCDHF-V-PF$_4$-azide as our photoactivatable molecule, again in a thick film of PMMA. Subsets of the

Fig. 5.4. 3D super-resolution imaging. (a) High concentrations of single molecules of DCDHF-V-PF4-azide in a thick PMMA sample image using the PALM/STORM/F-PALM method with the DH-PSF as described in the text. Color indicates total number of photons used for estimation after background correction. (b) Zoom-in of position estimations for molecules 1 and 2 (blue and red, respectively) separated by 14 nm (x), 26 nm (y), and 21 nm (z); Euclidean distance (green): 36 nm. (Scale bar: 20 nm.) (c) Image from activation cycle 1 showing molecule 1. (d) Image from later in cycle 1 confirming that molecule 1 bleached. (e) Image from activation cycle 2 showing molecule 2. (Scale bar: C–E, 1μm.)

molecules were photoactivated with 407nm light, and then excited with 514 nm light to image the fluorescent emission centered at 578nm. Accordingly, a DH-PSF mask designed for 578nm was loaded into the SLM. The power and the duration of the purple 407nm beam were chosen so that only a sparse subset of molecules activate in each cycle.

Fig. 5.4a shows the 3D average position of each molecule extracted from 30 activation cycles, with 30 (500ms) frames per activation. The colormap encodes the total number of photons available for position localization. Fig. 5.4b shows a zoomed-in view of two molecules establishing the super-resolving capability of the method: these two molecules are separated by 14nm (X), 26nm (Y), and 21nm (Z), for a Euclidean distance of 36nm. Fig. 5.4 c-e shows the corresponding images for these two molecules during two consecutive activation cycles. The initially emissive first molecule (Fig. 5.4c) bleaches near the beginning of an activation/imaging cycle (Fig. 5.4d), and the second molecule starts emitting precisely after the second activation, about 9.5 seconds after the first molecule bleached. Since the dark time gap is far larger than the blinking time scale for these molecules (~100's of ms), and because these molecules are photoactivatable, but not photoswitchable, the molecules that appear in different imaging cycles (Fig. 5.4c and Fig. 5.4e) must be different molecules. In future work, where photoactivatable or photoswitchable molecules are labeling a particular structure, super-resolution information can be extracted as long as the labeling density is sufficiently high to satisfy the Nyquist criterion [63].

5.6   Summary

The DH-PSF provides a powerful new tool for 3D super-localization and super-resolution imaging of single molecules. By encoding the z-position in the angular orientation of two lobes in the image, the x, y, and z positions of each single emitter can be determined well beyond the optical diffraction limit. Moreover, the DH-PSF enables 3D imaging with greater depth of field than is available from other imaging methods. Despite losses from the insertion of an SLM into the imaging system, single small molecules can in fact be localized with precision in the 10-20 nm range in three dimensions with single images. It is expected that future improvements in the phase mask design, the use of a custom phase mask, optimized estimators, background minimization, and a closed-loop drift correction will lead to even further improvements in resolution. With the proofs-of-principle reported here, the path is open to implementation of these ideas in a range of areas of science, including the study of materials for defect characterization, the quantum optical generation of novel optical fields using subwavelength localization of properly coupled single emitters, the use of single molecules to characterize nanostructures, and 3D biophysical and biomedical imaging of labeled biomolecules inside and outside of cells.

5.7   Appendix I: Methods — Sample preparation, imaging, and analysis

5.7.1 Sample preparation

Axial position calibration data were obtained at two different emission wavelengths, 515 nm and 580 nm, using fluorescent beads (Fluospheres 505/515, 200 nm, biotin

labeled, and Fluospheres 565/580, 100 nm, carboxylated, both from Molecular Probes) immobilized in a spin-coated layer of 1% poly(vinyl alcohol) (72000 g/mol, Carl Roth Chemicals) in water; the polymer solution was cleaned with activated charcoal and filtered before being doped with beads. Single-molecule samples were prepared by doping a nanomolar concentration of DCDHF-P [62] into a 10% solution of poly(methyl methacrylate) (T_g = 105°C, MW = 75,000 g/mol atactic, polydispersity ~ 7.8, Polysciences, Inc.) in distilled toluene that was spun (at 2000 RPM for 30 s with an acceleration time of 10,000 RPM/s) onto a plasma-etched glass coverslip to form a ~2 μm thick layer. The thickness was estimated by finding the axial in-focus position of various single molecules by scanning the z-position of the objective. The thick photoactivatable sample was made similarly using the molecule DCDHF-V-PF$_4$-azide, except that a layer of PVA containing 656/580 nm fluorescent beads was spun on top of the PMMA layer to incorporate fiduciary markers in the images.

5.7.2 Imaging

All epifluorescence images of both fluorescent beads and single molecules were collected with an Olympus IX71 inverted microscope equipped with a 1.4 NA 100x oil immersion objective. The filters used were a dichroic mirror (Chroma Z514RDC or z488RDC) and a longpass filter (Omega XF3082 and Chroma HQ545LP). The objective was fitted with a z-piezo adjustable mount (PIFOC p-721.CDQ stage with E625.CO analog controller, Physik Instrumente) that allowed for control of the z-position of the objective. The samples were imaged with either 488 nm (DCDHF-P)

or 514 nm (DCDHF-V-PF4-azide) circularly polarized excitation light (Coherent Innova 90 Ar$^+$ laser) with an irradiance of 1-10 kW/cm^2. Because some of the fluorogenic DCDHF-V-PF4-azide molecules were already activated, the molecules were first exposed to the 514 nm beam until most of them were bleached, leaving only a sparse subset of them in the fluorescent state. For further super-resolution imaging, molecules were photoactivated using circularly polarized 407 nm (Coherent Innova 300 Kr$^+$ laser) light with an irradiance of <1 kW/cm^2, which was chosen such that only a few molecules were turned on at a time. Images were then continuously acquired with 514 nm pumping with 500ms exposure time. After all of the molecules were bleached, the green beam was blocked and the purple beam was unblocked for 100ms to photo-activate additional molecules. The green beam was then unblocked for the next 15 seconds, until all of the activated molecules were bleached again. Each round of one 100-ms activation period and one 15-s imaging period constitutes one activation cycle. Thirty such cycles were required to obtain the data in Fig. 5.4. Mechanical shutters under computer control were used to define the timing of the imaging and activation beams.

In the collection path, a standard 4f imaging setup was utilized with a phase-only spatial light modulator (Boulder Nonlinear Systems XY Phase Series) programmed to generate the DH-PSF placed at the Fourier plane. The light exiting the sideport of the microscope was collected by a 15 cm focal length achromat lens (Edmund NT32-886) placed 15cm from the microscope's image plane (25.5 cm from the exit port). The SLM was placed 15 cm from this lens at a slight angle such that the phase modulated reflected beam would be diverted from the incoming beam by ~30°. The reflected

light passed through a polarizer and was then collected by another achromat lens 15 cm from the SLM. The real image was then focused onto an EMCCD (Andor Ixon[+]). Bead samples were imaged with no electron multiplication gain while single-molecule samples were imaged with a software gain setting of 250 yielding a calibrated gain of 224.5. The imaging acquisition rate for all single-molecule imaging was 2 Hz.

5.7.3 Analysis

Movies from the camera were exported by the Andor software as tiff stacks. The images were then analyzed with MATLAB. Two methods were used to determine the center position of each lobe of the DH-PSF. Briefly, a threshold was applied to remove background, and then the center position of each lobe of the DH-PSF was determined using either a least-squares Gaussian fit or a simple centroid calculation. The midpoint of the two centroids gave the x and y position of the emitter and the angle of the line connecting the two centroids with respect to the horizontal gave the axial position after conversion from degrees to nanometers using the calibration curve in Figure 5.1.

The average number of photons detected in each case were obtained by summing the fluorescence counts in a background corrected image coming from a molecule and then converting the A/D counts into photons. The conversion gain of our camera, 24.7 e⁻/count, was calibrated by a method described in the section 5.8.4 and the electron multiplication gain was calibrated to be 224.5 by measuring the increase in detected signal with gain versus that for no gain.

5.8   Appendix II: Estimation, calibration, and synthesis

5.8.1 Gaussian estimation scheme

In order to best assess the localization precision with the DH-PSF system, we developed a more complex nonlinear fitting algorithm for the molecule in Figure 5.2 than the one used for Figures 5.3 and 5.4. Each lobe was identified and isolated with a $(9 \text{ pixel})^2$ box. The lobes in the PSF were then each fit to a 2-D Gaussian using the MATLAB function, nlinfit, to extract an estimate of the center position of each lobe. Then the standard procedure for finding the x, y, and z positions of the molecule was applied — that is, using the angle of the line between the two lobe positions to extract z, and the midpoint to extract x and y. If the lobes of the PSF are symmetric, then this fitting procedure can give better results than a simple centroid fit, although it is significantly more complex computationally. For this molecule it offers a 15% improvement in localization precision in all three directions over the simpler centroid fit algorithm. For the large number of single molecules in Figures 5.3 and 5.4, we chose to use a centroid fitting scheme (described in the next section) both because the improvement is not overly significant for most molecules and because the centroid takes up less computational time.

In addition, for the data in Figure 5.2, a 100 nm fluorescent bead (Fluospheres 565/580, Molecular Probes, Inc.) was used as a fiduciary marker. Because the bead emits many more photons, its localization precision is much better than for a single molecule. Figure 5.5 shows the position fluctuations of the bead (b) and the molecule (a), and the dramatic improvement in z estimation drift (c) that results from subtracting the bead motion from the single-molecule z-estimations.
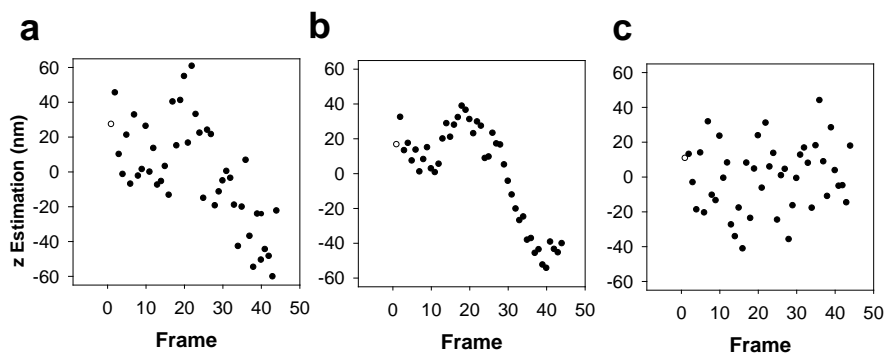
Fig. 5.5 : (a) Estimations of the z position of the DCDHF-V-PF$_4$ molecule featured in Fig. 5.2 of the main text. (b) Estimations of the z position of the fluorescent bead fiduciary in the sample, illustrating the z drift of the microscope and/or the z-piezo. (c) Fiduciary-corrected positions of the single molecule.

5.8.2. Estimation algorithm for 3D images

Each frame of the raw detected movies shows multiple molecules located over a transverse-position-dependent background that resembles the Gaussian intensity profile of the excitation beam. 3D positions of the molecules in each of these frames are estimated with an algorithm implemented in MATLAB. The algorithm first finds the coarse molecule positions from the raw image, and then zooms in on these coarse positions to find the exact 3D positions as explained below.

The non-uniform background prohibits the use of direct thresholding to identify molecules in the raw detected image. Hence, we used an edge detection algorithm that calculates the modulo-square of the gradient of the raw image to locate the coarse molecule positions. The gradient distinguishes the molecules from the slowly varying background by highlighting the edges around the molecules' response. The centroid of the area enclosed by the edges of a molecule is taken as the molecule's coarse x and y position. A (19 pixel)^2 region centered about the coarse position is then

extracted out to find the exact 3D molecule position. The two DH-PSF lobes present within this region are separated from the background using an adaptive thresholding technique. This technique finds the smallest threshold above the background such that the areas of the two lobes are maximized while remaining disconnected. The photon counts used for the colormap of Fig. 5.4 and in the horizontal axis of Fig. 5.6 are the photons counted from these maximum lobe-areas after background correction. The centroid coordinates of the two DH-PSF lobes were then computed. The axial position of the molecule was estimated by mapping the angle between the two centroid locations to axial distance using the calibration plot shown in Fig. 5.1 of the main text. The transverse molecule positions were estimated from the midpoint of the centroids of the DH-PSF lobes after applying a z-dependent transverse correction. This correction compensates for a small systematic change in tranverse position of the DH-PSF lobe centroid midpoint as a function of z, determined from fluorescent bead imaging with z-focus displacement produced by the piezo.

Finally, this estimation algorithm generated a 4D (3D spatial - temporal) dataset containing the molecule positions from different camera frames. This matrix is directly displayed in Fig. 5.3 of the main text. In Fig. 5.4, the temporal dimension was squeezed by replacing multiple localizations of a molecule within an activation cycle with the mean estimate. The precisions shown in the vertical axis of Fig. 5.6 are the standard deviations of estimates of the position for multiple molecules obtained from the above 4D dataset after a drift correction was made, based on correlation analysis of the single-molecule positions, which compensated for any linear stage drift along any of the three dimensions.

5.8.3 Localization precision as a function of the number of detected photons
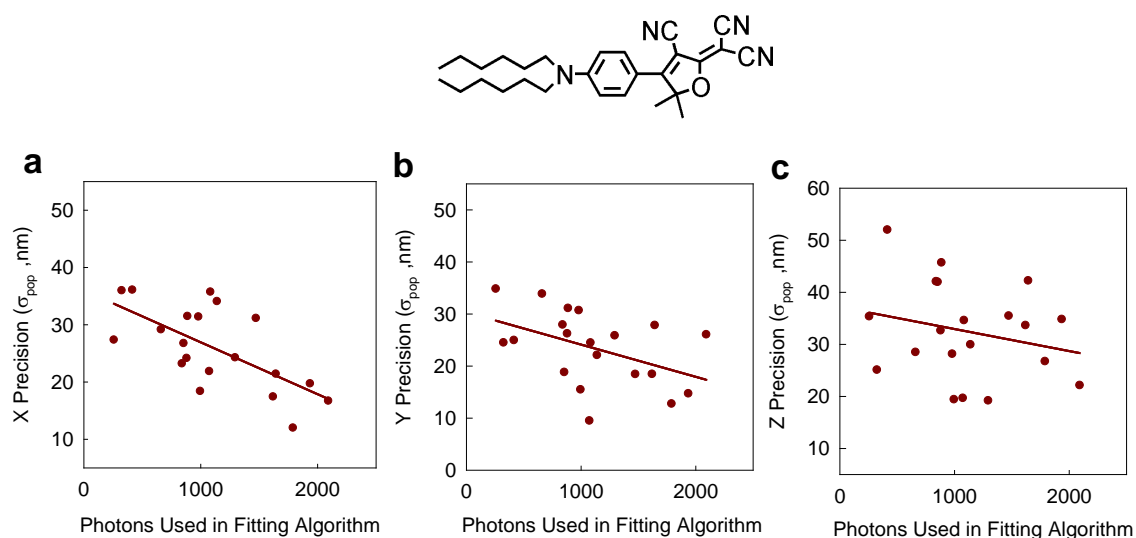
Fig. 5.6: The localization precision from single DCDHF-P (structure shown) molecules as a function of the number of photons used in the centroid estimation algorithm for the x (a), y (b), and z (c) directions. All measurements were made with acquisition times of 500 ms and the rms background noise in the samples was approximately 20 photons/pixel.

Fig. 5.6 shows three plots of the localization precision for multiple localizations of different DCDHF-P molecules versus the number of photons used in the fitting algorithm for that molecule. The ordinate of each plot refers to the localization precision as defined by the standard deviation of the population of molecule location measurements as illustrated in Fig. 5.2a, which can be regarded as the localization precision expected for a single position determination. The data in Fig. 5.6 was obtained using the computationally simpler centroid fitting scheme described in the previous section. The centroid estimation algorithm does not use all of the photons in the DH-PSF, but rather applies an adaptive threshold that only uses photons in the primary two lobes above a certain background level. This is in contrast to the fitting

algorithm used in Figure 5.2, which does not threshold the data and hence uses all available photons to find the position of the molecule. There is a weak and seemingly linear negative correlation between the localization precision and number of photons, but a full analysis of this and the development of an optimal estimation algorithm are subjects of future work. A possible reason for the scatter is that the DH-PSF shape can change slightly depending on the axial position of the emitter, that is, one lobe appears better defined than the other at certain axial positions, possibly arising from aberration effects. Another reason is that the background fluctuations from position to position are partly deterministic: because much of the background itself is actually weak, the sidelobes from the various GL modes forming the PSF combine to make a widely spatially varying, but temporally constant, variation across the sample.

5.8.4 Calibration of CCD gain for photon counting

In order to convert EMCCD camera counts to photons, two calibrations are required: the conversion gain, (number of e$^-$ after on-chip gain)/(ADC count), and the electron multiplication gain (number of e$^-$ after on-chip gain)/(number of photoelectrons) [64]. Briefly, the method proceeds as follows. First, one records two images of a dim uniform field (a blank, clean coverslip) at the same light intensity level with no EM gain for an arbitrary number of evenly spaced intensities. Due to Poisson fluctuations in detected photons, a plot of the variance of the image for each intensity level versus the mean signal of the image for each intensity level should be a straight line with a slope that equals the inverse of the conversion gain. Significant flat-field effects due

to nonuniformity in pixel sensitivity caused a nonlinear dependence and they were removed by two methods described in Ref. 64.

The electron multiplication gain on the camera needs to be calibrated because the value selected in the software does not always exactly match the true value. To calculate this factor for any software input value, we measured the ratio of the mean signal under an arbitrary irradiance and the mean signal with the camera shutter closed. Because dark counts are negligible, the electron multiplication gain is then determined by computing this ratio with the gain on divided by this ratio with the gain off (i.e., multiplicative gain=1).

5.8.5 Synthesis of photoactivatable fluorophore DCDHF-V-PF$_4$-azide

4-Azido-2,3,5,6-tetrafluorobenzaldehyde
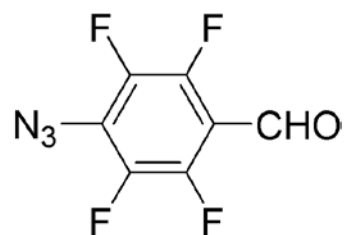
This synthesis was performed by Prof. Robert Twieg's group at Kent State University. To a 100-mL round-bottom flask with stirbar was added pentafluorobenzaldehyde (1.96 g, 0.01 mol), sodium azide (0.72 g, 0.011 mol), acetone (15 mL) and water (15 mL) [65,66,67,68]. The mixture was warmed to reflux under nitrogen for 10 h. TLC showed all the pentafluorobenzaldehyde was

consumed and so the reaction was stopped and cooled to room temperature. The product mixture was diluted with 20 mL of water. The crude product was extracted with ether (30 mL ×5). The combined organic layer was dried over anhydrous MgSO$_4$. The solvent was removed at room temperature under vacuum. Sublimation of the residue (50 ºC/0.2 mm) gave the final product as a white solid (1.20 g, 55% yield). Mp 44 ºC (lit 44–45 ºC, ref (5)). IR (neat): 3377, 2121, 1704, 1644, 1480, 1398, 1237, 1066, 1000, 615 cm^{-1}. ^{1}H NMR (400 MHz, CDCl$_3$): δ 10.26 (m, 1H); ^{19}F NMR (470 MHz, CDCl$_3$): δ –149.6 (m, 2F), –155.6 (m, 2F).
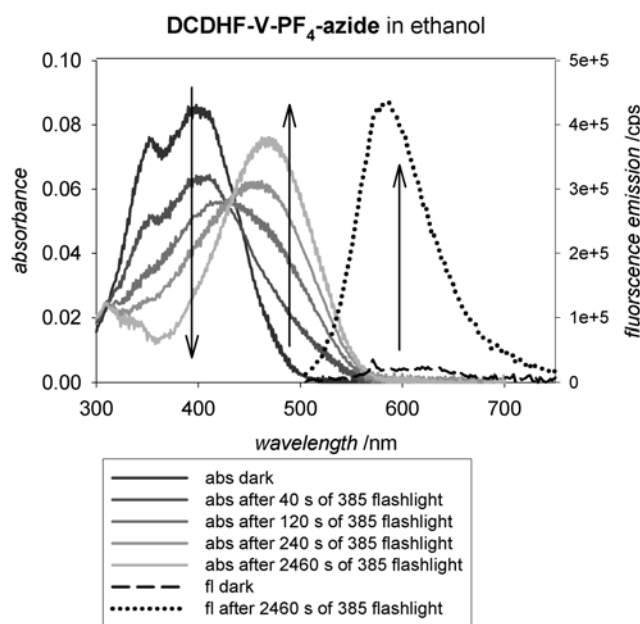
Fig. 5.7: Absorption (solid lines) and fluorescence (dashed and dotted lines) spectra of the DCDHF-V-PF4-azide dark fluorogen before and after photoactivation to the amino fluorophore. The short-wavelength absorption peak, which corresponds to the azido fluorogen, disappears after illumination with 385-nm light (0.3 mW/cm^2); the longer wavelength peak of the fluorescent amino compound grows in. Before photoactivation, pumping at 490 nm yields little fluorescence (dashed line); after activation with 385-nm illumination, pumping at 490 nm produces much brighter fluorescence (dotted line).

(*E*)-2-(4-(4-Azido-2,3,5,6-tetrafluorostyryl)-3-cyano-5,5-dimethylfuran-2(5*H*)-ylidene)malononitrile (DCDHF-V-PF$_4$-azide)
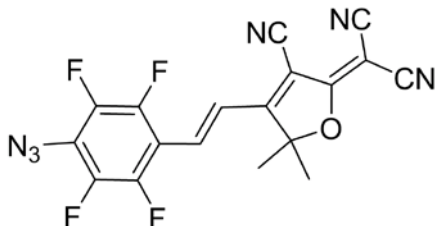
This synthesis was also performed by Prof. Robert Twieg's group at Kent State University. To a 100-mL round-bottom flask with stirbar was added 4-azido-2,3,5,6-tetrafluoro-benzaldehyde (0.22 g, 1 mmol) and 2-(3-cyano-4,5,5-trimethyl-5*H*-furan-2-ylidene)-malononitrile (0.22 g, 1.1 mmol), 5 mL pyridine and several drops of acetic acid. The mixture was stirred at room temperature for 2.5 days. TLC showed the desired azido product had been formed as the main product. The reaction was stopped and poured into 500 mL ice-water. After stirring for 2 h, the precipitate was filtered off by suction filtration. The solid was recrystallized from 1-propanol. After recrystallization, part of the azido product was converted to the corresponding amino compound. The mixture was adsorbed on silica gel, placed at the top of a silica column and eluted (CH$_2$Cl$_2$:EtOAc = 20:1). Fractions containing only the first product were combined and concentrated to give an orange product (40 mg, 10% yield). This is the final azido product, (*E*)-2-(4-(4-azido-2,3,5,6-tetrafluorostyryl)-3-cyano-5,5-dimethylfuran-2(5*H*)-ylidene)malononitrile. Recrystallization could not be done on this compound, since it has high photoreactivity: it readily converts to the corresponding amino compound in solvents (like propanol) in daylight. IR (neat): 2933, 2228, 2124, 1586, 1557, 1489, 1372, 1253, 998 cm^{-1}. ^{1}H NMR (400 MHz,

CDCl$_3$): δ 7.63 (d, J = 16.8 Hz, 1H), 7.31 (d, J = 16.4 Hz, 1H), 1.82 (s, 6H); ^{13}C

NMR (100 MHz, CDCl$_3$): δ 174.5, 172.5, 146.9 (m), 144.4 (m), 142.0 (m), 139.4 (m),

130.7, 121.4 (t, J = 9.8 Hz), 111.1, 110.3, 109.5, 102.6, 97.8, 51.3, 26.3; ^{19}F NMR

(470 MHz, CDCl$_3$): δ –143.5 (2F), –155.2 (2F). UV–vis (EtOH): λ_{max} = 406 nm, ε =

2.7 x 10^4 L mol^{-1} cm^{-1}.

Chapter 6

Polarization Sensitive 3D Nanoscopy of Cells

Double-helix point-spread function photoactivation-localization microscopy allows three-dimensional (3D) super-resolution imaging of objects smaller than the optical diffraction-limit. We demonstrate polarization sensitive detection with 3D super-localization of single-molecules and unveil 3D polarization specific characteristics of single-molecules within the intracellular structure of PtK1 cells expressing photoactivatable green fluorescent protein. The system modulates orthogonal polarizations of single-molecule emissions with a single spatial light modulator, yielding up to 30% 3D precision improvement using an optimal estimation rule.

6.1   Introduction

A variety of super-resolution microscopy methods are now making it possible to resolve objects that are smaller than the optical diffraction limit, which has historically restricted spatial resolutions to about ~200nm in the transverse (x,y) dimensions. Prominent among these are stimulated emission and depletion (STED) microscopy [1], structured illumination microscopy (SIM) [2], photoactivated localization microscopy (PALM) [3], stochastic optical reconstruction microscopy (STORM) [4], and fluorescence photoactivation localization microscopy (FPALM) [5]. PALM, STORM, and FPALM photoactivate (turn on) a sparse subset of fluorescent molecules at a given time, and localize the molecule positions with

precisions much better than the diffraction limit. Super-resolution images are obtained by repeatedly photoactivating and localizing different sparse molecule subsets at different times, and by combining the position information of all photoactivated molecules. This has been extended to the third dimension by using astigmatism [9], biplane detection [10], two-photon processes [11], interferometry [12], and a double-helix point spread function [69] (Chapter 5 of this thesis).

The DH-PSF based 3D super-resolution technique uses a phase mask [35] in a microscope's imaging path to engineer the point spread function of the microscope to exhibit two lobes that rotate with defocus. Accordingly, each molecule displays two lobes in the image plane, with the angular orientation of the lobes encoding the axial position of the molecule, and their midpoint representing the molecule transverse position [49]. Because the DH-PSF carries higher Fisher Information about a molecule's 3D position than a standard PSF (clear aperture) over a long range, DH-PSF microscopes can localize molecules with fundamentally better 3D precision than standard systems [48].

In single-molecule super-resolution imaging, it is useful to obtain information on the orientation of molecules by analyzing the polarization of their emissions, in addition to their spatial positions. Because the orientations of protein molecules are directly related to the orientations of intracellular structures, polarization sensitive super-resolution imaging offers super-resolution images with a molecule-orientation based contrast, besides the contrast based on the brightness and the concentration of single molecules. Polarization-FPALM demonstrates this capability in two dimensions by simultaneously detecting the transverse (x,y) positions and

polarization anisotropy of molecules [70]. Information on molecule orientations have also been determined by other methods [71,72,73,74,75], but have not been used in super-resolution imaging.

In this chapter, we present a polarization sensitive DH-PSF super-resolution system and demonstrate the first 3D nanoscale imaging of polarization-specific characteristics of single photoactivatable green fluorescent protein (PA-GFP) [76] molecules in a cell [77]. The system modulates the phase of two orthogonal polarization channels with a single spatial light modulator, and detects polarization-specific DH-PSF images with a single detector. With a single objective lens, the 3D positions of the fluorescent protein molecules are localized with about 20nm and 40nm precisions in the transverse and axial dimensions with only ~250 detected photons per image. We further show that improved 3D localization precisions can be achieved by optimally combining the information from the two polarization channels.

6.2   Polarization sensitive double-helix nanoscope

Fig. 6.1 illustrates the polarization-sensitive 3D super-resolution experimental setup. The imaging path includes a microscope section and a polarization-sensitive signal processing section. In the microscope section, a 1.3NA objective (Lo) and an achromatic lens (Lt) form a 91x magnified intermediate image of the sample. A diaphragm (iris) is placed on this plane to adjust the field of view of the system. The polarization-sensitive signal processing section consists of two parallel 4f imaging systems — one for each of the horizontal and vertical polarizations.
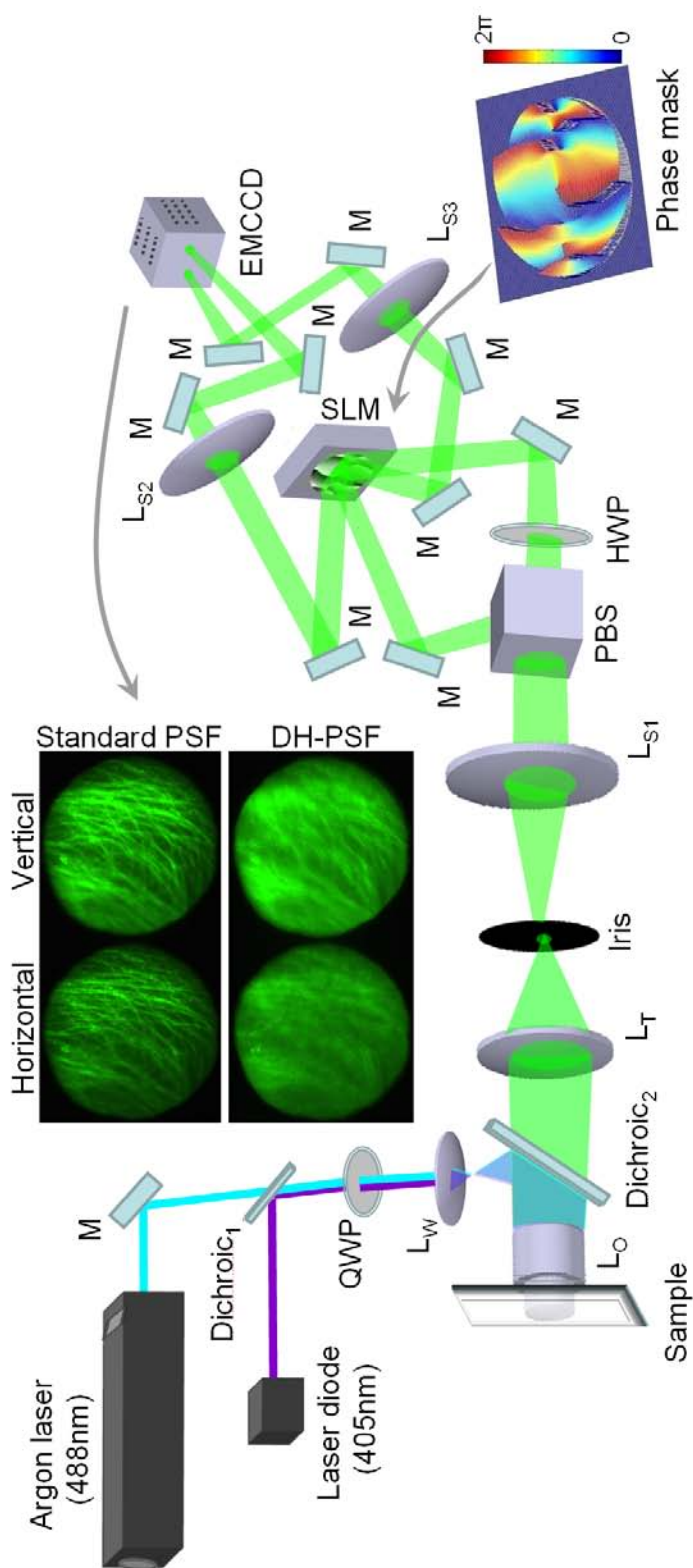
Figure 6.1. Experimental setup for polarization sensitive 3D superresolution imaging with the double-helix point spread function (DH-PSF). PtK1 cells labeled with PA-GFP are excited with the 488nm argon laser line and are photoactivated with a 405nm laser diode. The imaging path consists of two polarization channels that are modulated with a spatial light modulator (SLM) encoding the DH-PSF phase mask (bottom right inset). The inset in the middle shows PtK1 microtubules imaged in the horizontal and vertical channels with the standard PSF (SLM off) and with the DH-PSF (SLM loaded with DH-PSF mask). M refers to mirrors; QWP is quarter wave plate; L_W is a wide-field lens; L_O is a 1.3NA objective; L_T is a 150mm achromatic lens; L_{S1}, L_{S2}, and L_{S3} are 250mm achromatic lenses; PBS is a broadband polarization beam splitter; HWP is a broadband half wave plate; EMCCD is an electron multiplying charge coupled device detector.

A broadband polarization beam splitter (PBS) creates the two polarization channels after propagation through the Fourier transform lens L_{S1}. A spatial light modulator is placed in the Fourier plane shared by the two polarization channels. Because the SLM is sensitive only to vertically polarized light, a broadband half-wave plate is used to rotate the polarization of the horizontal channel by 90°. The PSFs of the two channels are engineered by loading the SLM with the DH-PSF phase mask (bottom right inset in Fig. 6.1). The final stage of the 4f systems is implemented by two achromatic lenses (L_{S2} and L_{S3}) that create two polarization-specific DH-PSF images on different regions of an electron multiplying CCD detector.

The illumination side of the system consists of a circularly polarized 488nm Argon laser beam (for the excitation of PA-GFP molecules) and a 405nm laser diode beam (for the photoactivation of PA-GFP molecules). These beams are expanded sufficiently by a wide-field lens (L_W; focal length = 75mm) to illuminate the entire field of view (40μm diameter) of the system. While the Dichroic$_1$ transmits over 95% of the 488nm beam and reflects over 90% of the 405nm beam, the Dichroic$_2$ and a band-pass filter combination in the imaging path block the excitation wavelengths and transmit about 90% of the PA-GFP emission spectra (505nm to 590nm).

The center inset in Fig. 6.1 shows the result of imaging PA-GFP labeled microtubules of a PtK1 cell using standard PSF (SLM off) and DH-PSF (SLM loaded with DH-PSF mask), with horizontal and vertical polarization channel images in each case. In the standard PSF image, the microtubules near the focal region of the objective appear sharply focused (because the standard PSF is narrow in this region), and the microtubules outside the focal region appear blurred (because the standard

PSF widens significantly for out-of-focus objects). In contrast, in the DH-PSF image, each axial (z) slice of the object is convolved with the two DH-PSF lobes, which are oriented at an angle that is uniquely related to the axial position of the object slice. While 3D information can be retrieved from such DH-PSF images of continuous objects using deconvolution techniques [22], in the context of PALM/STORM/FPALM based super-resolution imaging, because only sparse subsets of molecules are turned on at any given time, each molecule directly displays two DH-PSF lobes in the image.

Fig. 6.2 shows an example of imaging a 40nm wide fluorescent bead (Excitation peak: 505nm; Emission peak: 515nm) when the SLM is loaded with the DH-PSF phase mask. Because the bead acts like a point source, the images of the bead mimic the 3D DH-PSF, with two lobes continuously rotating as the bead is moved in the axial dimension. Interestingly, because of the presence of an additional mirror between the SLM and the second signal processing lens (L_{S3}) in the vertical channel, the two channels see horizontally flipped versions of the DH-PSF mask, resulting in opposite DH-PSF rotation directions. However, because the total number of reflections in both channels is of the same parity, the images produced by the two channels are not flipped with respect to each other (See Fig. 6.1 center inset). Fig. 6.2 shows the calibration curves for mapping rotation angles to axial locations in both polarization channels (See section 6.7 for calibration details).
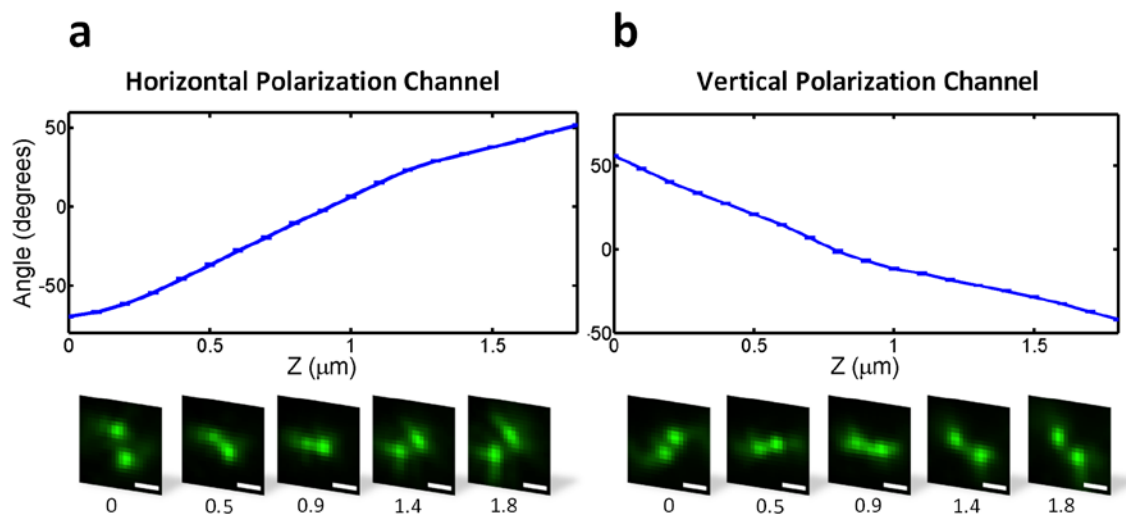
Figure 6.2. Plots of DH-PSF rotation angle in the (a) horizontal and the (b) vertical channels obtained by moving a 40nm wide fluorescent microsphere in the axial dimension with 100nm steps. The DH-PSF rotates in opposite direction in the two channels. Scale bar: 1μm

6.3 Precision improvement by combining channels

When the sample under observation has multiple sparse point sources (molecules, beads) at different 3D locations, the DH-PSF images of the two channels exhibit two differently rotated lobes for every source. The transverse position of each source is estimated from the midpoint of the two lobes, and the axial position is estimated by converting rotation angles to axial locations using the calibration plots of Fig. 6.2.

The precision with which the 3D position of a point source can be estimated primarily depends on the number of photons emitted by the source, PSF shape, detector noise, image background, and the position estimation algorithm. Because of the splitting of photons into two polarization channels, the 3D position localization precisions of each channel, in general, is worse than that of a single channel system (such as a polarization insensitive super-resolution system). Interestingly, better

precisions than the precisions of the individual polarization channels — even matching the precision of a single-channel system — can be achieved by properly combining the information from the two channels. From an information theoretical perspective, this improved precision is the result of the addition of the Fisher Information from the two channels. While such improvements can be achieved with complex estimators that simultaneously fit the PSFs of the two channels, we now show that equally improved precisions can be achieved by *optimally* combining the information with simple estimators that operate on each of the two channels separately. In a shot-noise limited system, we further show that the improved precisions achieved by this optimal combination are identical to the precisions that would have been obtained if all photons were detected in a single channel system.

We estimate the 3D positions of the two channels separately, and combine them as a weighted average with optimal weights, as shown below.

$$P_C = \alpha P_H + \beta P_V , \tag{6.1}$$

where P_H, P_V, and P_C refer to the position estimates in the horizontal channel, vertical channel, and in the channel combination along a particular spatial dimension (X, Y, or Z) with standard deviations σ_H, σ_V, and σ_C, respectively. α and β represent the scaling factors whose optimal values are found to be (See Section 6.7 for details):

$$\alpha = \frac{\sigma_V^2}{\sigma_H^2 + \sigma_V^2} \; ; \; \beta = \frac{\sigma_H^2}{\sigma_H^2 + \sigma_V^2} , \tag{6.2}$$

With an uncorrelated pixel assumption, we quantify the improvement in precision with the variable *precision gain* (PG) defined as,

$$PG \; = \; min(\sigma_H, \sigma_V) - \sigma_C \; = \; min(\sigma_H, \sigma_V) - \sqrt{\alpha^2 \sigma_H{}^2 + \beta^2 \sigma_V{}^2} \; . \qquad (6.3)$$

Fig. 6.3a shows PG as a function of the precisions of the horizontal and vertical channels. By choosing α and β optimally, we achieve improved precisions (*PG* > 0) for all values of σ_H and σ_V with improvements up to about 30%.
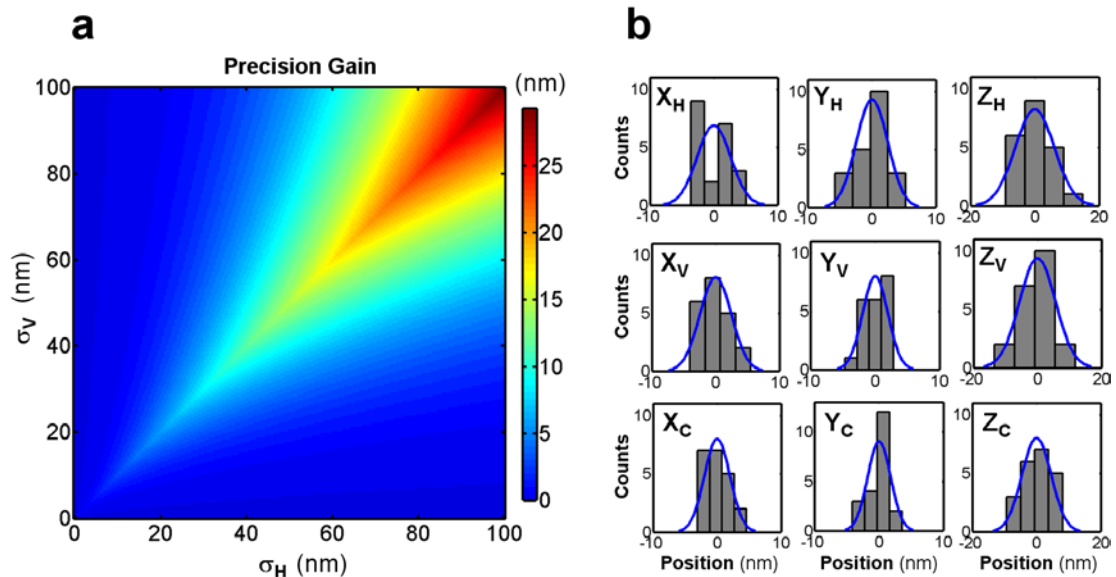
Figure 6.3. (a) Gain in position localization precision obtained by combining position information from the two polarization channels. The image shows that the optimal channel combination technique presented here always results in an improvement in localization precision. (b) 3D position histograms of a fluorescent bead showing improved precisions when horizontal (X_H, Y_H, Z_H) and the vertical (X_V, Y_V, Z_V) channel estimates are combined (X_C, Y_C, Z_C). $\sigma_H(X,Y,Z) = (2.6, 2.5, 6.1)nm$; $\sigma_V(X,Y,Z) = (2.5, 2, 5.6)nm$; $\sigma_C(X,Y,Z) = (2, 1.8, 4.5)nm$. This experimentally demonstrates the precision improvement by optimally combining the information from the two channels.

It is worth noting that suboptimal selection of weights would result in precision improvements only within smaller regions of Fig. 6.3a. Interestingly, in a shot-noise limited system, the precision improvement with optimal weights makes the precision (σ_C) of the optimally combined estimate (P_C) identical to the precision (σ_S) of a single channel system, where all photons from a molecule are imaged in one channel. Specifically,

$$\sigma_C = \sigma_S = \frac{\sigma_H \, \sigma_V}{\sqrt{\sigma_H{}^2 + \sigma_V{}^2}} \; . \tag{6.4}$$

Further, when $\sigma_H{}^2$ and $\sigma_V{}^2$ reach the Cramer-Rao Bounds (lowest possible variances with unbiased estimators) of the two channels, σ_C is exactly equal to the precision obtained when the Fisher Information from the two channels are added (See Section 6.7 for details).

Fig. 6.3b shows position localization histograms obtained from 21 position estimates of a fluorescent bead. (X_H, Y_H, Z_H), (X_V, Y_V, Z_V), and (X_C, Y_C, Z_C) correspond to the 3D position estimates obtained from the horizontal channel, the vertical channel, and the channel combination, respectively. While the single-image standard deviations of the horizontal and the vertical channels are $\sigma_H(X,Y,Z)=(2.6nm, 2.5nm, 6.1nm)$ and $\sigma_V(X,Y,Z)=(2.5nm, 2nm, 5.6nm)$, the standard deviations of the optimal channel combination are $\sigma_C(X,Y,Z)=(2nm, 1.8nm, 4.5nm)$. In this experiment, 41,014 photons were detected per estimate from the horizontal channel, and 65,852 photons were detected

per estimate from the vertical channel. The channel combination results demonstrate an improvement in precision over the precisions of the individual channels. As a corollary, it is worth noting that σ_H and σ_V can be directly translated into molecule polarization orientations. However, while using high NA objectives, care needs to be taken to account for polarization distortion effects which require rigorous vectorial electromagnetic modeling.

6.4   Imaging of PA-GFP molecules

We now describe imaging of PA-GFP molecules in a PtK1 rat kangaroo kidney epithelial cell. The molecules are excited with the 488nm laser, and are photoactivated with the 405nm laser. Fig. 6.4 shows an example of a PA-GFP molecule obtained from the horizontal channel of our system. The molecule position was localized from 19 images to obtain the 3D position histograms shown in Fig. 6.4(b,c,d). On an average, these position estimates were computed from only 246 detected photons per image, resulting in single image standard deviations of $\sigma_{PA-GFP}(X,Y,Z)=(13.2nm,\ 20.3nm,42.8nm)$.
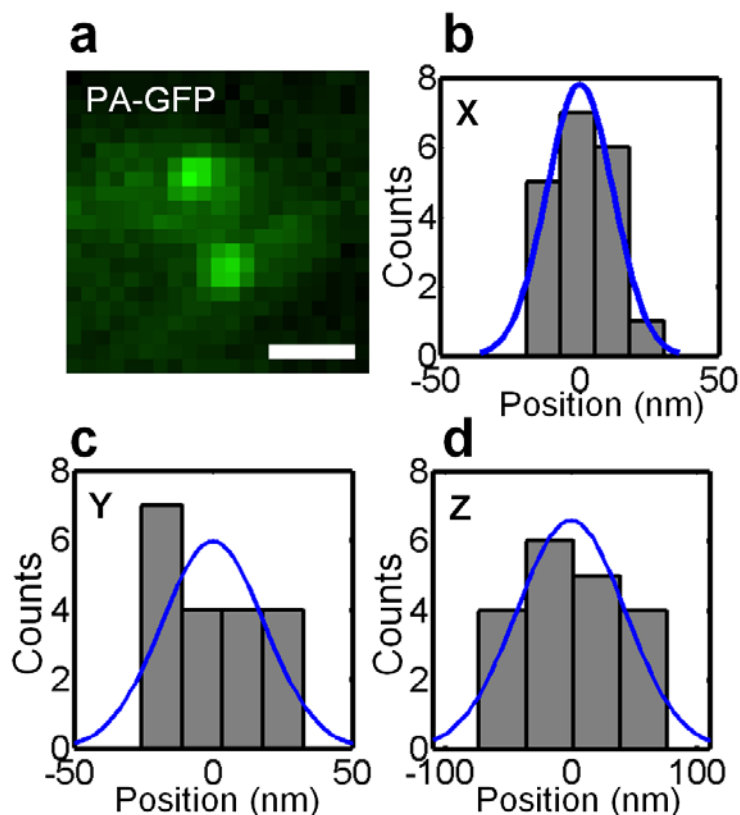
Figure 6.4. Position localization histograms of a (a) single PA-GFP molecule in the (b) X, (c) Y, and (d) Z dimensions. $\sigma_{PA-GFP}(X,Y,Z)=(13.2nm, 20.3nm, 42.8nm)$. The average number of detected photons per image is only 246 photons. Scale bar: 1μm

6.5   3D polarization sensitive super-resolution results

For polarization-sensitive 3D super-resolution imaging, we initially bleached the PA-GFP molecules within the field of view using the 488nm laser, and later activated sparse subsets of PA-GFP molecules by shining the 405nm laser on the sample. By repeating this activation cycle a number of times, different sparse PA-GFP molecules were photoactivated, while their 3D positions were estimated from the horizontal and the vertical channels of the system. The 3D super-resolution images in Fig. 6.5 were

obtained by combining the positions of molecules from a number of activation cycles after correcting for stage drift and other systematic errors (See Section 6.7).

The PtK1 cells appear differently in the horizontal and the vertical polarization channel images. For example, the edge of the cell (dotted cyan arrows) is more prominently visible in the horizontal polarization channel than in the vertical polarization channel (see XY projection images). This difference is due to molecules appearing with different intensities in the two channels based on their orientations. The XZ and YZ projections of the 3D super-resolution images show this polarization based difference. These axial images also show the existence of layers of cells extending in depth. Such polarization-specific 3D super-resolution images of cells offer biologists a new way to analyze intracellular structure and function.

Standard bright field microscopy analysis of the sample using cross-polarizers showed essentially no sample birefringence (See section 6.7). Accordingly, the polarization information provided by the system can be associated with the molecular orientation and propagation through the optical system.

It is important to note that the polarization specific DH-PSF super-resolution system described here detects only the first two (S_0, S_1) of the four Stokes vectors [78] (S_0, S_1, S_2, S_3) corresponding to an arbitrary transverse-plane polarization state. In order to determine the transverse-plane orientation of an arbitrary linear polarization state, S_2 needs to be measured in addition to S_0 and S_1. This can, for example, be done by decomposing the incoming polarization into two additional $+45°$ and $-45°$ channels. Determining the orientations of molecules is further complicated by
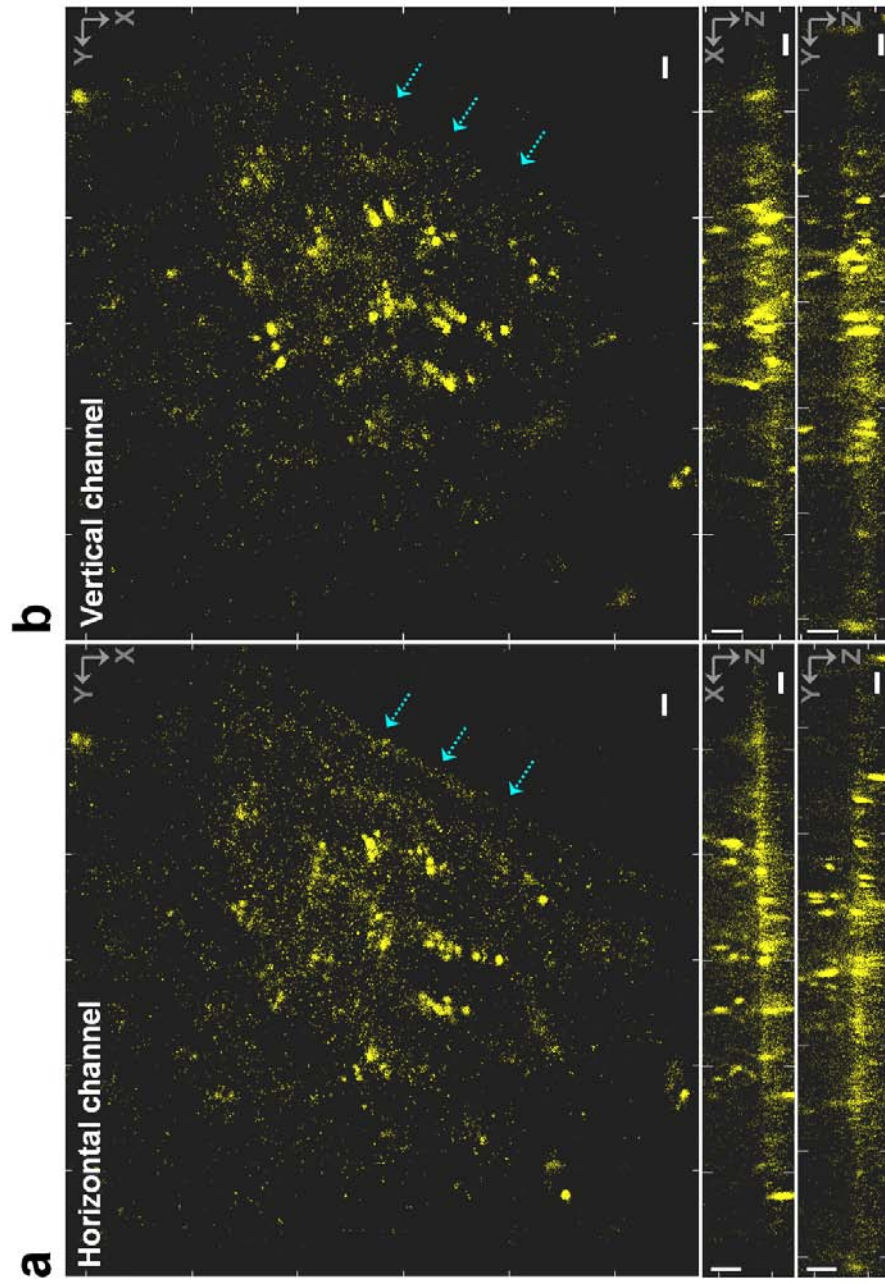
Figure 6.5. Polarization specific 3D superresolution images of a PtK1 cell obtained from (a) horizontal and (b) vertical polarization channels. The superresolution images from the two channels reveal polarization specific features of the cell. For example, the edge of the cell (pointed at by cyan dotted arrows) is more prominently visible in the horizontal polarization channel, but not in the vertical polarization channel. Scale bars: 1μm

polarization distortion effects because of high NA objectives, which require corrections based on rigorous vectorial modeling.

A liquid-crystal SLM based implementation of the DH-PSF offers the convenience of rapidly implementing different DH-PSF masks suitable for application-specific requirements with high sampling rates and fill factors, but unfortunately comes with the need to absorb the polarization component orthogonal to the polarization component for which the SLM is designed to operate. The polarization sensitive DH-PSF implementation described here, on the other hand, takes advantage of photons emitted in both polarization states to improve localization precision and consequently imaging resolution, while simultaneously having the ability to resolve polarization specific nanometer scale features in three dimensions.

In photoactivation-localization techniques, the factors contributing to contrast are the density of molecule position estimates and the number of photons detected for each position estimate. An attractive aspect of the technique presented here is the existence of an additional contrast mechanism based on polarization. In other words, polarization information can reveal structural and functional properties that might go undetected in polarization insensitive techniques.

Polarization sensitive detection of single molecules using the DH-PSF provides information from both the 3D position and the orientation of individual proteins within a cell or sub-cellular structure. Applications for this technique are biologically far-reaching, with use in tracking orientation changes of molecules within a cellular structure, as well as in monitoring interactions between molecules. For example, solving the orientation of proteins within large subcelluar structures, such as

centrosomes or kinetochores, would provide important information on how protein-protein interactions occur within these structures, and on how signals are exchanged between these structures and the cytoplasm of the cell. Further, polarization sensitive super-resolution imaging of individual cytoskeletal subunits (i.e. actin, tubulin) can potentially be used to detect with high precision the binding of proteins to actin or microtubule filaments. Understanding the precise location and orientation of protein binding to these filaments would provide much needed insight into a number of critical cellular processes including chromosome segregation, cell motility, neurite outgrowth, and vesicle trafficking.

6.6   Summary

In summary, we have demonstrated a polarization sensitive 3D super-resolution imaging system that engineers the PSFs of two orthogonal polarization channels with a single SLM and detects both channels separately with a single detector. By combining the position information from the two imaging channels with simple estimators, we demonstrated improvements in 3D position localization precisions. We finally used our system to obtain polarization specific 3D super-resolution images of PtK1 cells expressing PA-GFP.

6.7 Appendix: Optimal position estimation, calibration, and imaging

Derivation of optimal weights for weighted channel combination

Assuming uncorrelated pixels, the standard deviation of the weighted average channel combination defined in equation (6.1) of main text is,

$$\sigma_C = \sqrt{\alpha^2 \sigma_H^2 + (1-\alpha)^2 \sigma_V^2} \; , \tag{6.A1}$$

where the weight condition, $\alpha + \beta = 1$, has been used to express β in terms of α. Optimal weights are defined as the weights that minimize σ_C. Applying the minimization condition by equating the first derivative (with respect to α) of equation (6.A1) to 0,

$$\frac{\partial \sigma_c}{\partial \alpha} = \frac{2\alpha \sigma_H^2 - 2(1-\alpha)\sigma_V^2}{2\sqrt{\alpha^2 \sigma_H^2 + (1-\alpha)^2 \sigma_V^2}} = 0 \; . \tag{6.A2}$$

Solving for α leads to

$$\alpha = \frac{\sigma_V^2}{\sigma_H^2 + \sigma_V^2} \; ; \quad \beta = \frac{\sigma_H^2}{\sigma_H^2 + \sigma_V^2} \tag{6.A3}$$

The second derivative (with respect to α) of equation (6.A1) is positive, confirming that σ_C attains its minima when the weights are as defined in equation (6.A3). Using (6.A3) in (6.A1), the standard deviation of the channel combination becomes,

$$\sigma_C = \frac{\sigma_H \sigma_V}{\sqrt{\sigma_H^2 + \sigma_V^2}} \; . \tag{6.A4}$$

Equality of the precision of the optimal channel combination (σ_C) and the precision of single-channel systems (σ_S).

In a shot noise limited system, if N is the number of photons captured by an imaging system from a molecule, σ_S is the standard deviation if all N photons are imaged in one channel, and κ is the fraction of photons entering the horizontal polarization channel, the standard deviations corresponding to horizontal (σ_H) and vertical (σ_V) polarization channels are,

$$\sigma_H = \frac{\sigma_S}{\sqrt{\kappa}} ; \quad \sigma_V = \frac{\sigma_S}{\sqrt{1-\kappa}} \ .$$

(6.A5)

From equation (6.A5),

$$\sigma_S = \sigma_V \sqrt{1-\kappa} = \sigma_V \sqrt{1 - \frac{\sigma_S^2}{\sigma_H^2}} \ .$$

(6.A6)

Solving for σ_S,

$$\sigma_S = \frac{\sigma_H \, \sigma_V}{\sqrt{\sigma_H^2 + \sigma_V^2}} \ .$$

(6.A7)

Note that from equations (6.A4) and (6.A7), σ_C and σ_S are identical. This means that (in the shot-noise limited case) the precision achieved by optimally combining channels is exactly the same as the precision of a single-channel system, where all photons from a molecule are imaged in one channel.

In summary, the weighted combination method of equation (6.1), when used with the optimal weights of equation (6.A3) is found to be a powerful, yet simple, method that achieves precisions that are equivalent to the precisions of a system that detects all photons in a single channel.

Equality of the Cramer Rao Bound (CRB) of the optimal channel combination

(CRB_C) and the CRB of a two-channel (CRB_T) system

CRB is a quantitative information theoretical metric that provides a lower bound on estimator variances when unbiased estimations are used. We now show that the CRB of the optimal channel combination (CRB_C) is identical to the CRB of the two channel system (CRB_T) and to the CRB of a single-channel system (CRB_S) that captures all the photons.

Using Eq (6.A4) and taking the lower bound on both sides of the equation, we obtain the CRB corresponding to the optimal weighted average rule:

$$CRB_C = \frac{CRB_H \ CRB_V}{CRB_H + CRB_V} \tag{6.A8}$$

where CRB_H, CRB_V are the lower bounds of the horizontal ($\sigma_H{}^2$) and vertical ($\sigma_V{}^2$) channel variances, respectively.

The total information content in a two channel system is given by the sum of the Fisher Information from individual channels ($F_H \equiv \frac{1}{CRB_H}$ and $F_V \equiv \frac{1}{CRB_V}$). Hence, the CRB for the two channel system is

$$CRB_T = \frac{1}{F_H + F_V} = \frac{CRB_H \ CRB_V}{CRB_H + CRB_V}. \tag{6.A9}$$

From equations (6.A8) and (6.A9), we see that $CRB_C = CRB_T$. Similarly, by applying lower bounds on equation (6.A7), it follows that $CRB_C = CRB_S$.

The fact that CRB_C is identical to CRB_T suggests that estimators acting separately on each of the two channels can be as good as the (more complex) estimators that operate simultaneously on the two channels.

Rotation angle calibration

The data for the plots in Fig. 6.2 of the main text were obtained by translating a 40nm wide fluorescent microsphere (Invitrogen yellow-green carboxylate-modifed FluoSpheres®) in 100nm axial steps using a piezo stage (Physik Instrumente P-615.3CD), and by estimating the DH-PSF rotation angle from 21 images acquired with 273ms exposure time with a detector cooled to -90°C. These fluorescent microspheres have an emission spectrum that is very close to that of PA-GFP. The 488nm excitation power was 1.3mW. DH-PSF rotation angles were estimated as the angle between the centroids of the two DH-PSF lobes. The angle estimator's standard deviations at each axial step are shown as an error bar (at each axial step) in Fig. 6.2.
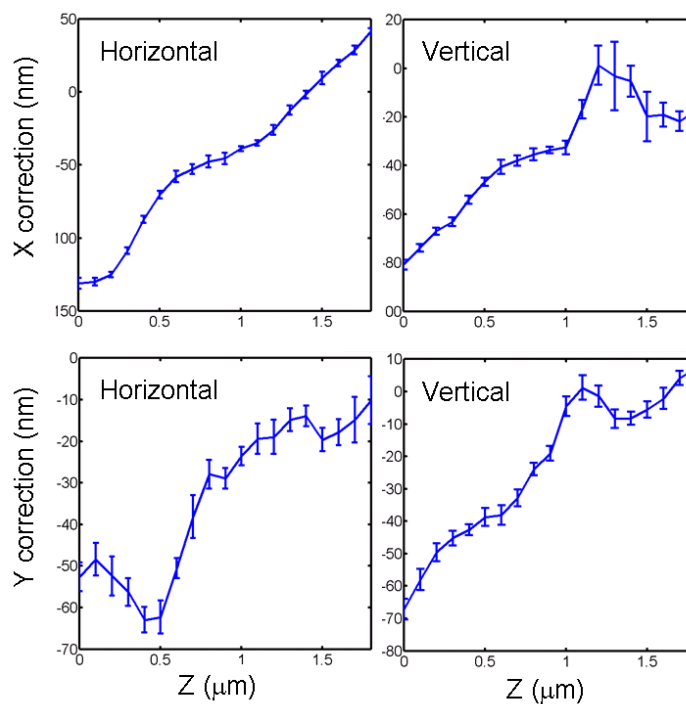
Figure 6.6. X and Y corrections of the horizontal and the vertical channels due to aberration induced small systematic shift in the midpoint of the two PSF lobes.

Transverse position corrections

Because of aberrations, the position of the midpoint of the two DH-PSF lobes shifts with axial distance. This systematic shift is calibrated by plotting the transverse position of the midpoint as a function of axial distance (Fig. 6.6). Actual 3D position information of a point source is reported after correcting for these systematic errors.

Super-resolution imaging

The 405nm diode laser (0.5mW power) was controlled with a function generator to turn on for 500ms once in every 5 seconds. The 488nm Argon laser (38mW power) was always on during the imaging process. The laser beams illuminated the sample

with circular polarization to excite or photoactivate molecules with all transverse-plane orientations. A broadband (420-680nm, Edmund Optics) polarizing beam splitter and an achromatic (465-610nm, Edmund Optics) half wave plate were used in the imaging path to account for the PA-GFP emission bandwidth. Images were detected with 500ms exposure time using an electron multiplying charge coupled device (EMCCD) detector (Andor iXon) cooled to -90°C. Fig. 6.5 is obtained from a dataset collected for 3.7 hours, after correcting for stage drift with a fiduciary object.

Sample preparation

This sample was prepared by Prof. Jennifer G. DeLuca's group at Colorado State University. PtK1 cells stably expressing PA-GFP-tubulin were maintained in HAM's F-12 medium complemented with 0.5 mg/ml G418, 10% fetal bovine serum, penicillin, streptomycin, and amphotericin B (antimycotic) and plated on number 1½, 22mm2 glass coverslips in 6-well culture dishes in a 37°C, 5% CO2 humidified incubator. Cells on coverslips were lysed in 0.5% Triton X-100 in PHEM buffer (60 mM PIPES, 25 mM HEPES, 10 mM EGTA, and 4 mM MgSO4, pH 6.9) at 37°C for 5 min and fixed in freshly prepared 4% formaldehyde in PHEM buffer at 37°C for 20 min. Coverslips were rinsed three times for 5 min in PHEM, mounted onto slides, and sealed.

Check for sample birefringence

A differential interference contrast (DIC) image of the PtK1 cells is shown in Fig. 6.7(a) and an image of the same region with cross-polarizers shows there is negligible birefringence [Fig. 6.7(b)].
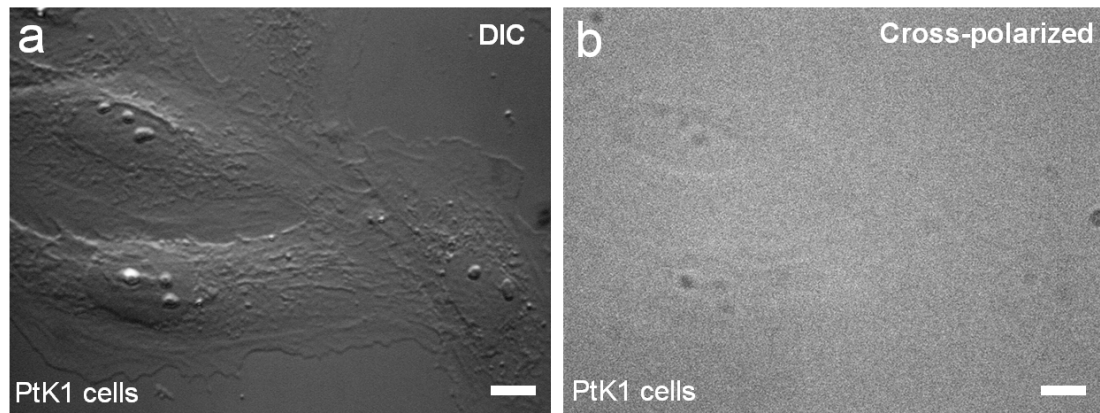
Fig. 6.7. (a) Differential Interference Contrast (DIC) image of PtK1 cells, (b) Cross-polarized image of the same cells as in (a) showing negligible birefringence. Scale bars: 10μm

Chapter 7

Future work

7.1   Approaching the fundamental limits of 3D DH-PSF nanoscopy

The DH-PSF nanoscope has broken the optical diffraction limit over one order of magnitude in all three dimensions — Chapters 2, 3, and 4 of this thesis enabled Chapter 5 to resolve molecules separated by about 20nm in each of the three spatial dimensions; Chapter 6 already reveals polarization-specific nanoscale features in cells. A natural question to ask is whether there is a fundamental resolution limit to the 3D DH-PSF nanoscopy introduced here?

The resolution of a DH-PSF nanoscope is fundamentally limited by the precision with which single molecules are localized. Each point (molecule position) in our super-resolution images has a position uncertainty cloud with radius about twice the standard deviation (precision) of position estimation. As these clouds become wider, the clouds of neighboring points begin to overlap, thereby degrading resolvability. These clouds can indeed be thought of as cloud spread functions (CSFs) that are convolved with molecule positions of super-resolution images. However, unlike PSFs, CSFs are space-variant, with the size of each CSF being closely related to the brightness of its molecule and several other parameters as described below. As a corollary, it is interesting to note that when CSF sizes approach the PSF size of a standard imaging system, the system loses its super-resolution capability. With significantly better 3D Fisher Information than standard systems, the DH-PSF

nanoscope seeks the opposite – CSF sizes (consequently, localization precision) that are orders of magnitude smaller than the standard PSF.

While the localization precision of a DH-PSF system is fundamentally limited only by the number of photons (photon noise) and the estimation algorithm used, in practice it is also significantly affected by detector noise (read noise, electron multiplication noise), aberrations, background noise in images, and random stage vibrations (see section 7.2 for more information on experimental factors influencing the localization precision). The need for brighter molecules, detectors with lower electron multiplying and read noise, fewer sample-induced aberrations, samples with lower background impurities, PSF implementation with lower background, lower vibrations, active drift correction (for example, with quadrant photodiodes), and better estimation algorithms with variances reaching the CRB is thus apparent to achieve 3D resolutions better than 20nm.

Even though precision dictates the resolution capability of a DH-PSF nanoscope, it is important to note that density of photoactivatable fluorophores is critical in imaging nanometer scale features. Because these fluorophores act as sampling points in super-resolution images, identifying nanoscale structures requires multiple fluorophores on those structures. From a biological standpoint, the fluorophore concentration is limited by the biological feature under investigation, and also by the problem of large fluorophore concentrations affecting the normal functioning of cells. Furthermore, very closely spaced fluorophores are known to quench each other's fluorescence emission.

7.2   Factors influencing the Cramer-Rao Bound

Chapters 3 and 4 of this thesis used the Cramer-Rao Bound (CRB) metric to compare the performance of double-helix and standard PSFs for localizing the 3D position of a particle. As mentioned in those chapters, the fundamental parameters affecting the CRB of a PSF along a particular dimension are the gradient of the PSF, and the signal to noise. Specifically, the CRB decreases (better localization performance) as each of those two factors increase.

In an experimental setting, it is important to understand that there are a number of parameters that influence the precision of the estimation. Notable among these are detector parameters (such as thermal, read, electron-multiplication, and shot noise, dark current, pixel size, bit depth, position of PSF in detector array [38]), sample parameters (such as number of photons emitted or scattered by the object, image background, emission bandwidth, sample induced aberrations), and optical parameters (such as numerical aperture or phase mask size, system's photon-efficiency or throughput, system aberrations, magnification, emission filters and dichroics, excitation laser powers, excitation laser polarization, detection polarization).

Each of these experimental parameters directly influences one or both of the fundamental parameters noted above (first paragraph). For example, the fundamental parameter of PSF's gradient is affected by sample or system aberrations, emission bandwidth, numerical aperture, and background. In other words an increase in aberrations, an increase in bandwidth (incoherent addition of PSFs with different wavelengths results in a wider PSF), an increase in background, or a decrease in

phase mask size would result in a PSF with lower gradient. Similarly, the fundamental parameter of signal to noise is affected by detector noise, number of photons, efficiency, laser power, etc. In the future, CRB computations can be made to account for these experimental parameters once they are quantitatively modeled. Specifically, the parameters that affect the PSF gradient result in modifications to the exact DH-PSF shape used in CRB calculations, and the parameters that affect the SNR affect the probability density function used in CRB calculations.

The following two subsections qualitatively analyze the effect of pixel size and image background on the DH-PSF CRB. A quantitative analysis of these parameters, however, is a part of future work.

7.2.1 Effect of pixel size

Fig. 7.1 shows the effect of increasing the pixel size (using detectors with various pixel sizes) on the detected DH-PSF corresponding to an emitter with 10,000 (detected) photons for a given system magnification. Equivalently, this can be accomplished by varying the magnification of the imaging system with a fixed pixel size. Here, we will focus on the former case. As the pixel size decreases, it is clear that the DH-PSF is sampled better. This benefit in sampling comes at the expense of fewer photons per pixel (i.e. a distribution of photons over more pixels). In a shot-noise limited case, the sum of the noise variances of all pixels is a constant (in our example, 10000) regardless of the number of pixels.
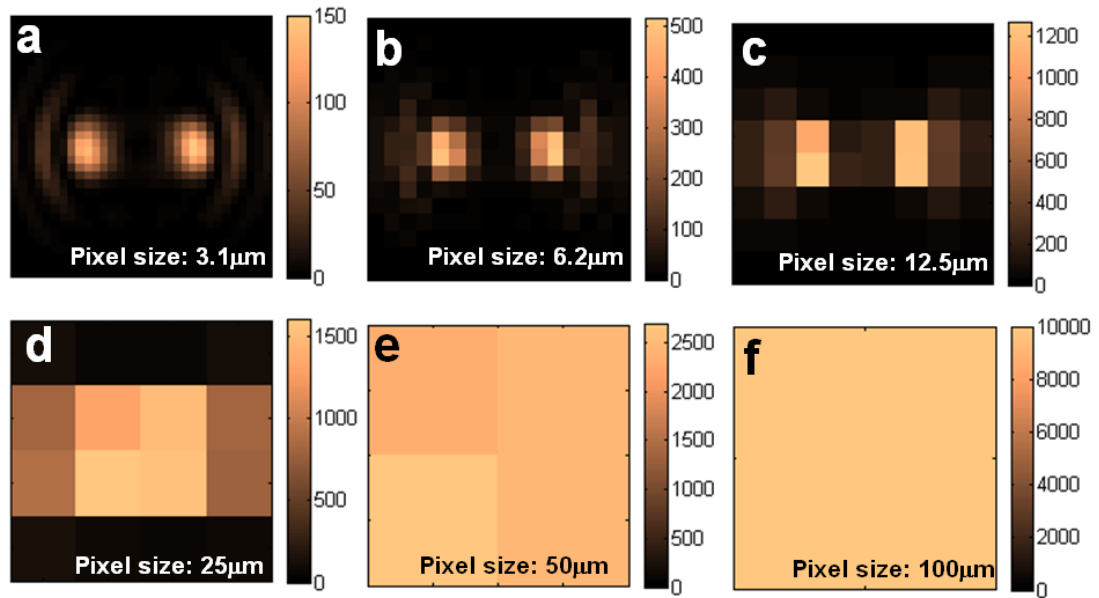
Fig. 7.1. Effect of pixel size. As the pixel size decreases for a given magnification (equivalently, as magnification increases for a given pixel size) in a photon-limited system, the DH-PSF is better sampled, but with a decrease in the number of photons per pixel. The optimal number of pixels sampling the DH-PSF depends on the SNR per pixel of the system.

However, when pixel dependent noise sources such as read noise are strong, having more pixels in the PSF results in the reduction of the detected-PSF SNR. Here we call the PSF after being sampled by the detector as detected-PSF, in contrast to the continuous optical-PSF of the system. Thus the detector pixels affect the fundamental SNR parameter influencing the CRB. Interestingly, this pixel factor also affects the other fundamental CRB parameter of PSF gradient. It can be seen from Fig. 7.1 that large pixel sizes result in the reduction of detected-PSF gradient. In the extreme case of the whole optical-PSF falling within a single pixel, the detected-PSF gradient is zero, and the position of the optical-PSF can only be localized to be within the pixel.

From the detected-PSF-gradient point of view, having more pixels is beneficial. However, from the SNR point of view, one will need to analyze the noise-sources per pixel of the detector to determine the effect of increasing the number of pixels. What can be definitely be stated, however, is that increasing the number of pixels cannot possibly result in better overall detected-PSF SNR. Even the best case (shot-noise regime), the noise variance of a better sampled PSF is only equal to that of a poorly sampled PSF. In all other regimes, the noise variance of a better sampled PSF will be higher (worse) than that of a poorly sampled PSF. In such regimes, it is clearly not beneficial to have a lot of pixels (more noise) or very few pixels (poor detected-PSF gradient), thereby suggesting an optimal number for the PSF sampling rate. Such an optimal number would however be specific to the noise sources of a system. See Ref. 38 for analysis on the effect of pixels for the standard PSF.

7.2.2 Effect of image background

Imaging systems often suffer from a background in detected images that lead to the degradation of image contrast. Background can result from bright-field or phase imaging microscope modalities, out of focus emitters or scatters, detector background noise, and also from the PSF side lobes.

Here we focus on the best-case imaging scenario, where the system parameters (such as illumination power, detector gain, exposure time, etc) are adjusted to make the PSF span the dynamic range of the detector. In detector-limited systems, as explained in chapter 3, such an adjustment can be accomplished with an appropriate illumination power setting, clearly leading to an improved SNR and reduced PSF-

intensity-quantization effects. In photon-limited applications, such as single-molecule imaging, this spanning of the dynamic range can be accomplished by setting EMCCD gain and exposure time appropriately. Interestingly, such a photon-limited detector setting also leads to an improved SNR, mainly because the on-chip electron amplification does not amplify the detector's read noise. Fig. 7.2 shows the effect of image background on a detected PSF in the best-case imaging scenario. As the background level increases, the PSF gradient decreases significantly, with almost zero gradient for very high background levels, as shown in Fig. 7.2 (c). Image background consequently results in the degradation of localization precisions (higher CRBs).
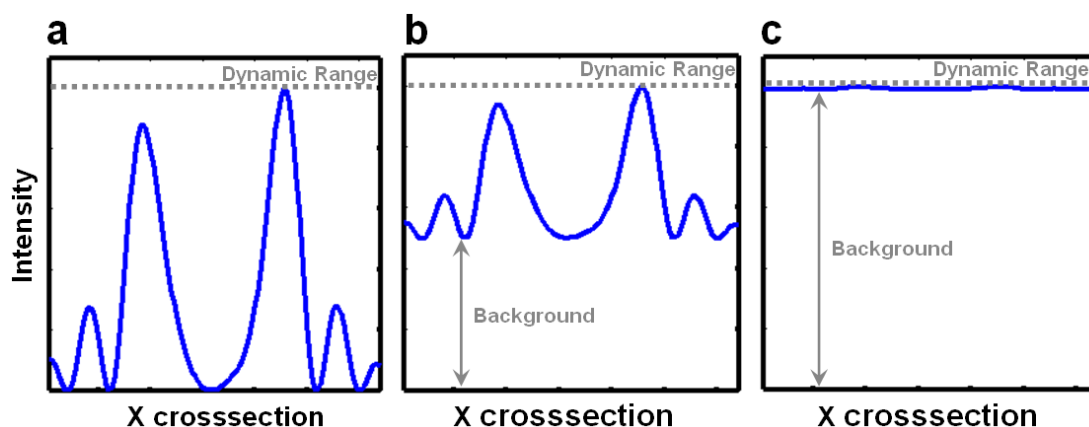
Fig. 7.2. Effect of image background. As the image background increases for a given signal level, the gradient of the detected PSF (scaled to reach the detector's dynamic range for best CRB) decreases.

7.3   Unlimited precision in detector-limited systems

From the information theoretical comparisons of chapters 3 and 4, it is clear that the DH-PSF systems exhibit higher Fisher Information (FI), i.e. better position localization accuracies, than standard PSF systems. But a question still remains: is there a PSF with higher FI than the DH-PSF? We explore this question below.

For a given noise level, the FI of a PSF primarily depends on the shape of the PSF. A PSF exhibiting a dramatic change in shape in all three dimensions is the best PSF for 3D position estimation. While optimization routines with constraints enforcing such a dramatic change in shape can be developed, the routines would converge only if the PSF satisfies the wave equation.

Interestingly, PSFs with higher FI than the DH-PSF can be developed in detector-limited systems (bright-field, dark-field, phase contrast, etc.) by compromising on the volume occupied by a PSF. In other words, the idea here is to physically increase the size of a PSF in order to accommodate more spatial information within a given area or volume. Because the detected number of photons can be increased by increasing the illumination intensity in detector-limited systems, PSF size can be increased without compromising SNR. Fig. 7.3 shows three PSFs that exhibit high FI in 1D (X), 2D (X,Y), and 3D (X,Y,Z). The PSF with high 1D FI is essentially a $sin^2(X)$ function (Fig. 7.3a) with a finite PSF width (termed *sine-PSF* here). Each lobe of this PSF is smaller than that of an Airy disc along the X dimension. This PSF has a very high gradient along the X dimension, with almost zero gradient along Y and Z dimensions. The PSF with high 2D FI has a series of spots within a finite PSF width (termed *spots-PSF* here). This PSF simultaneously has high gradients along X and Y

dimensions, with almost zero gradient along the Z dimension. The size of each spot is smaller than that of an Airy disc in X and Y dimensions. The PSF with high 3D Fisher information (Fig. 7.3c) is a finite *Talbot PSF*, operating between a Talbot image and a phase-reversed Talbot image, with a Talbot sub-image as the focal plane. This PSF was optimized to reduce the background in the Talbot subimage. Interestingly, the Talbot PSF has high spatial gradients along all three dimensions.
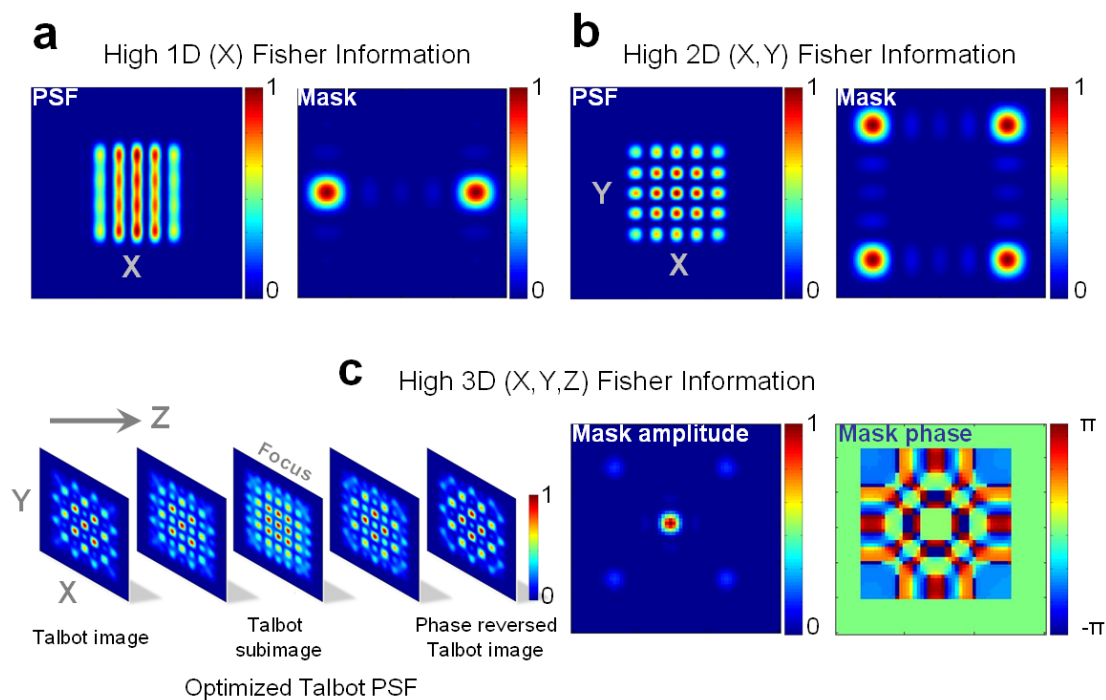
Fig. 7.3. Detector-limited PSFs with high (a) 1D, (b) 2D, and (c) 3D Fisher Information

It is worth noting that the FI of the sine-PSF along the X dimension is higher than the FI of the spots-PSF along X, which is higher than the FI of the Talbot-PSF along X. Similarly, the FI of the spots PSF along Y is higher than the FI of the Talbot-PSF along Y. This means that PSFs that are explicitly designed for position localization

along a given dimension perform better (along that dimension) than PSFs designed to simultaneously localize along multiple dimensions.

The PSFs of Fig. 7.3 are interesting because their FIs can be arbitrarily increased (for a given noise level) by increasing the PSF widths. These PSFs open up new ways for tracking sparse particles with very high precisions.

7.4   Application of double-helix PSF to quantitative phase imaging

Conventional bright field transmission microscopes employ detectors that observe intensity modulations while remaining indifferent to the phase modulations of light. Therefore, such microscopes cannot be directly used to examine non-absorbing samples (phase objects) such as biological cells without staining them with dyes. Phase microscopy techniques such as Zernike phase contrast (*Nobel prize in physics - 1953*) and differential interference contrast produce very good contrast with phase objects, but unfortunately cannot produce quantitative phase images, with each image point representing the optical path length (OPL) of an object point.

There has been continued interest in developing quantitative phase imaging systems that can deliver accurate OPL profiles of phase only samples. In fact, we recently introduced quantitative structured-illumination phase (QSIP) microscopy [79, 80], a technique that uses a structured illumination and an image processing algorithm implementing a closed-form analytical solution to estimate quantitative OPL profiles from structure deformations. In this section, we propose that the DH-

PSF can be directly applied to quantitative phase imaging with high phase resolutions.

The idea is to use a structured illumination together with the DH-PSF in a bright field microscope (Fig. 7.4).
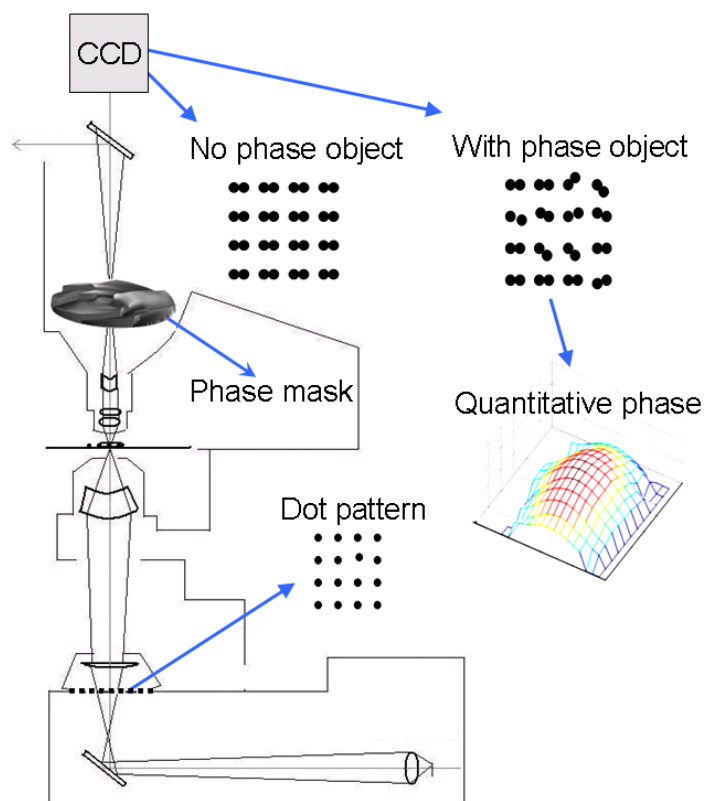
Fig. 7.4. Quantitative phase microscopy using a structured-illumination DH-PSF system.

Specifically, a dot pattern is imaged on the sample plane, for example, by placing an amplitude mask in the microscope's field diaphragm. In the absence of any phase object in the sample plane, each dot appears with two horizontally oriented lobes in the detected image. When a thin phase sample is introduced in the sample plane, each dot in the sample plane incurs a phase-retardation that is directly related to the OPL

of the sample at the location of the dot. This results in an image with differently rotated DH-PSF lobes. By estimating the DH-PSF rotation angle for each dot, the sample OPL at the location of the dot can be estimated. From chapters 3, 4, 5, and 6, we know that the DH-PSF can estimate nanometer scale position variations in the axial dimension. In the context of phase imaging, this directly translates to nanometer scale OPL resolution (OPL resolution is defined as the smallest change in OPL that can be resolved).

For thick phase objects, the DH-PSF lobes for each dot also shift transversely, in addition to exhibiting rotation. In this case, the closed-form analytical solution derived for QSIP may be used in addition to the information from DH-PSF rotation to estimate the sample's OPL profile.

Chapter 8

Conclusions

This thesis introduced a 3D nanoscopy paradigm using the double-helix point spread function. By taking advantage of a cloud pattern in the Gauss-Laguerre modal plane, a multi-domain optimization procedure is used to design an on-axis double-helix PSF phase mask that generates a rotating PSF in a limited region of space with over 30 times higher light efficiency than traditional rotating PSFs, thereby opening up diffracted rotation to systems with a limited photon budget. Information theoretical analyses show that the DH-PSF is fundamentally better for 3D position localization than the standard PSF in both detector-limited and photon-limited systems. With appropriate DH-PSF phase masks in the imaging path, a variety of 2D microscope modalities such as bright-field, dark-field, and fluorescence can be directly transformed into their 3D counterparts. With a single image, DH-PSF microscopes localize the 3D positions of multiple fluorescent and scattering microparticles with nanometer scale 3D precisions. By periodically acquiring DH-PSF images, 3D positions of multiple moving fluorescent microparticles can be simultaneously tracked, while computing their 3D average velocities.

Single fluorescent molecules can be localized with nanometer scale 3D precisions with DH-PSF fluorescence microscopes. Using photoactivatable molecules along with DH-PSF microscopes enables the ability to resolve molecules separated by as close as a few nanometers in 3D, thereby breaking the optical diffraction limit by over an order of magnitude in all three dimensions. Polarization-specific intracellular

features can be resolved, with nanometer scale 3D resolutions, using a polarization sensitive DH-PSF nanoscope that phase modulates the orthogonal polarization components of single molecule emissions with a single spatial light modulator, and detects them separately with a single detector.

The DH-PSF 3D nanoscopy paradigm introduced here is powerful in its ability to probe the nanoscale with fundamentally better 3D precisions and an extended axial range, while simultaneously being remarkable in its simplicity. The principles and experiments studied here can be applied to a variety of scientific investigations, including studies of molecular interactions, intracellular structure and function, particle trapping, particle image velocimetry, flow cytometry, phase imaging, material characterization, and nanofabrication.

Bibliography

[1] Klar, T. A.; Jakobs, S.; Dyba, M.; Egner, A.; Hell, S. W. "Fluorescence microscopy with diffraction resolution barrier broken by stimulated emission,"Proc. Nat. Acad. Sci. U.S.A, **97**, 8206– 8210 (2000).

[2] Gustafsson, M. G. L., "Surpassing the lateral resolution limit by a factor of two using structured illumination microscopy," J. Microsc. **198**, 82-87 (2000).

[3] E. Betzig, G. H. Patterson, R. Sougrat, O. W. Lindwasser, S. Olenych, J. S. Bonifacino, M. W. Davidson, J. Lippincott-Schwartz, and H. F. Hess, "Imaging intracellular fluorescent proteins at nanometer resolution," Science **313**, 1642 (2006).

[4] M. Rust, M. Bates, and X. Zhuang, "Sub-diffraction-limit imaging by stochastic optical reconstruction microscopy (STORM)," Nat. Methods. **3**, 793 (2006).

[5] S. T. Hess, T. P. K. Girirajan, and M. D. Mason, "Ultra-high resolution imaging by fluorescence photoactivation localization microscopy," Biophys. J. **91**, 4258 (2006).

[6] Z. Liu, H. Lee, Y. Xiong, C. Sun, and X. Zhang, "Far-field optical hyperlens magnifying sub-diffraction-limited objects." Science **315**, 1699-1701 (2007).

[7] R. Schmidt, C. A. Wurm, S. Jakobs, J. Engelhardt, A. Egner, and S. W. Hell, "Spherical nanosized focal spot unravels the interior of cells," Nat. Methods **5**, 539-544 (2008).

[8] Schermelleh, L., Carlton, P. M., Haase, S., Shao, L., Winoto, L., Kner, P., Burke, B., Cardoso, M. C., Agard, D. A., Gustafsson, M. G., Heinrich Leonhardt, and John W. Sedat, "Subdiffraction multicolor imaging of the nuclear periphery with 3D structured illumination microscopy," *Science* **320**, 1332-1336 (2008).

[9] B. Huang, W. Wang, M. Bates, and X. Zhuang, "Three-dimensional super-resolution imaging by stochastic optical reconstruction microscopy," Science **319**, 810 (2008).

[10] Juette MF, et al "Three-dimensional sub-100 nm resolution fluorescence microscopy of thick samples," Nature Methods **5**, 527-529 (2008).

[11] Vaziri A, Tang J, Shroff H, Shank CV, "Multilayer three-dimensional super resolution imaging of thick biological samples," Proc Nat Acad Sci USA **105**:20221–20226 (2008).

[12] Shtengel G.; Galbraith J. A.; Galbraith C. G.; Lippincott-Schwartz J.; Gillette J. M.; Manley S.; Sougrat R.; Waterman C. M.; Kanchanawong P.; Davidson M. W.; Fetter R. D.; Hess H. F., "Interferometric fluorescent super-resolution microscopy

resolves 3D cellular ultrastructure," Proc. Natl. Acad. Sci. USA **106**, 3125-3130 (2009).

[13] Y. Y. Schechner, R. Piestun, and J. Shamir, "Wave propagation with rotating intensity distributions," Phys. Rev. E **54**, R50–R53 (1996).

[14] V. V. Kotlyar, V. A. Soifer, and S. N. Khonina, "An algorithm for the generation of laser beams with longitudinal periodicity: rotating images," J. Mod. Opt. **44**, 1409-1416 (1997).

[15] R. Piestun, Y. Y. Schechner, and J. Shamir, "Propagation-invariant wave fields with finite energy," J. Opt. Soc. Am. A **17**, 294-303 (2000).

[16] S. N. Khonina, V. V. Kotlyar, V. A. Soifer, M. Honkanen, J. Lautanen, and J. Turunen, "Generation of rotating Gauss–Laguerre modes with binary-phase diffractive optics," J. Mod. Opt. **46**, 227–238 (1999).

[17] E. G. Abramochkin and V. G. Volostnikov, "Spiral light beams," Phys.-Usp. **47**, 1177-1203 (2004).

[18] A. Y. Bekshaev, M. S. Soskin, and M. V. Vasnetsov, "Angular momentum of a rotating light beam," Opt. Comm. **249**, 367-378 (2005).

[19] N. B. Simpson, L. Allen, and M. J. Padgett, "Optical tweezers and optical spanners with Laguerre-Gaussian modes," J. of Mod. Opt. **43**, 2485-2491 (1996).

[20] M. P. MacDonald, L. Paterson, K. Volke-Sepulveda, J. Arlt, W. Sibbett, and K. Dholakia, "Creation and manipulation of three-dimensional optically trapped structures," Science **296**, 1101-1103 (2002).

[21] R. Grimm, M. Weidemuller, and Y. B. Ovchinnikov, "Optical dipole traps for neutral atoms," Adv. At. Mol. Opt. Phys. **42**, 95-170 (2000).

[22] A. Greengard, Y. Y. Schechner, and R. Piestun, "Depth from diffracted rotation," Opt. Lett. **31**, 181-183 (2006).

[23] W. H. Lee, "Computer-generated holograms: techniques and applications," in *Progress in Optics*, E. Wolf, ed. (Elsevier, 1978), Chap. 3.

[24] R. Piestun, B. Spektor, and J. Shamir, "Wave fields in three dimensions: analysis and synthesis," J. Opt. Soc. Am. A **13**, 1837-1848 (1996).

[25] R. Piestun and J. Shamir, "Control of wave-front propagation with diffractive elements," Opt. Lett. **19**, 771-773 (1994).

[26] H. P. Kao and A. S. Verkman, "Tracking of single fluorescent particles in three dimensions: use of cylindrical optics to encode particle position," Biophys. J. **67**, 1291 (1994).

[27] M. Speidel, A. Jonas, and E.-L. Florin, "Three-dimensional tracking of fluorescent nanoparticles with subnanometer precision by use of off-focus imaging," Opt. Lett. **28**, 69 (2003).

[28] S. -H. Lee, Y. Roichman, G. -R. Yi, S. -H. Kim, S. -M. Yang, A. van Blaaderen, P. van Oostrum, and D. G. Grier, "Characterizing and tracking single colloidal particles with video holographic microscopy," Opt. Express **15**, 18275 (2007).

[29] D. G. Grier, "A revolution in optical manipulation," Nature **424**, 810 (2003).

[30] R. M. Dickson, A. B. Cubitt, R. Y. Tsien, W. E. Moerner, "On/off blinking and switching behaviour of single molecules of green fluorescent protein," Nature **388**, 355 (1997).

[31] R. E. Thompson, D. R. Larson, and W. W. Webb, "Precise nanometer localization analysis for individual fluorescent probes," Biophys. J. **82**, 2775 (2002).

[32] S. -H. Lee and D. G. Grier, "Holographic microscopy of holographically trapped three-dimensional structures," Opt. Express **15**, 1505 (2007).

[33] A. Marian, F. Charrière, T. Colomb, F. Montfort, J. Kühn, P. Marquet, C. Depeursinge, "On the complex three-dimensional amplitude point spread function of lenses and microscope objectives: theoretical aspects, simulations and measurements by digital holography," J. of Microscopy **225**(2), 156 (2007).

[34] J. Rosen and G. Brooker, "Non-scanning motionless fluorescence three-dimensional holographic microscopy," Nature Photonics **2**, 190 (2008).

[35] S. R. P. Pavani and R. Piestun, "High-efficiency rotating point spread functions," Opt. Express **16**, 3484 (2008).

[36] T. M. Cover and J. A. Thomas, *Elements of Information Theory* (Wiley-Interscience, 1991).

[37] S. M. Kay, *Fundamentals of Statistical Signal Processing: Estimation Theory* (Prentice-Hall, 1993).

[38] R. J. Ober, S. Ram, and S.E. Ward. "Localization accuracy in single-molecule microscopy," Biophys. J. **86**, 1185 (2004).

[39] S.R.P. Pavani and R. Piestun, "3D microscopy with a double-helix point spread function," Proc. SPIE 7184, 71840I (2009).

[40] L. Novotny and B. Hecht, *Principles of Nano-Optics, chapter 4* (Cambridge, 2006).

[41] J.A. Steyer and W. Almers, "Tracking single secretory granules in live chromaffin cells by evanescent-field fluorescence microscopy," Biophys. J. **76**, 2262–2271 (1999).

[42] D. Li, J. Xiong, A. Qu, and T. Xu, "Three-dimensional tracking of single secretory granules in live pc12 cells," Biophys. J. **87**, 1991-2001 (2004).

[43] R. M. Dickson, A. B. Cubitt, R. Y. Tsien, W. E. Moerner, "On/off blinking and switching behaviour of single molecules of green fluorescent protein," Nature **388**, 355 (1997).

[44] G. J. Schütz, M. Axmann, and H. Schindler, "Imaging single molecules in three dimensions," Sing. Mol. **2**(2):69–74 (2001).

[45] J. A. Steinkamp, J. S. Wilson, G. C. Saunders, and C. C. Stewart, "Phagocytosis: flow cytometric quantitation with fluorescent microspheres," Science **215**, 64-66 (1982).

[46] L. Holtzer, T. Meckel, and T. Schmidt, "Nanometric three-dimensional tracking of individual quantum dots in cells," Appl. Phys. Lett. **90**, 053902 (2007).

[47] J. Rosen and G. Brooker, "Non-scanning motionless fluorescence three-dimensional holographic microscopy," Nature Photonics **2**, 190-195 (2008).

[48] S. R. P. Pavani, A. Greengard, and R. Piestun, "Three-dimensional localization with nanometer accuracy using a detector-limited double-helix point spread function system," Appl. Phys. Lett. **95**, 021103 (2009).

[49] S.R.P. Pavani and R. Piestun, "Three dimensional tracking of fluorescent microparticles using a photon-limited double-helix response system," Opt. Express **16**, 22048-22057 (2008).

[50] Abbe E, "Beiträge zur theorie des mikroskops und der mikroskopischen wahrnehmung (translation: Contributions to the theory of the microscope and that microscopic perception). Arch Mikroskop Anat **9**, 413-468 (1873).

[51] Heisenberg W in The Physical Principles of Quantum Theory, (University of Chicago Press, Chicago) (1930).

[52] Bobroff N, "Position measurement with a resolution and noise-limited instrument," Rev. Sci. Instrum. **57**, 1152-1157 (1986).

[53] Gelles J, Schnapp BJ & Sheetz MP, "Tracking kinesin-driven movements with nanometre-scale precision," Nature **4**, 450-453 (1988).

[54] Ambrose WP, Basché T & Moerner WE, "Detection and spectroscopy of single pentacene molecules in a p-terphenyl crystal by means of fluorescence excitation," J Chem Phys **95**, 7150 (1991).

[55] van Oijen, A. M., Köhler J, Schmidt J, Müller M & Brakenhoff GJ, "3-dimensional super-resolution by spectrally selective imaging," Chem Phys Lett **292**, 183-187 (1998).

[56] Yildiz A, et al "Myosin V walks hand-over-hand: Single fluorophore imaging with 1.5-nm localization. Science **300**, 2061-2065 (2003).

[57] Ram S, Chao J, Prabhat P, Ward ES & Ober RJ, "A novel approach to determining the three-dimensional location of microscopic objects with applications to 3D particle tracking," Proc SPIE **6443**, 64430D-1-64430D-7 (2007).

[58] Sharonov A & Hochstrasser RM, "Wide-field subdiffraction imaging by accumulated binding of diffusing probes," Proc Natl Acad Sci U S A **103**, 18911-18916 (2006).

[59] Lidke KA, Rieger B, Jovin TM & Heintzmann R, "Superresolution by localization of quantum dots using blinking statistics," Opt Express **13**, 7052-7062 (2005).

[60] Ram S, Prabhat P, Chao J, Ward ES, Ober RJ, "High accuracy 3D quantum dot tracking with multifocal plane microscopy for the study of fast intracellular dynamics in live cells," Biophys J **95**:6025–6043 (2008).

[61] Lord SJ, et al "A photoactivatable Push−Pull fluorophore for single-molecule imaging in live cells," J Am Chem Soc **130**, 9204-9205 (2008).

[62] Willets KA, Ostroverkhova O, He M, Twieg RJ & Moerner WE, "New fluorophores for single-molecule spectroscopy," J Am Chem Soc **125**, 1174-1175 (2003).

[63] Shroff H, et al.. "Dual-color superresolution imaging of genetically expressed probes within individual adhesion complexes," Proc Nat Acad Sci USA **104**:20308–20313 (2007).

[64] Newberry M, "Mirametrics technical note on pixel response effects in CCD camera gain calibration http://www.mirametrics.com/tech_note_ccdgain.htm," (1998).

[65] Keana JFW & Cai SX, "New reagents for photoaffinity labeling: Synthesis and photolysis of functionalized perfluorophenyl azides," J Org Chem **55**, 3640-3647 (1990).

[66] Keana JFW & Xiong Cai S, "Functionalized perfluorophenyl azides: New reagents for photoaffinity labeling," Journal of Fluorine Chemistry **43**, 151-154 (1989).

[67] Stromgaard K, et al, "Ginkgolide derivatives for photolabeling studies: Preparation and pharmacological evaluation," J Med Chem **45**, 4038-4046 (2002).

[68] Michaela Wiegand TKL, "Synthesis of photoactive alpha-mannosides and mannosyl peptides and their evaluation for lectin labeling," European Journal of Organic Chemistry **2006**, 4841-4851 (2006).

[69] Pavani S. R. P.; Thompson M. A.; Biteen J. S.; Lord S. J.; Liu N.; Twieg R. J.; Piestun R.; Moerner W. E., "Three-dimensional, single-molecule fluorescence imaging beyond the diffraction limit by using a double-helix point spread function" Proc. Natl. Acad. Sci. USA **106**, 2995-2999 (2009).

[70] Gould, T.J.; Gunewardene, M. S.; Gudheti, M. V.; Verkhusha, V. V.; Yin, S.-R; Gosse, J. A.; Hess, S. T. "Nanoscale imaging of molecular positions and anisotropies," Nat. Methods **5**, 1027–1030 (2008).

[71] Ha, T.; Enderle, T.; Chemla, D. S.; Selvin, P. R.; Weiss, S. "Single Molecule Dynamics Studied by Polarization Modulation," Phys. Rev. Lett. **77**, 3979 (1996).

[72] Dickson, R. M.; Norris, D. J.; Moerner, W. E. "Simultaneous Imaging of Individual Molecules Aligned Both Parallel and Perpendicular to the Optic Axis," Phys. Rev. Lett. **81**, 5322 (1998).

[73] Sick, B.; Hecht, B.; Novotny, L. " Orientational Imaging of Single Molecules by Annular Illumination," Phys. Rev. Lett. **85**, 4482 (2000).

[74] Foreman, M. R.; Romero, C. M.; Török, P.; "Determination of the three-dimensional orientation of single molecules," Opt. Lett. 33, 1020–1022 (2008).

[75] Aguet, F.; Geissbühler, S.; Märki, I; Lasser, T; Unser, M., "Super-resolution orientation estimation and localization of fluorescent dipoles using 3-D steerable filters," Opt. Exp. **17** (8), p.6829 (2009).

[76] Patterson, G. H.; Lippincott-Schwartz J. "A Photoactivatable GFP for Selective Photolabeling of Proteins and Cells," Science **297**:1873–1877 (2002).

[77] S. R. P. Pavani, J. G. Deluca, and R. Piestun, "Polarization sensitive, 3D, single-molecule imaging of cells with a double-helix system," *submitted* (2009).

[78] Yariv, A. Optical Electronics in Modern Communications (Oxford University Press, New York, 1997).

[79] S. R. P. Pavani, A. Libertun, S. King, and C. Cogswell, "Quantitative structured-illumination phase microscopy," Appl. Opt. **47**, 15-24 (2008).

[80] S. R. P. Pavani, A. R. Libertun, S. V. King, and C. J. Cogswell, "QSIP: phase imaging made possible in a bright field microscope," Proc. SPIE **6861**, 686105 (2008).